The two-pion contribution to the hadronic vacuum polarization with staggered quarks.

Shaun Lahert,[1,2,*] Carleton DeTar,[1] Aida X. El-Khadra,[2,3]
Steven Gottlieb,[4] Andreas S. Kronfeld,[5] and Ruth S. Van de Water[5]

[1] *Department of Physics and Astronomy, University of Utah, Salt Lake City, UT, USA*
[2] *Department of Physics, University of Illinois, Urbana, Illinois, 61801, USA*
[3] *Illinois Center for the Advanced Studies of the Universe, University of Illinois, Urbana, Illinois, 61801, USA*
[4] *Department of Physics, Indiana University, Bloomington, IN 47405, USA*
[5] *Theory Division, Fermi National Accelerator Laboratory, Batavia, Illinois, 60510, USA*

(Dated: September 4, 2024)

Abstract

We present results from the first lattice QCD calculation of the two-pion contributions to the light-quark connected vector-current correlation function obtained from staggered-quark operators. We employ the MILC collaboration's gauge-field ensemble with $2+1+1$ flavors of highly improved staggered sea quarks at a lattice spacing of $a \approx 0.15$ fm with a light sea-quark mass at its physical value. The two-pion contributions allow for a refined determination of the noisy long-distance tail of the vector-current correlation function, which we use to compute the light-quark connected contribution to HVP with improved statistical precision. We compare our results with traditional noise-reduction techniques used in lattice QCD calculations of the light-quark connected HVP, namely the so-called fit and bounding methods. We observe a factor of roughly three improvement in the statistical precision in the determination of the HVP contribution to the muon's anomalous magnetic moment over these approaches. We also lay the group theoretical groundwork for extending this calculation to finer lattice spacings with increased numbers of staggered two-pion taste states.

* shaun.lahert@gmail.com

I. INTRODUCTION

The long-standing tension between experimental measurements and Standard Model expectations for the anomalous magnetic moment of the muon $a_\mu \equiv (g_\mu - 2)/2$ has been an intriguing hint of new physics for many years. On the experimental side, the Fermilab $g-2$ collaboration (E989) released their second measurement result from their runs 2 and 3 data in August 2023 [1], finding it in excellent agreement with all previous measurements [2, 3]. The resulting experimental uncertainty is now at 190 ppb, and the Fermilab experiment is on track to reach their uncertainty goal of 140 ppb with the ongoing analysis of their runs 4, 5, and 6 data. They are expected to release their final result in 2025.

On the theory side, contributions to a_μ from all SM particles and interactions must be quantified with commensurate precision in order to maximize the discovery potential of the experimental effort. Hadronic corrections, comprised of hadronic vacuum polarization (HVP) and hadronic light-by-light (HLbL), are the main source of theory uncertainty, due to their nonperturbative nature, being governed by quantum chromodynamics (QCD). The HVP contribution to the muon $g-2$, $a_\mu^{\rm HVP,LO}$, which enters at order α^2, is the larger of the two and the dominant source of error. The Standard Model prediction of a_μ in the Muon $g-2$ Theory Initiative white paper [4] was based on a dispersive evaluation of $a_\mu^{\rm HVP,LO}$, in which experimental measurements of $e^+e^- \to$ hadrons cross-sections serve as nonperturbative inputs [5–24].

Lattice QCD offers an *ab initio* approach to computing the hadronic corrections and hence allows for an entirely SM theory based evaluation.[1] While lattice QCD calculations of $a_\mu^{\rm HVP,LO}$ have not yet reached the needed precision level, in 2021 the BMW collaboration published a lattice HVP result with a quoted uncertainty of 0.8% [25]. Compared with Ref. [4], the BMW result for $a_\mu^{\rm HVP,LO}$ is higher by about 2σ and implies a SM value for a_μ that is about 1.5σ lower than the experimental average.[2] Independent lattice-QCD calculations, with improved precision, are needed to address this theoretical discrepancy and to obtain a consolidated lattice QCD average for this important quantity. The purpose of this paper is to develop the methodology to better control the systematic uncertainty of long-distance contributions to HVP, as part of a larger undertaking [27, 28].

The HVP is typically computed in lattice QCD as an integral over Euclidean time t of two-point correlation functions with vector-current operators (representing the corresponding EM current) at the source and sink [29, 30]. As is well known, vector-current correlation functions of light-quark operators suffer from rapidly increasing statistical uncertainty at large Euclidean times, which in turn limits statistical precision of the integral. Noise-reduction methods, such as the truncated solver method, low-mode averaging or improvement [31–35] coupled with high-statistics computations have been used to improve statistical precision at large Euclidean times. In addition, analysis methods such as the bounding [36] and fit [27] methods can yield further improvements. However, to obtain lattice QCD results of $a_\mu^{\rm HVP,LO}$ at the required few permille level, better control over the long-distance tail of the correlation function is needed. In the spectral decomposition of

[1] Apart from the experimental inputs (usually hadron masses) needed to fix the quark masses and lattice spacing in the QCD Lagrangian.

[2] Very recently, a new, hybrid result for $a_\mu^{\rm HVP,LO}$ with a quoted uncertainty of 0.5% was presented in Ref. [26]. It combines an updated lattice QCD calculation with a data-driven evaluation of the contributions at long distances, and yields an increased tension with the data-driven prediction in Ref. [4].

the vector-current correlation function, the dominant contributions at large Euclidean times come from two-pion states (where the pions have back-to-back momenta) with energies below the ρ^0 meson. Hence, a robust strategy is to compute additional correlation functions to obtain the energies and amplitudes of all contributing low-energy two-pion states. This approach, which requires the computation of two-, three-, and four-point functions, has already been implemented for order-a-improved Wilson [37] and domain wall fermions [38].

In this work, we perform the first such computation for the case of staggered quarks with the full set of staggered two-meson operators. First results from this study were presented in Ref. [39].[3] The staggered formulation [42–45] of lattice QCD, which uses the so-called doubling symmetry of the naively discretized Dirac action to reduce the number of spin degrees of freedom from 4 to 1, results in a more complicated group structure with an additional quantum number which is called 'taste.' Hence, careful treatment of the modified group structure is needed to correctly resolve the low-lying spectra. This includes obtaining the irreducible representations of the staggered group, computing the corresponding Clebsch-Gordan coefficients and constructing the multi-particle two-pion operators. With the staggered operator basis in hand, the remaining steps are similar to those in Refs. [37, 38]. After computing the correlation functions on the $a \approx 0.15$ fm HISQ ensemble with a light-sea quark mass at its physical value [46], we obtain the spectrum of the two-pion energies and amplitudes from a generalized-eigenvalue-problem (GEVP) analysis and finally use it to reconstruct the two-point vector-current correlation function at large t. We find a significant reduction in the statistical uncertainty of the resulting $a_\mu^{\mathrm{HVP,LO}}$ over the traditional methods of large-t noise reduction, in agreement with the studies using other discretizations. Hence, we plan to incorporate this approach into our ongoing effort within the Fermilab Lattice, HPQCD, and MILC Collaborations [27, 28] to compute $a_\mu^{\mathrm{HVP,LO}}$ at the less than 0.5% level.

The rest of the paper is organized as follows. Section II introduces the vector-current correlation function and its relation to $a_\mu^{\mathrm{HVP,LO}}$. Section III details our calculation strategy, from constructing our operator basis (Secs. III A and III C), computing the correlation functions (Secs. III B and III D) and determination of the two-pion energies and amplitudes from the GEVP (Sec. III F). In Sec. IV, we present our final results on the $a \approx 0.15$ ensemble, for the two-pion spectrum (Sec. IV A) and our subsequent reconstruction of the correlation function and computation of $a_\mu^{\mathrm{HVP,LO}}$ (Sec. IV B). Section V provides a summary and outlook of the potential impact of this approach. In Appendices A to C, we cover the prerequisite details of the staggered-quark formalism, namely the notation employed for the irreducible representations, treatment of staggered states at non-zero momentum and connection to the continuum. We include the theoretical details to perform this calculation at any lattice spacing with any number of two-pion states. We note that our work builds on the results presented in Refs. [47–49] and we restate the pertinent parts using our notation (and include minor corrections). Appendix D contains tables of the Clebsch-Gordan coefficients and Appendix E discusses the correct weighting of connected and disconnected diagrams with rooted staggered quarks. Finally, Appendix F details a slight modification made to the two-pion operators and how it impacts the analysis.

[3] See also Ref. [40] for a detailed description of the group theoretic derivation, analysis steps, and additional background information. Preliminary results from a similar effort were reported in Ref. [41].

II. PRELIMINARIES

In lattice QCD, the hadronic vacuum polarization contribution to the muon's anomalous magnetic moment, $a_\mu^{\rm HVP,LO}$, is, typically, obtained from weighted integrals of Euclidean vector-current correlation functions [30, 50],

$$C(t) = \frac{1}{3}\sum_{\vec{x},k}\left\langle J^k(\vec{x},t)J^k(0)\right\rangle, \quad k=1,2,3, \tag{2.1}$$

$$J^\mu(x) = \sum_f q_f \bar{\psi}_f(x)\gamma^\mu\psi_f(x), \tag{2.2}$$

where the electromagnetic current $J^\mu(x)$ is summed over all quark flavors $f=\{u,d,s,c,b,t\}$ and q_f are the corresponding electric charges in units of e. The RHS of Eq. (2.1) contains both quark-line connected and disconnected Wick contractions. The leading-order HVP contribution to a_μ is obtained from the following formulae [30]:

$$a_\mu^{\rm HVP,LO} = 4\alpha^2\int_0^\infty {\rm d}t\, C(t)\tilde{K}(t) \tag{2.3}$$

$$\tilde{K}(t) = 2\int_0^\infty \frac{{\rm d}Q}{Q}\,K_E(Q^2)\left[Q^2t^2 - 4\sin^2\left(\frac{Qt}{2}\right)\right]. \tag{2.4}$$

The integration kernel $K_E(Q^2)$ [29], which contains the muon mass dependence, is given as

$$K_E\left(Q^2\right) = \frac{m_\mu^2 Q^2 Z^3(1-Q^2Z)}{1+m_\mu^2}, \tag{2.5}$$

where $Z = [(Q^4+4m_\mu^2Q^2)^{1/2}-Q^2]/(2m_\mu^2Q^2)$. In lattice-QCD calculations of $a_\mu^{\rm HVP,LO}$ the contributions from each quark flavor and from connected and disconnected Wick contractions are typically computed separately and then summed up. Here we focus on the dominant light-quark connected contribution in the isospin-symmetric limit, a_μ^{ll}(conn.). Therefore, our electromagnetic vector current $J^\mu(x)$ includes only the up and down terms with both masses equal, $m_l = (m_u+m_d)/2$. Additionally, the correlation function $C(t)$ includes only the connected contractions. This can be straightforwardly related to the pure isospin 1 contribution. Splitting the flavor components of the vector current operator from Eq. (2.2) into isospin 1 and isospin 0 components, $J_i = J_i^{I=1} + J_i^{I=0}$, gives

$$J_i^{I=1} = \rho_i^0 = \frac{1}{2}\left(\bar{u}\gamma_i u - \bar{d}\gamma_i d\right), \tag{2.6}$$

$$J_i^{I=0} = \frac{1}{6}\left(\bar{u}\gamma_i u + \bar{d}\gamma_i d - 2\bar{s}\gamma_i s + \ldots\right). \tag{2.7}$$

We note that $J_i^{I=1}$ has $I_3=0$ and is equivalent to a ρ^0 meson bilinear. (In most of the rest of this work the ρ^0 notation is employed.) Hence, once charge factors are accounted for, the following linear relationship between the light-quark connected and $I=1$ correlation functions is obtained,

$$\left\langle J_i^l(x)J_i^l(0)\right\rangle_{\rm conn.} = \frac{10}{9}\left\langle \rho_i^0(x)\rho_i^0(0)\right\rangle, \tag{2.8}$$

$$\Rightarrow C^{ll}(t)(\text{conn.}) = \frac{10}{9} C_{\rho\to\rho}(t). \tag{2.9}$$

The light-quark connected correlation function, therefore, has the following spectral representation,

$$C^{ll}(t)(\text{conn.}) = \frac{10}{9} \sum_{n=0} \left|\langle 0|\rho^0|n\rangle\right|^2 e^{-E_n t}\,. \tag{2.10}$$

The average over the spatial direction in Eq. (2.10) is implicit. The overlap amplitudes $\langle 0|\rho^0|n\rangle$ select the states $|n\rangle$ of the Hamiltonian with the same quantum numbers as the ρ^0.

The signal-to-noise issue discussed in the introduction can be traced to the fact that the variance of this correlation function falls off with an exponent of $2m_\pi$ [51]

$$\lim_{t\to\infty} \sigma^2_{C^{ll}(t)(\text{conn.})} \sim \lim_{t\to\infty} \left[\left\langle \left(\rho_i^0(t)\rho_i^0(0)\right)^2\right\rangle - \left\langle \rho_i^0(t)\rho_i^0(0)\right\rangle^2\right] \sim \lim_{t\to\infty} \left\langle \left(\rho_i^0(t)\rho_i^0(0)\right)^2\right\rangle \sim e^{-2m_\pi t}\,. \tag{2.11}$$

while the signal falls off with the lowest energy $I = 1$, $I_3 = 0$ state, which is a two-pion state with the smallest non-zero back-to-back momentum possible in the finite volume of the lattice,

$$\lim_{t\to\infty} C^{ll}(t)(\text{conn.}) \sim e^{-E^0_{\pi\pi}(p\neq 0)t}\,. \tag{2.12}$$

The noise, the square root of the variance in Eq. (2.11), falls off more slowly and overwhelms the two-pion signal in the large-time region.

At present, there are two commonly employed analysis-based approaches to address the signal-to-noise issue when computing $a_\mu^{ll}(\text{conn.})$, namely, the "bounding" and "fit" methods:

- **Bounding method** [36]: Two series of $a_\mu^{ll}(\text{conn.})$ values are obtained by replacing the correlation function, $C^{ll}(t)(\text{conn.})$, with

$$C_{\text{bounded}}(t) = \begin{cases} C^{ll}(t)(\text{conn.}) & \text{if } t \le t_{\text{cut}}, \\ C^{ll}(t_{\text{cut}})(\text{conn.}) e^{-E_{\text{bound}}(t-t_{\text{cut}})} & \text{if } t > t_{\text{cut}}, \end{cases} \tag{2.13}$$

  for upper and lower bounding energies, resulting in lower and upper bounds on $C^{ll}(t)(\text{conn.})$, respectively. Here, t_{cut} is a free parameter that ranges over the temporal extent of the lattice. The final result for $a_\mu^{ll}(\text{conn.})$ is obtained at the value of t_{cut} where the two bounds meet. The lower energy bound is taken to be the free, lattice two-pion energy [25, 36], $E_{\text{bound}} = 2\sqrt{(2\pi/L)^2 + M_\pi^2}$, where the pion mass, M_π, is computed on the same lattice ensemble. The energy appearing in Eq. (2.12) is the interacting energy, which is smaller than the free energy due to the binding energy of the $\pi\pi$ state. However, this approximation is reasonable because the binding energy is small enough to shift $a_\mu^{ll}(\text{conn.})$ by only a small fraction of the total uncertainties currently achievable [52].[4] The upper energy bound, usually taken to be $E_{\text{bound}} = \infty$, can be improved by, instead, taking the ground state from a fit to $C^{ll}(t)(\text{conn.})$. In the case of staggered fermions, the final choice of t_{cut} is complicated by the presence of

[4] We find that this is true for the differences between interacting and free energies obtained in this work.

oscillations in the correlation function. Compared with direct integration, the bounding method improves the statistical precision of a_μ^{ll}(conn.). However, the improvement is limited, because the bounds typically meet well into the noisy part of the tail, at roughly 2.5–3.5 fm.

- **Fit method** [53]: For this approach, the correlation function is fit over a time range suitable for determining the spectrum. The determined spectrum can be improved via combined fits to, for example, smeared correlated functions. The energies and $C^{ll}(t)$(conn.) amplitudes are then used to reconstruct it after some time $t \geq t^\star$. Here, there is a systematic uncertainty associated with how well the fit correctly parameterizes the behavior of the lowest-energy states that determine $C^{ll}(t)$(conn.) in the region where it is being replaced.

In this work, we treat the signal-to-noise problem by obtaining an accurate spectral representation of the vector-current correlation function at large Euclidean times. For this purpose, we generate correlation functions using suitably constructed two-pion operators, from which the following matrix of correlation functions is formed:

$$\mathbf{C}(t) = \begin{pmatrix} C_{\rho,\tilde{\rho}\to\rho,\tilde{\rho}}(t) & C_{\rho,\tilde{\rho}\to\pi\pi}(t) \\ C_{\pi\pi\to\rho,\tilde{\rho}}(t) & C_{\pi\pi\to\pi\pi}(t) \end{pmatrix}. \tag{2.14}$$

The upper left 2×2 block, $C_{\rho,\tilde{\rho}\to\rho,\tilde{\rho}}(t)$, contains the correlation function constructed with the ρ^0 operator of Eq. (2.6) along with additional correlation functions obtained by including a smeared version of the operator $\tilde{\rho}^0$. This smearing improves the overlap with the ground state [27]. The bottom right block consists of the two-pion to two-pion correlation functions, and the size of the block is given by the number of two-pion operators included. The off-diagonal blocks are correlation functions constructed from the (ρ^0,$\tilde{\rho}^0$) and two-pion operators. With this matrix, the lowest lying states for the $I = 1$, $I_3 = 0$ channel can be precisely resolved and the tail of $C^{ll}(t)$(conn.) can be reconstructed from this information. A similar approach was implemented in Ref. [54] in a study of the ρ resonance parameters with staggered valence quarks, where, however, only the simplest case of Goldstone-boson pion operators was considered. Ours is the first study of this system based on a complete description of the staggered two-pion operators.

III. METHODOLOGY

In this section, we describe all the steps of the calculation. Section III A describes the computation of the Clebsch-Gordan coefficients for the symmetry group of the staggered-fermion transfer matrix and, hence, the construction of the two-pion operators used here. In Sec. III B, we give the required Wick contractions corresponding to the correlation functions in the matrix of Eq. (2.14). We tabulate the complete staggered operator bases on the physical-mass HISQ ensembles in Sec. III C. Section III D describes the numerical strategy we employ to compute the Wick contractions of Sec. III B. In Sec. III E, we give our preferred approach for dealing with finite-time effects in the diagonal four-point correlation functions of Eq. (2.14). Finally, in Sec. III F, we discuss our GEVP based approach for extracting the desired energies and amplitudes from our matrix using a correlated fit.

A. Operator construction

For the case of staggered quarks, the two-pion states that couple to the ρ^0 need to transform correctly under isospin and the staggered symmetry group. Under isospin, the two-pion operators need to transform as $I = 1$, $I_3 = 0$, where the single pion operators have the following $I = 1$ quantum numbers,

$$\pi^+ = -\bar{d}u \qquad I_3 = 1, \tag{3.1}$$

$$\pi^- = \bar{u}d \qquad I_3 = -1, \tag{3.2}$$

$$\pi^0 = \frac{1}{\sqrt{2}}\left(\bar{u}u - \bar{d}d\right) \qquad I_3 = 0. \tag{3.3}$$

and the two-pion operator then takes the form

$$(\pi\pi)^{I=1,I_3=0} = \frac{1}{\sqrt{2}}\pi^+\pi^- - \frac{1}{\sqrt{2}}\pi^-\pi^+. \tag{3.4}$$

The $\pi^\pm$ states transform into each other under charge conjugation, so the minus sign on the right-hand side of Eq. (3.4) ensures that these two-pion states have $C = -1$, just like ρ^0. The factors $\pm 1/\sqrt{2}$ are SU(2) Clebsch-Gordan coefficients—the rest of this subsection explains how to set up the analogous construction for the staggered symmetry group, to obtain two-pion operators with the same quantum numbers as staggered ρ^0 states.

Here, "quantum numbers" refer to irreducible representations (irreps) of the symmetry group of the transfer matrix of staggered quarks for N_s^3 spatial lattices. This group is

$$G_{T_0}(N_s) = Z^3_{N_s/2} \rtimes (\Gamma_{4,1} \rtimes O_{\rm h}), \tag{3.5}$$

where T_0 refers to the two timeslice transfer matrix [44], and $\rtimes$ denotes semi-direct product. The factors are, respectively, two-hop translations, the Clifford group of taste and charge conjugation, and the symmetry group of a cube. Eigenstates of translations are labeled by momentum $\vec{p}$, where each component satisfies,

$$p_i = \frac{2\pi}{aN_s}\ell_i, \quad \ell_i = -\frac{N_s}{4}+1, \ldots, -1, 0, 1, \ldots, \frac{N_s}{4}, \tag{3.6}$$

for periodic boundary conditions; below it is more convenient to use $\vec{\ell}$ to label irreps. For mesons, taste is denoted by a four-vector with entries ± 1 or, equivalently, $e^{i\xi_\mu}$, $\xi_\mu \in \{0, \pi\}$. Similarly, charge conjugation is $e^{i\xi_C} = \pm 1$. The irreps of $O_{\rm h}$ are $A_0^\pm$, $A_1^\pm$, $E^\pm$, $T_0^\pm$, $T_1^\pm$, with the superscript for parity. We denote a general (bosonic) irrep

$$(\ell_1, \ell_2, \ell_3) \rtimes [(\xi_0, \xi_1, \xi_2, \xi_3), \xi_C] \rtimes R, \tag{3.7}$$

where the $\rtimes$ is reminder that the formalism of semi-direct groups is needed to construct the irrep; the last factor R denotes an irrep of $O_{\rm h}$ or a so-called little group appropriate to $\vec{\ell}$ and ξ_μ. Appendices A to D contains a full discussion of the staggered group irreps; below we refer to them for details.

The staggered two-pion operators must transform under the same irreducible representation (irrep) as the vector current operator. At zero momentum, the sixteen tastes are collected into five irreps; see Appendix C 1. We choose the taste-singlet ρ^0 (see Eq. (C3))

because it couples to a ground two-pion state of two pseudo-Goldstone boson pions, the lowest-energy two-pion state possible for any taste. Furthermore, all two-pion states which couple to the taste-singlet ρ^0 are taste singlets as well, meaning the two pions in the two-pion state must be in the same taste irrep. Alongside the taste irreps, we must also consider the momentum and rotation irreps. This is achieved by computing the Clebsch-Gordan coefficients (CGs) for $G_{T_0} \times G_{T_0} \to G_{T_0}$ as follows:

$$\pi^{(\alpha)}(\vec{p}) \otimes \pi^{(\alpha')}(-\vec{p}) \to (0,0,0) \rtimes [(0,0,0,0), \pi] \rtimes T_0^-, \tag{3.8}$$

where $\pi^{(\alpha)}(\vec{p})$ denotes some non-zero momentum pion irrep, with the full list of such irreps given in Appendix C 2. The right-hand side of Eq. (3.8) is the taste-singlet ρ^0 irrep from Eq. (C3).

In order to compute these CGs, the irreps from Appendix A 3 must be constructed. For values of N_s typically used in numerical simulations, $G_{T_0}(N_s)$ is enormous, but we are interested only in two-pion states below ρ^0 threshold (see Sec. III C). For the MILC HISQ ensembles with spatial size around 5–6 fm, that means we can restrict our attention to states with momenta $\ell_i \in \{0, \pm 1\}$. According to Eq. (3.6), the smallest group needed to construct these irreps has $N_s = 6$. The corresponding transfer-matrix symmetry group (Eq. (A32)) has only $|G_{T_0}(6)| = 82944$ elements.

The non-zero momentum irreps correspond to matrices of dimensions between 6 and 24, depending on the taste- and momentum-dimension. Happily, one does not need to construct and store matrices for each of the 82944 elements of the group. A smaller subset can be used to form the tensor product representations in Eq. (3.8) and decompose them into irreps. If this decomposition contains the taste singlet irrep of Eq. (3.8), we then compute the CGs.

For the first step, forming the tensor product representation and decomposing it, one needs only a representative element for each conjugacy class to perform the character decomposition [55]. For $N_s/2 = 3$, this corresponds to 404 classes. The second step, computing the CGs, is typically done by summing over all the group elements. However, for semi-direct product groups, the sum can be reduced by breaking up the group into subgroups and corresponding cosets [56]. The Clebsch-Gordan matrix U relates a tensor product representation to the block-diagonal reduced matrix D_R,

$$D^{(\alpha)}(g) \otimes D^{(\beta)}(g) = U D_R(g) U^\dagger, \qquad \forall g \in G. \tag{3.9}$$

where the two representations on the left correspond to the two single-pion representations on the LHS of Eq. (3.8). The approach to obtaining U, given in Ref. [56], is summarized by the following equation,

$$U = \text{unitarity: } \sum_{g \in G} \left[D^{(\alpha)}(g) \otimes D^{(\beta)}(g) \right] A D_R(g)^\dagger, \tag{3.10}$$

where A is a matrix of entries to be determined from the unitarity constraint. As mentioned, the staggered group has the natural structure (nested semi-direct product) to reduce this sum to one over subgroups and cosets. First, the cosets of the full staggered group under the subgroup $\Gamma_{4,1} \rtimes O_\mathrm{h}$ are obtained. This gives $(N_s/2)^3$ momentum cosets, with only one representative element from each coset needed. Then, the cosets of the group $\Gamma_{4,1} \rtimes O_\mathrm{h}$ under O_h are obtained, of which there are 64. So in total, for $N_s/2 = 3$, one needs only to store $27 + 64 + 48 = 139$ matrices for this step, where 48 is the order of O_h, the final

subgroup. The sum is thus reduced as

$$U = \text{unitarity:} \sum_{\tilde{z}\in\tilde{Z}^3_{N_s/2}} D(\tilde{z}) \left[\sum_{\tilde{\gamma}\in\tilde{\Gamma}_{4,1}} D(\tilde{\gamma}) \left[\sum_{o\in O_\text{h}} D(o) A D^\dagger(o) \right] D^\dagger(\tilde{\gamma}) \right] D^\dagger(\tilde{z}), \tag{3.11}$$

where the tilde, for example $\tilde{\Gamma}_{4,1}$, denotes the coset representatives of the corresponding set. Hence, in combination with the 404 class representative elements, the total number of essential matrices needed per irrep, for $N_s/2 = 3$, is around 500. This is a significant storage and computational cost reduction over the total order of the group.

To illustrate the steps outlined above, we perform the procedure for two specific cases of Eq. (3.8). The first is the case of the staggered pion irreps that are one-dimensional at zero momentum, i.e., the irreps of Eqs. (C27)–(C30). As taste singlets, they have the same CGs as Wilson fermions. The second case is for the staggered pion irreps that are three-dimensional at zero momentum, *i.e.*, the irreps of Eqs. (C31)–(C34). As described in Appendix A 3 a, these irreps can undergo "taste-orbit splitting" at non-zero momentum, typically, into a one- and two-dimensional taste-orbit irrep. The one-dimensional taste irrep is, again, akin to Wilson quarks, while the two-dimensional irrep is unique to staggered quarks.

To help illustrate these examples, we introduce the familiar notation for a general staggered operator with momentum and spin and taste quantum numbers Γ_S and Γ_T, respectively,

$$\mathcal{O}^{\Gamma_S\otimes\Gamma_T}(\ell_1, \ell_2, \ell_3), \tag{3.12}$$

which are described in Appendix A 4, with the precise meaning of this notation defined through Eqs. (A53)–(A57). The operators excite the states of the staggered irreps of Eq. (3.7). Hence, just as we label a staggered irrep by a single representative state of that irrep, as in Eq. (3.7), we can correspondingly label the irrep by a representative operator which excites this specific state. The correspondence between staggered irrep states and the operators which excite them is given by Eqs. (A58)–(A61). We denote this correspondence with the : symbol throughout the rest of this work, for example $\mathcal{O}^{\gamma_5\otimes\gamma_5}(0,0,1) \;:\; (0,0,1) \rtimes [(\pi,\pi,\pi,\pi),0] \rtimes A_0$ for the irrep with pseudoscalar spin and taste and one unit of momentum.

a. Example 1 For the first case, we take the above-mentioned pseudoscalar with one unit of momentum, Eq. (C38), as the representative example irrep. We have the following decomposition of the tensor product representation into irreps:

$$\begin{aligned}
&\mathcal{O}^{\gamma_5\otimes\gamma_5}(0,0,1) \otimes \mathcal{O}^{\gamma_5\otimes\gamma_5}(0,0,1) \;: \\
&(0,0,1) \rtimes [(\pi,\pi,\pi,\pi),0] \rtimes A_0 \otimes (0,0,1) \rtimes [(\pi,\pi,\pi,\pi),0] \rtimes A_0 \\
&= \; (0,0,0) \rtimes [(0,0,0,0),\pi] \rtimes A_0^+ \quad : \quad \mathcal{O}^{\gamma_0\otimes 1}(0,0,0) \\
&\oplus \; (0,0,0) \rtimes [(0,0,0,0),\pi] \rtimes E_0^+ \quad : \\
&\oplus \; (0,0,0) \rtimes [(0,0,0,0),\pi] \rtimes T_0^- \quad : \quad \mathcal{O}^{\gamma_i\otimes 1}(0,0,0) \\
&\oplus \; (0,0,1) \rtimes [(0,0,0,0),\pi] \rtimes A_0 \quad : \quad \mathcal{O}^{\gamma_3\otimes 1}(0,0,1) \\
&\oplus \; (1,1,0) \rtimes [(0,0,0,0),\pi] \rtimes A_0 \quad : \quad \mathcal{O}^{\gamma_0\otimes 1}(1,1,0) \\
&\oplus \; (1,1,0) \rtimes [(0,0,0,0),\pi] \rtimes A_2 \quad : \quad \mathcal{O}^{\gamma_1\gamma_2\otimes 1}(1,1,0).
\end{aligned} \tag{3.13}$$

TABLE I. Clebsch-Gordan table for $(0,0,1) \rtimes [(\pi,\pi,\pi,\pi),0] \rtimes A_0 \otimes (0,0,1) \rtimes [(\pi,\pi,\pi,\pi),\pi] \rtimes A_0 = (0,0,0) \rtimes [(0,0,0,0),\pi] \rtimes T_0^- \oplus \cdots$. The irreps in the rows and columns are labeled by the corresponding operators.

Tensor product row	$\mathcal{O}^{\gamma_1 \otimes 1}(0,0,0)$	$\mathcal{O}^{\gamma_2 \otimes 1}(0,0,0)$	$\mathcal{O}^{\gamma_3 \otimes 1}(0,0,0)$
$\mathcal{O}^{\gamma_5 \otimes \gamma_5}(1,0,0) \otimes \mathcal{O}^{\gamma_5 \otimes \gamma_5}(-1,0,0)$	$\frac{1}{\sqrt{2}}$	0	0
$\mathcal{O}^{\gamma_5 \otimes \gamma_5}(-1,0,0) \otimes \mathcal{O}^{\gamma_5 \otimes \gamma_5}(1,0,0)$	$-\frac{1}{\sqrt{2}}$	0	0
$\mathcal{O}^{\gamma_5 \otimes \gamma_5}(0,1,0) \otimes \mathcal{O}^{\gamma_5 \otimes \gamma_5}(0,-1,0)$	0	$\frac{1}{\sqrt{2}}$	0
$\mathcal{O}^{\gamma_5 \otimes \gamma_5}(0,-1,0) \otimes \mathcal{O}^{\gamma_5 \otimes \gamma_5}(0,1,0)$	0	$-\frac{1}{\sqrt{2}}$	0
$\mathcal{O}^{\gamma_5 \otimes \gamma_5}(0,0,1) \otimes \mathcal{O}^{\gamma_5 \otimes \gamma_5}(0,0,-1)$	0	0	$\frac{1}{\sqrt{2}}$
$\mathcal{O}^{\gamma_5 \otimes \gamma_5}(0,0,-1) \otimes \mathcal{O}^{\gamma_5 \otimes \gamma_5}(0,0,1)$	0	0	$-\frac{1}{\sqrt{2}}$

Here we have implicitly incorporated the form of Eq. (3.4) in the above direct product to ensure the desired staggered charge conjugation, $\xi_C = \pi$, is obtained in the decomposition. At zero momentum, there are $16 \times 16 = 256$ staggered bilinears and 448 irrep rows (states) in total (see Table VIII). Hence, some irreps, like the irrep including E_0^+ above, have no associated simple staggered bilinear which excite them. This irrep is instead excited by a more complicated staggered operator with a derivative insertion.

We are interested in the zero-momentum taste-singlet vector irrep which is the third irrep in the decomposition on the right-hand side of Eq. (3.13), with the corresponding operator $\mathcal{O}^{\gamma_i \otimes 1}(0,0,0)$. The CGs are computed for the states of this irrep using Eq. (3.10) and are given in Table I. For clarity, we use the more familiar, operators instead of the states to label the rows and columns in the table.

The two-pion operators are constructed from linear combinations of products of staggered single-pion operators with the CGs as coefficients. The staggered single-pion and two-pion operators are defined as

$$\pi^+_{\otimes\gamma_\xi}(\vec{p},t) \equiv -\frac{1}{N_S^{3/2}} \sum_{\vec{n}} e^{ia\vec{p}\cdot\vec{n}} \bar{d}(n)\gamma_5 \otimes \gamma_\xi u(n), \tag{3.14}$$

$$\pi^-_{\otimes\gamma_\xi}(\vec{p},t) \equiv \frac{1}{N_S^{3/2}} \sum_{\vec{n}} e^{ia\vec{p}\cdot\vec{n}} \bar{u}(n)\gamma_5 \otimes \gamma_\xi d(n), \tag{3.15}$$

$$\mathcal{O}_{\pi\pi}(\vec{p}_1+\vec{p}_2,t) \equiv \sum_{\xi_1,\xi_2,I_3^1,I_3^2,\vec{p}_1,\vec{p}_2} \mathrm{CG}_{G_{T_0},\,\mathrm{iso.}}(\xi_1,\xi_2,\vec{p}_1,\vec{p}_2,I_3^1,I_3^2)\pi^{I_3^1}_{\otimes\gamma_{\xi_1}}(\vec{p}_1,t)\pi^{I_3^2}_{\otimes\gamma_{\xi_2}}(\vec{p}_2,t). \tag{3.16}$$

Combining the results of Table I with Eq. (3.4) we obtained the normalized[5] staggered-isospin two-pion operator, built from $\otimes\gamma_5$ taste pions, that couples to the third component of the taste-singlet ρ^0:

$$\left[\mathcal{O}^{\otimes\gamma_5}_{\pi\pi}(\vec{0},t)\right]^{\gamma_3\otimes\gamma_1,\,I=1,I_3=0} = \frac{1}{\sqrt{2}}\left[\pi^+_{\otimes\gamma_5}((0,0,1),t)\,\pi^-_{\otimes\gamma_5}((0,0,-1),t) - \pi^-_{\otimes\gamma_5}((0,0,-1),t)\,\pi^+_{\otimes\gamma_5}(0,0,1),t)\right]. \tag{3.17}$$

[5] We are interested only in the overall overlap amplitudes of the ρ^0 operator, so are free to normalize the two-pion operators as we choose.

TABLE II. Clebsch-Gordan table for $(0,0,1) \rtimes [(0,0,\pi,0),0] \rtimes A_2 \otimes (0,0,1) \rtimes [(0,0,\pi,0),\pi] \rtimes A_2 = (0,0,0) \rtimes [(0,0,0,0),\pi] \rtimes T_0^- \oplus \cdots$. The irreps in the rows and columns are labeled by the corresponding operators.

Tensor product row	$\mathcal{O}^{\gamma_1 \otimes 1}(0,0,0)$	$\mathcal{O}^{\gamma_2 \otimes 1}(0,0,0)$	$\mathcal{O}^{\gamma_3 \otimes 1}(0,0,0)$
$\mathcal{O}^{\gamma_5 \otimes \gamma_5\gamma_2}(1,0,0) \otimes \mathcal{O}^{\gamma_5 \otimes \gamma_5\gamma_2}(-1,0,0)$	$\frac{1}{\sqrt{4}}$	0	0
$\mathcal{O}^{\gamma_5 \otimes \gamma_5\gamma_3}(1,0,0) \otimes \mathcal{O}^{\gamma_5 \otimes \gamma_5\gamma_3}(-1,0,0)$	$\frac{1}{\sqrt{4}}$	0	0
$\mathcal{O}^{\gamma_5 \otimes \gamma_5\gamma_2}(-1,0,0) \otimes \mathcal{O}^{\gamma_5 \otimes \gamma_5\gamma_2}(1,0,0)$	$-\frac{1}{\sqrt{4}}$	0	0
$\mathcal{O}^{\gamma_5 \otimes \gamma_5\gamma_3}(-1,0,0) \otimes \mathcal{O}^{\gamma_5 \otimes \gamma_5\gamma_3}(1,0,0)$	$-\frac{1}{\sqrt{4}}$	0	0
$\mathcal{O}^{\gamma_5 \otimes \gamma_5\gamma_3}(0,1,0) \otimes \mathcal{O}^{\gamma_5 \otimes \gamma_5\gamma_3}(0,-1,0)$	0	$\frac{1}{\sqrt{4}}$	0
$\mathcal{O}^{\gamma_5 \otimes \gamma_5\gamma_1}(0,1,0) \otimes \mathcal{O}^{\gamma_5 \otimes \gamma_5\gamma_1}(0,-1,0)$	0	$\frac{1}{\sqrt{4}}$	0
$\mathcal{O}^{\gamma_5 \otimes \gamma_5\gamma_3}(0,-1,0) \otimes \mathcal{O}^{\gamma_5 \otimes \gamma_5\gamma_3}(0,1,0)$	0	$-\frac{1}{\sqrt{4}}$	0
$\mathcal{O}^{\gamma_5 \otimes \gamma_5\gamma_1}(0,-1,0) \otimes \mathcal{O}^{\gamma_5 \otimes \gamma_5\gamma_1}(0,1,0)$	0	$-\frac{1}{\sqrt{4}}$	0
$\mathcal{O}^{\gamma_5 \otimes \gamma_5\gamma_1}(0,0,1) \otimes \mathcal{O}^{\gamma_5 \otimes \gamma_5\gamma_1}(0,0,-1)$	0	0	$\frac{1}{\sqrt{4}}$
$\mathcal{O}^{\gamma_5 \otimes \gamma_5\gamma_2}(0,0,1) \otimes \mathcal{O}^{\gamma_5 \otimes \gamma_5\gamma_2}(0,0,-1)$	0	0	$\frac{1}{\sqrt{4}}$
$\mathcal{O}^{\gamma_5 \otimes \gamma_5\gamma_1}(0,0,-1) \otimes \mathcal{O}^{\gamma_5 \otimes \gamma_5\gamma_1}(0,0,1)$	0	0	$-\frac{1}{\sqrt{4}}$
$\mathcal{O}^{\gamma_5 \otimes \gamma_5\gamma_2}(0,0,-1) \otimes \mathcal{O}^{\gamma_5 \otimes \gamma_5\gamma_2}(0,0,1)$	0	0	$-\frac{1}{\sqrt{4}}$

b. Example 2 Differences from the Wilson case appear only when one considers spin-pseudoscalar irreps that have a larger dimension than one at zero momentum. For example, starting with the taste pseudo-vector Eq. (C32), which is three-dimensional, giving it one unit of momentum and taking the irrep where taste orbit is two-dimensional as our starting point (second line of Eq. (C40)). Here the taste-vector is orthogonal to the momentum . The tensor product representation then has the following decomposition,

$$
\begin{aligned}
&\mathcal{O}^{\gamma_5 \otimes \gamma_5\gamma_{i\neq 3}}(0,0,1) \otimes \mathcal{O}^{\gamma_5 \otimes \gamma_5\gamma_{i\neq 3}}(0,0,1) \ : \\
&\qquad (0,0,1) \rtimes [(0,0,\pi,0),0] \rtimes A_2 \ \otimes \ (0,0,1) \rtimes [(0,0,\pi,0),0] \rtimes A_2 \\
&\qquad = \ (0,0,0) \rtimes [(0,0,0,0),\pi] \rtimes A_0^+ \ : \ \mathcal{O}^{\gamma_0 \otimes 1}(0,0,0) \\
&\qquad \oplus \ (0,0,0) \rtimes [(0,0,0,0),\pi] \rtimes E_0^+ \\
&\qquad \oplus \ (0,0,0) \rtimes [(0,0,0,0),\pi] \rtimes E_0^+ \\
&\qquad \oplus \ (0,0,0) \rtimes [(0,0,0,0),\pi] \rtimes E_0^+ \\
&\qquad \oplus \ (0,0,0) \rtimes [(0,0,0,0),\pi] \rtimes T_0^- \ : \ \mathcal{O}^{\gamma_i \otimes 1}(0,0,0) \\
&\qquad \oplus \ \ldots ,
\end{aligned}
\tag{3.18}
$$

where again we use the form of Eq. (3.4) to obtain the desired charge conjugation in the decomposition. There are now multiple copies of the same irrep appearing in the tensor product representation, as it corresponds to a $12 \times 12 = 144$ dimensional reducible matrix. The sixth irrep listed is the one we are after, and the CGs for this are given in Table II. When combining these results with Eq. (3.4), we obtain the following normalized two-pion

operator which couples to the third component of the taste-singlet ρ^0,

$$\left[\mathcal{O}_{\pi\pi}^{\otimes\,\gamma_5\gamma_{i\neq 3}}(\vec{0},t)\right]^{\gamma_3\otimes\gamma_1,\,I=1,I_3=0} = \\ \frac{1}{\sqrt{4}}\left[\pi^+_{\otimes\gamma_5\gamma_1}((0,0,1),t)\,\pi^-_{\otimes\gamma_5\gamma_1}((0,0,-1),t)+\pi^+_{\otimes\gamma_5\gamma_2}((0,0,1),t)\,\pi^-_{\otimes\gamma_5\gamma_2}((0,0,-1),t)\right. \\ \left.-\pi^-_{\otimes\gamma_5\gamma_1}((0,0,-1),t)\,\pi^+_{\otimes\gamma_5\gamma_1}(0,0,1),t)-\pi^-_{\otimes\gamma_5\gamma_2}((0,0,-1),t)\,\pi^+_{\otimes\gamma_5\gamma_2}(0,0,1),t)\right], \quad (3.19)$$

When computing the correlation functions of this operator and the ρ^0 operator that appear in the matrix of Eq. (2.14), all four terms in Eq. (3.19) give identical contributions to the correlation functions, which follows from the taste and rotation symmetry. However, for the $C(t)_{\pi\pi\to\pi\pi}$ correlation functions that also appear in Eq. (2.14), there are cross terms which are not equivalent. The Clebsch-Gordan coefficients for all the other cases (momentum and taste) are given in Appendix D.

B. Correlation functions

1. *Two-points*

With the operators in hand, the correlation functions in Eq. (2.14) can be constructed and the Wick contractions computed. The taste-singlet ρ^0 two-point correlation function, in the isospin-symmetric limit, is

$$C(t)_{\rho\to\rho} = \frac{1}{3}\sum_i \left\langle \rho_i^0(\vec{0},t)\rho_i^{0\dagger}(\vec{0},0)\right\rangle_{\text{conn.}} = \sum_n \left|\langle 0|\rho^0|n\rangle\right|^2 e^{-E_n t} \quad (3.20)$$

$$= 2\cdot\frac{1}{4}\cdot\frac{1}{4}\cdot\frac{1}{N_S^3}\cdot\frac{1}{3}\sum_i$$

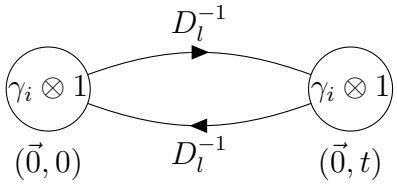

$$(3.21)$$

$$= \frac{1}{24N_S^3}\sum_{i,\vec{n}_0,\vec{n}_1,\{\pm\delta_j\}} \varphi^{\gamma_i\otimes 1}(n)\text{tr}\left[D_l^{-1}(\vec{n}_0+\delta^{\gamma_i\otimes 1},0|\vec{n}_1,t)D_l^{-1}(\vec{n}_1+\delta^{\gamma_i\otimes 1},t|\vec{n}_0,0)\right], \quad (3.22)$$

where D_l^{-1} are staggered light-quark propagators. The formulas for obtaining $\varphi(n)$ and δ from the spin and taste structure are given in Eqs. (A55) and (A56) with $\varphi^{\gamma_i\otimes 1}(n)$, $\delta^{\gamma_i\otimes 1}$ given explicitly in Eq. (A62). The $\{\pm\delta_j\}$ in the sum is a symmetrization over all components of each δ that appear. We leave the gauge fields implicit, with the trace just over the color index. The individual multiplicative factors are left explicit in the second line to illustrate the different sources of normalization. The factor of two arises from taking the isospin symmetric limit. The first factor of $\frac{1}{4}$ is from the operator normalization in Eq. (2.6), and the $1/N_S^3$ is from the Fourier transformation of these operators to momentum space. The second factor of $\frac{1}{4}$ comes from the staggered rooting procedure (Appendix E).

2. *Three-points*

The two-pion operators, Eqs. (3.17) and (3.19) and all others considered here, are built out of hermitian sub-operators of the form,

$$\mathcal{O}_{\pi\pi}^{\otimes\gamma_\xi}(\vec{0},t) = \pi^+_{\otimes\gamma_\xi}(\vec{p},t)\pi^-_{\otimes\gamma_\xi}(-\vec{p},t) - \pi^-_{\otimes\gamma_\xi}(\vec{p},t)\pi^+_{\otimes\gamma_\xi}(-\vec{p},t). \tag{3.23}$$

Hence, all correlation functions containing two-pion operators can be broken up into a linear combination of sub-correlation functions each containing an operator of this form. In following discussions, for simplicity, we just use Eq. (3.23) when computing the Wick contractions. The ρ operator, Eq. (2.6), at zero momentum is given by

$$\rho_i^0(\vec{0},t) = \frac{1}{2N_S^{3/2}}\sum_{\vec{n}} \bar{u}(n)\gamma_i \otimes 1\, u(n) - \bar{d}(n)\gamma_i \otimes 1\, d(n) \tag{3.24}$$

The $C(t)_{\pi\pi\to\rho}$ three-point function, in the isospin symmetric limit, is then

$$C(t)_{\pi\pi\to\rho} = \frac{1}{3}\sum_i \left\langle \rho_i^0(\vec{0},t)\mathcal{O}_{\pi\pi}^{\otimes\gamma_\xi}(\vec{0},0)\right\rangle = \sum_n \langle 0|\rho^0|n\rangle\langle n|\mathcal{O}_{\pi\pi}^{\otimes\gamma_\xi}|0\rangle e^{-E_n t} \tag{3.25}$$

$$= 4\cdot\frac{1}{2}\cdot\frac{1}{4}\cdot\frac{1}{N_S^{9/2}}\cdot\frac{1}{3}\sum_i$$

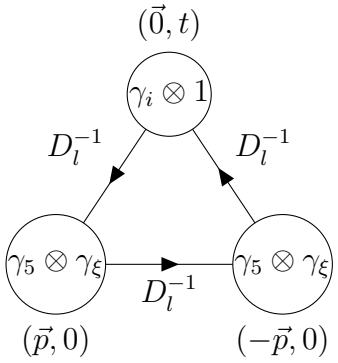

(3.26)

$$= \frac{1}{6N_S^{9/2}}\sum_{i,\vec{n}_0,\vec{n}_1,\vec{n}_2,\{\pm\delta_j\}} \varphi^{\gamma_5\otimes\gamma_\xi}(n_0)\varphi^{\gamma_5\otimes\gamma_\xi}(n_1)\varphi^{\gamma_i\otimes 1}(n_2)e^{ia\vec{p}\cdot(\vec{n}_0-\vec{n}_1)}$$
$$\times \mathrm{tr}\left[D_l^{-1}(\vec{n}_0+\delta^{\gamma_5\otimes\gamma_\xi},0|\vec{n}_1,0)D_l^{-1}(\vec{n}_1+\delta^{\gamma_5\otimes\gamma_\xi},0|\vec{n}_2,t)D_l^{-1}(\vec{n}_2+\delta^{\gamma_i\otimes 1},t|\vec{n}_0,0)\right]. \tag{3.27}$$

Disconnected Wick contributions cancel in the isospin symmetric limit. The factor of four in the second line comes from four connected Wick contractions, of which we only show one, which are all equivalent under isospin and parity. The $\frac{1}{2}$ is the normalization from the ρ^0 operator, and the $\frac{1}{4}$ is from the rooting procedure. The factor of $1/N_S^{9/2}$ arises from the Fourier transform of the three operators. We do not generate the $C(t)_{\rho\to\pi\pi}$ correlation functions, because they are significantly noisier with the random-wall source approach used here (see Sec. III D), and it is equivalent to $C(t)_{\pi\pi\to\rho}$ under time-reversal symmetry.

3. *Four-points*

The $\pi\pi\to\pi\pi$ four point function, in the isospin-symmetric limit, is

$$C(t)_{\pi\pi\to\pi\pi} = \left\langle \mathcal{O}_{\pi\pi}^{\otimes\gamma_{\xi_2}}(\vec{0},t)\mathcal{O}_{\pi\pi}^{\otimes\gamma_{\xi_1},\dagger}(\vec{0},0)\right\rangle = \sum_n \langle 0|\mathcal{O}_{\pi\pi}^{\otimes\gamma_{\xi_2}}|n\rangle\langle n|\mathcal{O}_{\pi\pi}^{\otimes\gamma_{\xi_1}}|0\rangle e^{-E_n t} \tag{3.28}$$

$$= -4 \cdot \frac{1}{4} \cdot \frac{1}{N_S^6} \times$$

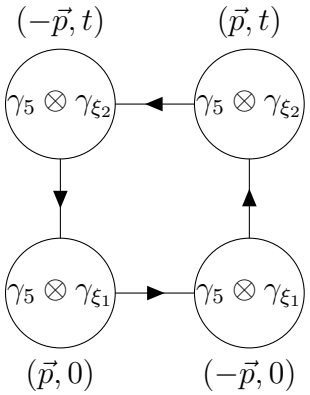

$$+ 4 \cdot \frac{1}{4} \cdot \frac{1}{N_S^6} \times$$

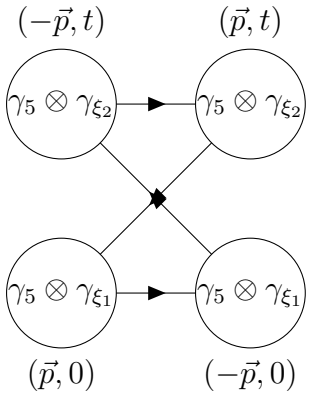

$$+ 2 \cdot \frac{1}{16} \cdot \frac{1}{N_S^6} \times$$

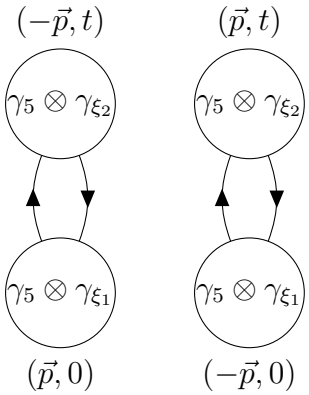

$$- 2 \cdot \frac{1}{16} \cdot \frac{1}{N_S^6} \times$$

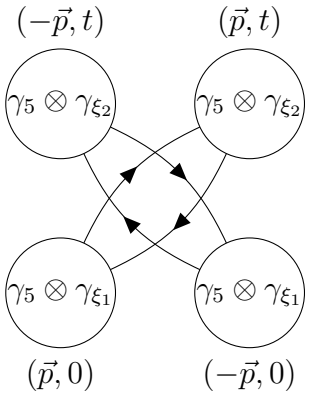

,

$$\begin{aligned}
= \frac{1}{N_S^6} \sum_{\vec{n}_0,\vec{n}_1,\vec{n}_2,\vec{n}_3,\{\pm\delta_j\}} & \varphi^{\gamma_5\otimes\gamma_{\xi_1}}(n_0)\varphi^{\gamma_5\otimes\gamma_{\xi_1}}(n_1)\varphi^{\gamma_5\otimes\gamma_{\xi_2}}(n_2)\varphi^{\gamma_5\otimes\gamma_{\xi_2}}(n_3)e^{ia\vec{p}\cdot(\vec{n}_0-\vec{n}_1+\vec{n}_2-\vec{n}_3)}\Big[\\
& - \mathrm{tr}\left[D_l^{-1}(\vec{n}_0+\delta^{\gamma_5\otimes\gamma_{\xi_1}},0|\vec{n}_1,0)D_l^{-1}(\vec{n}_1+\delta^{\gamma_5\otimes\gamma_{\xi_1}},0|\vec{n}_2,t)\right. \\
& \quad \left.\times D_l^{-1}(\vec{n}_2+\delta^{\gamma_5\otimes\gamma_{\xi_2}},t|\vec{n}_3,t)D_l^{-1}(\vec{n}_3+\delta^{\gamma_5\otimes\gamma_{\xi_2}},t|\vec{n}_0,0)\right] \\
& + \mathrm{tr}\left[D_l^{-1}(\vec{n}_0+\delta^{\gamma_5\otimes\gamma_{\xi_1}},0|\vec{n}_1,0)D_l^{-1}(\vec{n}_1+\delta^{\gamma_5\otimes\gamma_{\xi_1}},0|\vec{n}_3,t)\right. \\
& \quad \left.\times D_l^{-1}(\vec{n}_3+\delta^{\gamma_5\otimes\gamma_{\xi_2}},t|\vec{n}_2,t)D_l^{-1}(\vec{n}_2+\delta^{\gamma_5\otimes\gamma_{\xi_2}},t|\vec{n}_0,0)\right] \\
& + \frac{1}{8}\mathrm{tr}\left[D_l^{-1}(\vec{n}_0+\delta^{\gamma_5\otimes\gamma_{\xi_1}},0|\vec{n}_2,t)D_l^{-1}(\vec{n}_2+\delta^{\gamma_5\otimes\gamma_{\xi_2}},t|\vec{n}_0,0)\right] \\
& \quad \times \mathrm{tr}\left[D_l^{-1}(\vec{n}_1+\delta^{\gamma_5\otimes\gamma_{\xi_1}},0|\vec{n}_3,t)D_l^{-1}(\vec{n}_3+\delta^{\gamma_5\otimes\gamma_{\xi_2}},t|\vec{n}_1,0)\right] \\
& - \frac{1}{8}\mathrm{tr}\left[D_l^{-1}(\vec{n}_0+\delta^{\gamma_5\otimes\gamma_{\xi_1}},0|\vec{n}_3,t)D_l^{-1}(\vec{n}_3+\delta^{\gamma_5\otimes\gamma_{\xi_2}},t|\vec{n}_0,0)\right] \\
& \quad \times \mathrm{tr}\left[D_l^{-1}(\vec{n}_1+\delta^{\gamma_5\otimes\gamma_{\xi_1}},0|\vec{n}_2,t)D_l^{-1}(\vec{n}_2+\delta^{\gamma_5\otimes\gamma_{\xi_2}},t|\vec{n}_1,0)\right]\Big]. \qquad (3.29)
\end{aligned}$$

The individual factors of $4, 4, 2, 2$ in front of the respective diagrams are independent-diagram multiplicities. The $\frac{1}{4}, \frac{1}{4}, \frac{1}{16}, \frac{1}{16}$ are rooting factors ($\frac{1}{4}$ for each trace).

The numerical simulation presented here actually employs time-split two-pion operators instead of Eq. (3.28) to address a potential Fierz-rearrangement issue discussed in Ref. [57]. This modification and the additional considerations it introduces are described in Appendix F. It turns out that the Fierz-rearrangement problem does not arise with the random-wall sources used in this work, hence our ongoing studies employ Eq. (3.28).

TABLE III. Operator basis on the $a \approx 0.15$ fm ensemble. The single pion operators in the two-pion states have equal taste and equal-but-opposite momentum. We indicate the irrep splitting by listing the operators separately.

Operator	Momenta (back-to-back)
ρ^0, $\tilde{\rho}^0$	
$\mathcal{O}_{\pi\pi}^{\otimes\gamma_5}$	$(0,0,1),(1,1,0)$
$\mathcal{O}_{\pi\pi}^{\otimes\gamma_5\gamma_{1/2}}$, $\mathcal{O}_{\pi\pi}^{\otimes\gamma_5\gamma_3}$	$(0,0,1)$
$\mathcal{O}_{\pi\pi}^{\otimes\gamma_{1/2}\gamma_0}$, $\mathcal{O}_{\pi\pi}^{\otimes\gamma_3\gamma_0}$	$(0,0,1)$

4. *Effective energies and amplitudes*

We make use of the following formula for extracting the effective energy and amplitudes from the correlation functions used in this work. The effective energy is obtained from

$$aE_{0,\text{eff}}(t) = \frac{1}{2}\,\text{arccosh}\left[\frac{C(t+2)+C(t-2)}{2C(t)}\right], \tag{3.30}$$

where the averaging is performed over a time separations of $(t \pm 2)$ to remove staggered oscillatory effects. The effective amplitude is then given by the following,

$$Z^2_{0,\text{eff}}(t) = e^{N_t E_{0,\text{eff}}/2}\frac{C(t)}{\cosh(E_{0,\text{eff}}(N_t/2-t))}, \tag{3.31}$$

where the parameter $E_{0,\text{eff}}$ is obtained from Eq. (3.30), once the function has plateaued.

C. Choosing the operator basis

For the two-pion operators in the matrix, Eq. (2.14), we choose a range of pion momenta and tastes corresponding to two-pion energies up to the mass of the ρ^0 meson [59]. For this purpose, we construct the non-interacting two-pion energies using

$$E_{\text{free}} = 2\sqrt{\vec{p}^2 + M_\xi^2}, \tag{3.32}$$

where M_ξ are the measured ground-state masses of pion correlation functions obtained from Eqs. (C27)–(C34) and $p_i = 2\pi\ell_i/L$, $\ell_i = 0, 1\ldots$. This spectrum is shown in Fig. 1 for the four physical mass HISQ ensembles currently used in related $g-2$ work from the Fermilab Lattice, HPQCD and MILC Collaborations [28]. Figure 1 does not account for interactions or the taste-orbit splittings described in Appendix A 3 a, but suffices for deciding which $\pi\pi$ operators to use.

At 0.15 fm, which is the focus of this work, we see there are four states below or near the threshold. We include the taste-tensor (red cross) even though it is above the ρ^0 mass. We select an eight-operator basis, shown in Table III. From the irreps listed in Eqs. (C27)–(C34), we leave out operators for the taste pseudo-vector with a temporal taste component, Eq. (C28), and the taste tensors without a temporal taste component Eq. (C34). This choice is based on the fact these operators, in the form of $\mathcal{O}^{\gamma_5\otimes\xi}$, have links in the time-direction. Averaging over the forward and backward time-links removes the oscillating contribution,

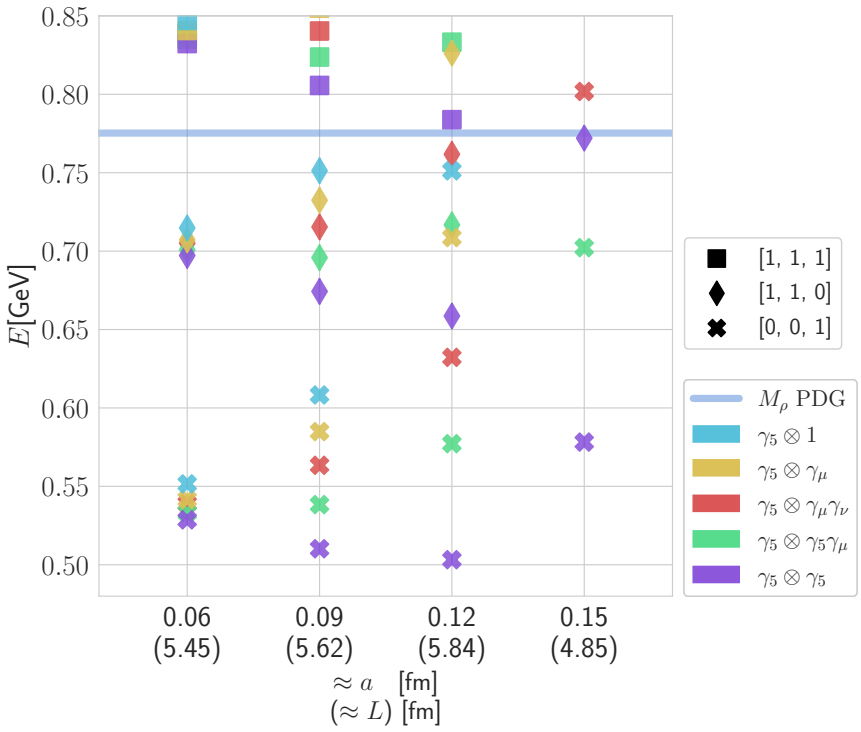

FIG. 1. Continuum, non-interacting energy spectrum for $\pi_\xi\pi_\xi \to \rho$ case on four physical-mass HISQ ensembles for the relevant tastes, ξ. The ensembles' parameters are given in Ref. [28]. The tastes of the single pions in the two-pion state are indicated by the color. The back-to-back momentum is indicated by the symbol shape. Also given is the ρ^0 Particle Data Group mass (blue band) [58] which is used as the cut-off energy to select the operator basis.

but results in non-local time dependence in the corresponding correlation functions. The time-link can be removed by modifying the operators as $\mathcal{O}^{\gamma_5\otimes\xi} \to \mathcal{O}^{\gamma_5\gamma_0\otimes\xi}$, which preserves the original quantum numbers (see Eq. (A64)). We generate additional correlation functions with these modified operators to check that the variational basis in Table III is complete, *i.e.*, to check that including them does not resolve any additional states beneath the threshold. This is expected based on the degeneracy's at zero-momentum, and confirmed in our analysis. These $\mathcal{O}^{\gamma_5\gamma_0\otimes\xi}$ operators, however, are found to have significant overlap with excited states, resulting in very noisy correlation functions; hence, they are not included in the main analysis presented here.

D. Numerical setup

The 0.15 fm HISQ ensemble parameters are given in Table IV. We use the same numerical strategy as described in Ref. [28] for the two-point correlation functions in Eqs. (3.22) and (3.29). For the three-point, Eq. (3.27), and single-trace four-point contractions of Eq. (3.29), we employ sequential sources [62]. For these four-point contractions, this approach requires an additional solve for each time separation in the correlation function. To

TABLE IV. Ensemble parameters used in this work; from Ref. [27]. Shown are the approximate lattice spacing in fm, the spatial length L of the lattice in fm, the size of the lattice, the sea-quark masses in lattice-spacing units, the gradient-flow scale w_0/a [27, 60], the taste-Goldstone pion mass [46], the number of configurations analyzed, the number of loose-residual solves per configuration used in the truncated solver method [31, 32], and the time-slice range computed for the four point functions. We take $w_0 = 0.1715(9)$ fm [61].

$\approx a$ (fm)	L (fm)	$N_s^3 \times N_t$	$am_l^{\rm sea}/am_s^{\rm sea}/am_c^{\rm sea}$	w_0/a	M_{π_5} (MeV)	$N_{\rm conf}$	$N_{\rm loose}$	$t_{\rm sep}$
0.15	4.85	$32^3 \times 48$	0.002426/0.0673/0.8447	1.13215(35)	134.73(71)	3473	16	[3,17]

reduce computational expense, we generate a subset of the total possible time separations, which are shown in the last column of Table IV. The total number of configurations for which we compute the correlation matrix Eq. (2.14) is given in the third-to-last column of Table IV. We calculate two-point correlators Eq. (3.22) on ≈ 6000 additional configurations, as the reconstructed tail accounts for only about $\approx 20\%$ of the total value of the integrand, Eq. (2.3), with the rest coming from the two-point data. We renormalize the vector operator using the results from Ref. [63]. Uncertainties are propagated through the analysis using the GVAR package [64]. We find that the GVAR uncertainties are in excellent agreement with jackknife resampling, while being computationally faster.

E. Finite time effects

A complication which must be addressed with the matrix Eq. (2.14) is the wrap-around contribution that arises in the diagonal $C(t)_{\pi\pi\to\pi\pi}$ correlation functions due to the finite temporal size of the lattice employed. In general, the spectral decomposition of $C(t) = \langle \mathcal{O}(t)\mathcal{O}^\dagger(0)\rangle$ is

$$C(t) = \frac{1}{Z}\sum_{mn}\langle m|\hat{\mathcal{O}}|n\rangle\langle n|\hat{\mathcal{O}}^\dagger|m\rangle e^{-E_n t - E_m(T-t)}, \tag{3.33}$$

$$Z = \sum_n e^{-E_n T}, \tag{3.34}$$

with the states ordered by increasing energy $E_0 < E_1 \leq E_2 \leq \cdots$. In the case of interest here, the $T < \infty$ correction from Z will be absorbed into the amplitudes $\langle m|\hat{\mathcal{O}}^{(\dagger)}|n\rangle$. The leading correction to $C(t)$ comes from $m = 1$ or $n = 1$, namely

$$\begin{aligned} C(t) = \cdots + e^{-E_1 T}\sum_{m\neq 0}\langle 1|\hat{\mathcal{O}}|n\rangle\langle n|\hat{\mathcal{O}}^\dagger|1\rangle e^{-(E_n-E_1)t} + \\ e^{-E_1 T}\sum_{n\neq 0}\langle 1|\hat{\mathcal{O}}^\dagger|m\rangle\langle m|\hat{\mathcal{O}}|1\rangle e^{-(E_m-E_1)(T-t)} + \cdots . \end{aligned} \tag{3.35}$$

After the vacuum, the lowest-energy states are the pions. For $|1\rangle = |\pi^0\rangle$, the two-pion operator $\mathcal{O}_{\pi^+\pi^-}$ connects to states like $|\pi^0\pi^+\pi^-\rangle$. For $|1\rangle = |\pi^\pm\rangle$, however, the intermediate state can also be $|\pi^\pm\rangle$. In this case, the t dependence drops out:

$$C(t) = \cdots + 2e^{-E_{\pi^\pm} T}\langle \pi^\pm|\hat{\mathcal{O}}_{\pi^+\pi^-}|\pi^\pm\rangle\langle\pi^\pm|\hat{\mathcal{O}}^\dagger_{\pi^+\pi^-}|\pi^\pm\rangle + \cdots , \tag{3.36}$$

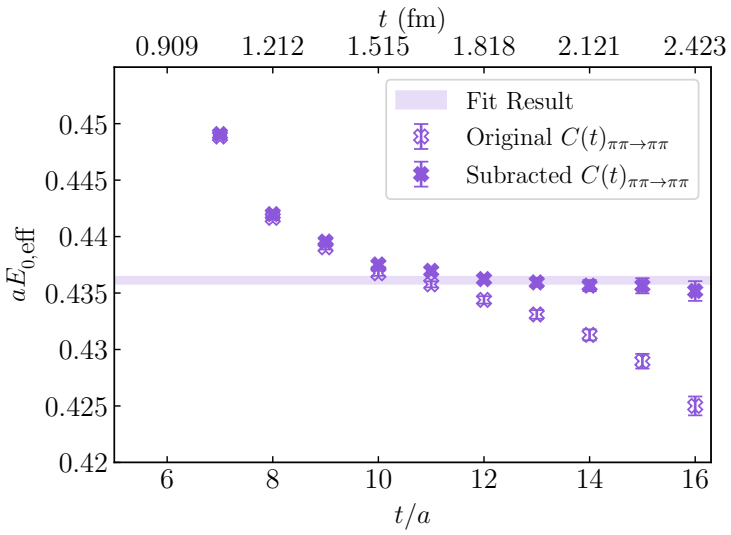

FIG. 2. Effective mass of the correlation function $C(t)_{\pi\pi\to\pi\pi} : \langle \mathcal{O}^{\otimes\gamma_5}_{\pi\pi}(\vec{0},t)\mathcal{O}^{\otimes\gamma_5}_{\pi\pi}(\vec{0},0)\rangle$ uncorrected (empty) and corrected (filled) purple crosses for the wrap around contribution using the method described in this section. Also shown is the result of a fit to corrected correlation function.

with the factor of 2 arising from both contributions in Eq. (3.35) contributing equally. If $\mathcal{O}_{\pi\pi}$ contains pions with back-to-back momentum $\vec{p}$, then the relevant state for Eq. (3.36) is $|\pi(\vec{p})\rangle$. With the weakly-interacting approximation [65],

$$\langle \pi^{\pm}|\hat{\mathcal{O}}_{\pi^+\pi^-}|\pi^{\pm}\rangle \approx \left|\langle 0|\pi^{\pm}\big|\pi^{\pm}\rangle\right|^2, \tag{3.37}$$

the constant term $2\left|\langle 0\big|\pi^{\pm}\big|\pi^{\pm}\rangle\right|^4 e^{-E_{\pi^{\pm}}T}$ is then the leading wrap-around contribution. While this t-independent term is formally small, it is not small in practice in the region of interest, where t is a bit shorter than $T/2$. This contribution is especially relevant for this calculation as T on the 0.15 fm physical mass HISQ ensemble is ≈ 0.8 fm smaller than on the other HISQ ensembles in Fig. 1.

We explicitly subtract this term from the diagonal correlators in Eq. (2.14) after obtaining $\langle 0\big|\pi^{\pm}\big|\pi^{\pm}\rangle$ and $E_{\pi^{\pm}}$ from a fit to the single-pion two-point correlation functions (third diagram in Eq. (3.29)). Shown in Fig. 2 is the result of applying this procedure to the ground state correlation function $\langle \mathcal{O}^{\otimes\gamma_5}_{\pi\pi}(\vec{0},t)\mathcal{O}^{\otimes\gamma_5}_{\pi\pi}(\vec{0},0)\rangle$, where we plot the effective energy, Eq. (3.30), for the original and subtracted correlation functions.

In the limit $t \to \infty \sim T/2$, the effective energy, $aE_{0,\text{eff}}(t)$, should plateau to the ground state energy if there is no constant term. From the plot, one sees this is indeed the case for the subtracted version. Moreover, the effective energy of the subtracted correlation function now agrees with the fit result (purple band), while the unsubtracted effective energy shows clear contamination from the wrap-around contribution. All following results use the subtracted version of Eq. (2.14) in which the diagonal two-pion correlators are replaced with the versions that have the leading wrap-around contribution subtracted.

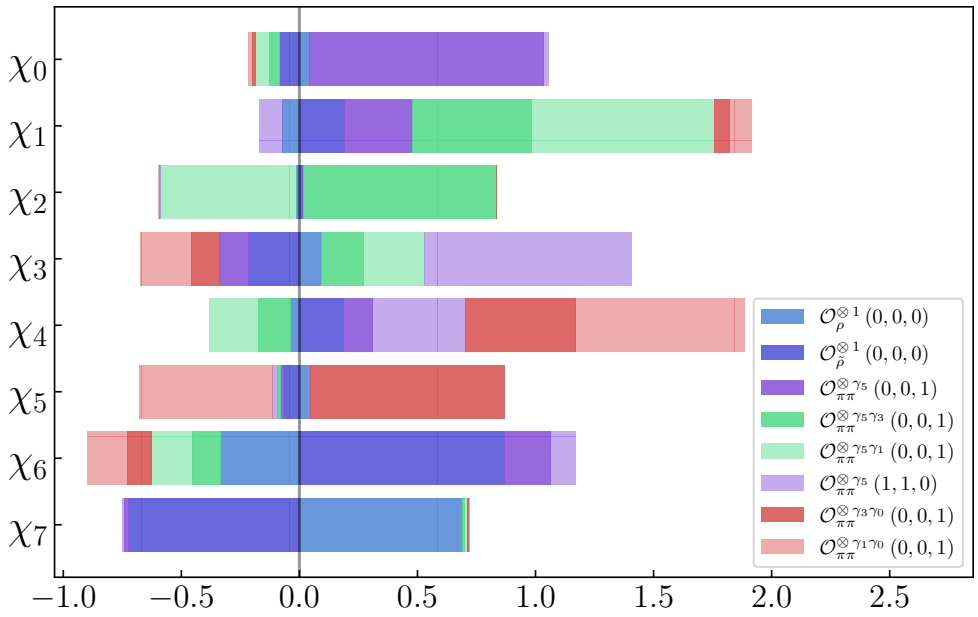

FIG. 3. Qualitative picture of the composition of the optimized operators χ_n as constructed from the original operator basis in Table III for a value of $t_0/a = 5$. The picture is qualitative, as the operators all must be normalized to some common value. This is achieved by setting their corresponding diagonal correlation functions equal at a reference time t. Here $t/a = 10$ is chosen, the picture varies slightly depending on the choice of reference time. The horizontal line divides the negative and positive contributions to the optimized operators[a].

F. The GEVP and optimized operators

To obtain the energies and amplitudes from the matrix, Eq. (2.14), eigenvectors $v_n(t, t_0)$ are first extracted through a generalized eigenvalue problem (GEVP) [66],

$$\mathbf{C}(t)v = \lambda \mathbf{C}(t_0)v. \tag{3.38}$$

Here, the reference time t_0 is a free parameter, which we vary later in the analysis to check for stability. A smaller value of t_0 yields eigenvectors and eigenvalues with better statistical precision, albeit with potentially larger excited state contamination. The resulting $v_n(t)$ are functions of Euclidean time. Their asymptotic values, v_n, at large enough $t = t'$ are the coefficients of the 'optimized operators' [67]. We find that at $t'/a = 10$ all the $v_n(t)$ appear to have plateaued to constants. The optimized operators with maximal overlap with the states $|n\rangle$ are, then:

$$\chi_n(t) = \sum_i (v_n)_i \, \mathcal{O}_i(t). \tag{3.39}$$

Figure 3 provides a visual display of the components of v_n for the full operator basis in Table III. In the plot, the relative contributions of the original operators to the χ_n are shown. For this purpose, the original operators are first normalized, so their diagonal correlators are equal at time $t/a = 10$. One observes that the ground state optimized operator, χ_0, is predominantly made up of $\mathcal{O}_{\pi\pi}^{\otimes\gamma_5}$ with $(0, 0, 1)$ back-to-back momenta as expected. The

TABLE V. Fit parameters used to extract energies and amplitudes from Eqs. (3.40) and (3.41). The D (diagonal) and OD (off-diagonal) labels correspond to the first and second equations, respectively. We display the fit quality through the χ^2/DoF value, which does not include the contribution from priors. We also display the BAIC weight [68], which we use to select these preferred fit parameters over other variations.

state	$t_{\text{min, D}}/a$	$t_{\text{max, D}}/a$	$t_{\text{min, OD}}/a$	$t_{\text{max, OD}}/a$	(N_{states}, $N_{\text{osc. states}}$)	χ^2/DoF	BAIC
0	6	18	6	20	(2, 1)	0.54	66.2
1	6	18	6	20	(2, 1)	0.65	68.3
2	6	16	6	20	(2, 1)	0.91	75.4
3	6	18	6	20	(2, 1)	0.66	68.6
4	6	18	6	20	(2, 1)	0.79	71.0
5	6	18	6	19	(2, 1)	0.84	73.2
6	6	18	6	20	(2, 1)	0.66	68.5

first and second excited states are primarily built out of the taste-pseudo vector, one-link operators, where the first excited state is an additive combination while the second is subtractive. The third operator is primarily the $\mathcal{O}_{\pi\pi}^{\otimes\gamma_5}$ operator with $[1,1,0]$ momentum, but with significant mixing from the other taste operators. The fourth and fifth are analogous to the first and second but for the taste-tensor, two-link operators. The sixth is primarily the smeared ρ^0 operator and the last is essentially a "junk" operator with the normal and smeared ρ^0 operators almost cancelling out.

The lowest energies E_n and overlap amplitudes $\langle 0|\rho^0|n\rangle$, that appear in Eq. (2.10), are obtained from the following correlation functions constructed from the optimized operators

$$v_n^\dagger \mathbf{C}(t) v_n = \left\langle \chi_n(t) \chi_n^\dagger(0) \right\rangle = \sum_n \left[Z_n^2 e^{-E_n t} + (-1)^t Z_{n,\text{osc}}^2 e^{-E_{n,\text{osc}} t} \right], \tag{3.40}$$

$$(\mathbf{C}(t) v_n)_0 = \left\langle \chi_n(t)\, \rho^{0\dagger}(0) \right\rangle = \sum_n \left[Z_n \left\langle 0 \left| \rho^0 \right| n \right\rangle e^{-E_n t} + (-1)^t Z_{n,\text{osc}} \left\langle 0 \left| \rho^0 \right| n, \text{osc} \right\rangle e^{-E_{n,\text{osc}} t} \right]. \tag{3.41}$$

The $t \to T - t$ terms, from periodic boundary conditions, in the spectral representation are implicit. In the following sections, we will also consider variations of the original operator basis which do not contain the ρ^0, in this case we simply pad the v_n with a zero as the first element so that these formulas still hold.

1. *Extracting the energies and amplitudes*

In order to extract the energies and amplitudes from Eqs. (3.40) and (3.41), we perform a combined fit to the functional forms on the right-hand side of these equations, including the $t \to T - t$ contributions. The sum is truncated with independent limits for the regular and oscillating states, N_{states} and $N_{\text{osc. states}}$. With a Bayesian fit approach, we use prior information for the ground state energies and overlap amplitudes extracted from the plateaus of the effective energy, Eq. (3.30), and amplitude, Eq. (3.31). These effective energies and amplitudes are shown in Fig. 4. We take the results of these as estimates for the prior central values and assign a 20% width. The effective amplitude for $\langle 0 \left| \rho^0 \right| n \rangle$ is obtained by taking

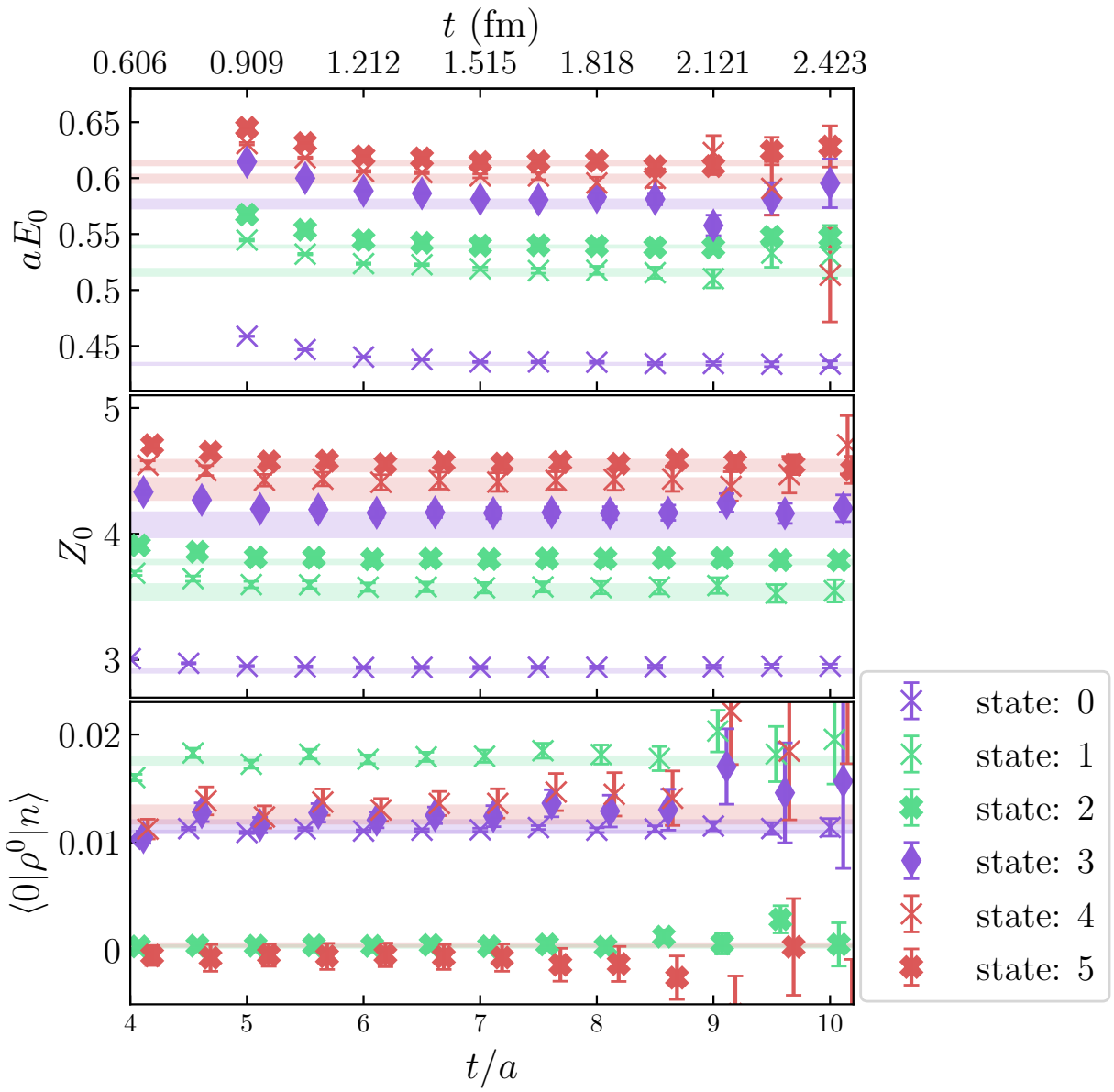

FIG. 4. Energies (top), optimized operator overlap amplitudes (middle) and ρ^0 operator overlap amplitudes (bottom) for the two-pion states, extracted from a generalized eigenvalue analysis on the ≈ 0.15 fm ensemble with $t_0/a = 5$. Bands are results from fits, data points are effective masses and amplitudes. The sixth state is left out due to the significant oscillations and overlapping error bands, rendering the plot unclear.

a ratio of the respective effective amplitudes of Eqs. (3.40) and (3.41). We use a prior of $\Delta E = 0.5(0.5)$ GeV for the energy splitting to higher states. The higher-state amplitudes are given the same prior as the ground state but with 100% widths. These higher state priors have little effect on the fits beyond helping with stability in some cases. Fits are performed up to $N_{\text{states}} \leq 3$ and $N_{\text{osc. states}} \leq N_{\text{states}}$ but we find that states beyond the first excited state and the first oscillating state are not well determined, even when including the earliest time-slices. Additionally, we vary t_{min} and t_{max} independently on the two datasets

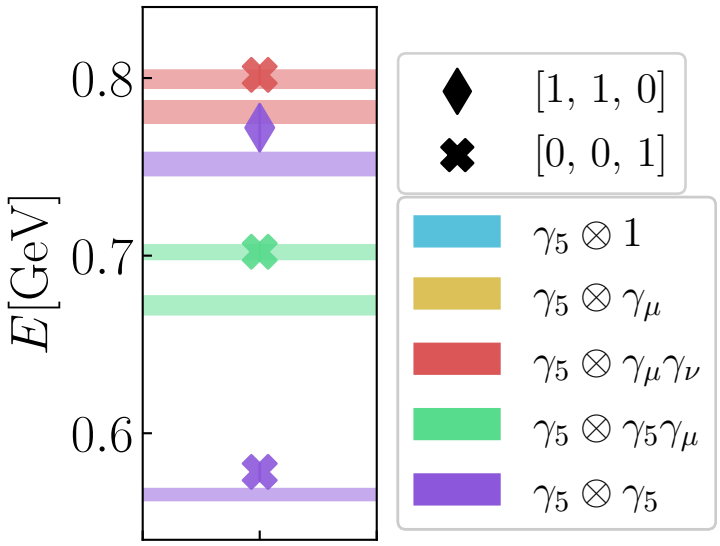

FIG. 5. Comparison of the free continuum spectrum of Fig. 1 (symbols) with the interacting spectrum of Fig. 4 (bands).

for Eqs. (3.40) and (3.41). This is beneficial as the two correlation functions have differing excited state contamination and noise-to-signal profiles. The stability of the fit results with respect to these parameter variations (as well as t_0 and operator basis variation) is discussed in Sec. IV A 1. In order to select our preferred set of fit parameters, we simply choose the fit for each n with the highest weight according to the Bayesian Akaike information criterion (BAIC) [68]. In general, they correspond to what one would obtain from a more traditional 'stability analysis,' i.e., the lowest t_{min} and highest t_{max} in the region of fit stability. Applying a full model-averaging procedure, discussed in Ref. [68], yields consistent results. Table V lists the fit parameters for our preferred reference time $t_0/a = 5$ (reasoning discussed in Sec. IV A 1).

IV. RESULTS

A. Staggered two-pion spectrum

In Fig. 4 we show the resultant GEVP fit energies and amplitudes for the first six states as color-coded bands. We find, as expected, that they agree very well with the effective mass and effective amplitude plateaus shown in this plot. We also find similar consistency for the highest well-determined state, $n = 6$, which is not shown here [6] as it renders the plot unclear. In Fig. 5 we compare the free, continuum energy spectrum (symbols) with these extracted energies (bands). We find that the ground state interacting energy (purple band) is roughly 2% smaller than that of the free case. The expected taste-orbit splitting can be seen in the two-pion states built from the zero-momentum, three-dimensional single-pion irreps, Eqs. (C40) and (C42). We see that these states, namely, $n = 1$ and 2, and $n = 4$ and 5 are non-degenerate. Of these, the two-pion states containing pions that are two-dimensional

[6] The $n = 6$ state is included in the displayed spectra of Figs. 6 and 7.

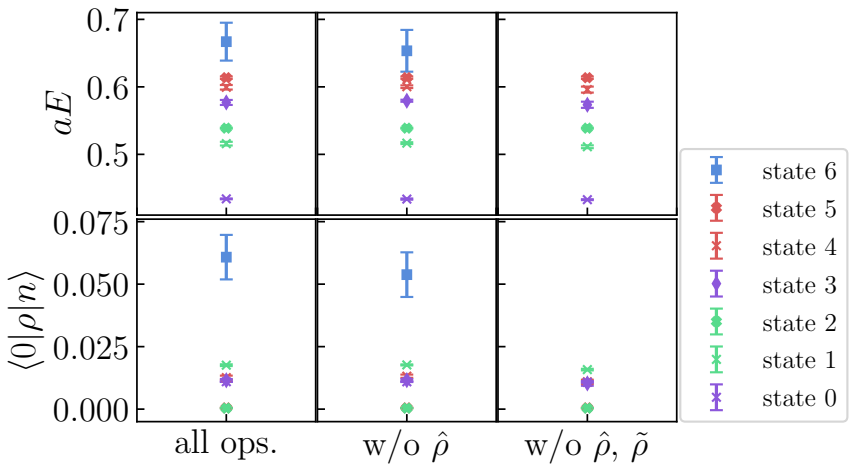

FIG. 6. GEVP spectrum comparison for three different operator bases. The first is the full eight-operator basis, the second contains seven operators with the ρ^0 operator dropped, and the third has six operators with both the ρ^0 and $\tilde{\rho}^0$ omitted.

in the taste dimension are strongly interacting, while the opposite is true for the states that are one-dimensional (see Fig. 3). This enhanced (suppressed) interaction results in a larger (smaller) binding energy, and larger (smaller) overlap amplitudes, as seen in Fig. 4 (bottom panel).

1. *Stability*

There are many choices that need to be made in order to arrive at a finalized energy spectrum and, hence, reconstruction of the vector-current correlation function and value for a_μ^{ll}(conn.), namely, the choice the operator basis, the reference time t_0, asymptotic time t', and the fit parameters for the optimized correlation functions, Eqs. (3.40) and (3.41), of which there are two sets of $t_{\rm min}$ and $t_{\rm max}$ for each n. Our selections are made as objectively as possible, using the BAIC weight, and after checking for stability under reasonable variations, among other considerations.

We first consider variations in the operator basis by dropping the ρ^0 operators. In Fig. 6, from left to right, we observe stability in the energies and amplitudes of the first six states as we drop first the ρ^0 operator (middle panel) and then the $\tilde{\rho}^0$ operator (right panel) from the basis. The energy and amplitude of the seventh state, $n = 6$, changes slightly, albeit well within the uncertainty when the ρ^0 is omitted, which is not surprising given that the operator used to resolve it contains a significant contribution from the ρ^0 (see Fig. 3). As is well known, to obtain a reliable spectral decomposition of the first n states, at least $n + 1$ independent operators (correlators) are needed. Hence, in our following reconstructions of the vector current, which include the $n = 7$ state, we use the full eight operator basis.

In the left-hand side of Fig. 7, we show the eigenvector (top) and corresponding energy, extracted from the eigenvalue for the $n = 2$ state as function of t_0. The full resultant spectrum for the same values of t_0 is shown in the right-hand side of Fig. 7. The spectra are broadly consistent with each other as t_0 is varied with the $n = 6$ state showing some fluctuation, although still being comfortably within uncertainties. We choose $t_0/a = 5$ as

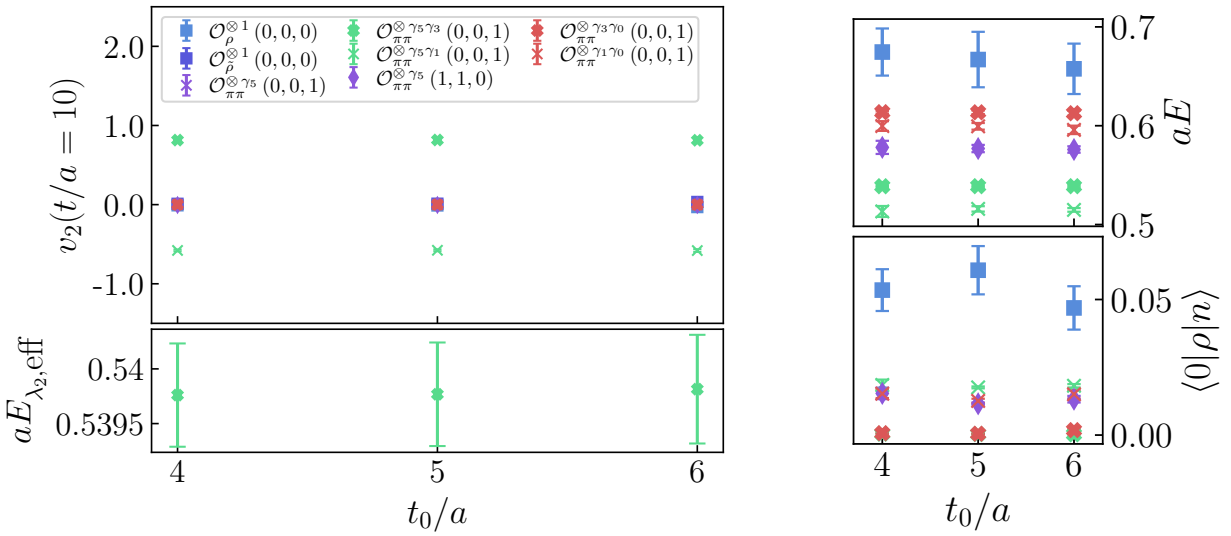

FIG. 7. Left: Normalized eigenvector for the $n = 2$ state as function of t_0 (top). The eigenvector is selected at $t'/a = 10$. The corresponding energy (bottom) is obtained by applying the effective mass formula, Eq. (3.30), to the eigenvalue and performing a correlated average over the data points $t/a > 10$. Right: Full GEVP spectrum comparison, energies (top) and amplitudes (bottom) for the same three choices of t_0. See legend of Fig. 6 for state labels. The ground state energy is omitted to improve the visibility of the rest of the spectrum, as the gap to the first excited state is large (see Fig. 6).

our preferred choice for this parameter, as it is consistent with other choices and results in the best agreement with the raw correlator in the intermediate time range (see Fig. 9).

Finally, we examine the fit stability, in Fig. 8, for a select number of states as a function of $t_{\text{min, D}}$ and $t_{\text{min, OD}}$, the lowest time included in the fit range for Eqs. (3.40) and (3.41), respectively. We find that the fit results are consistent across the values we consider, including the preferred choices from Table V, which are shown as bands. We do find for higher values of $t_{\text{min, OD}}$, namely, $9a$ that the fit to the $n = 6$ state fails to converge. Overall, all our stability checks indicate our final analysis choices result in well-determined energies and overlap amplitudes that are consistent with respect to reasonable parameter and operator basis variations.

B. Correlator reconstruction and noise reduction

With the determined energies and overlap amplitudes, the correlation function is reconstructed using the sum in Eq. (2.10) truncated to n_{max}. The corresponding reconstructed integrand of Eq. (2.3) is given in Fig. 9. Reconstructions as more states are included up to the maximum at $n_{\text{max}} = 6$ are shown. For visibility, we do not show the $n_{\text{max}} = 2$ and 5 reconstructions as they lie on top of the preceding reconstructions, due to the reduced overlap amplitudes (see bottom panel of Fig. 4). Additionally, we do not include any oscillating contributions determined from the fits. The reconstructions are compared to the raw vector-current two-point data (orange open circles), after applying improved parity averaging [69] to suppress the oscillatory behavior for better visualization.

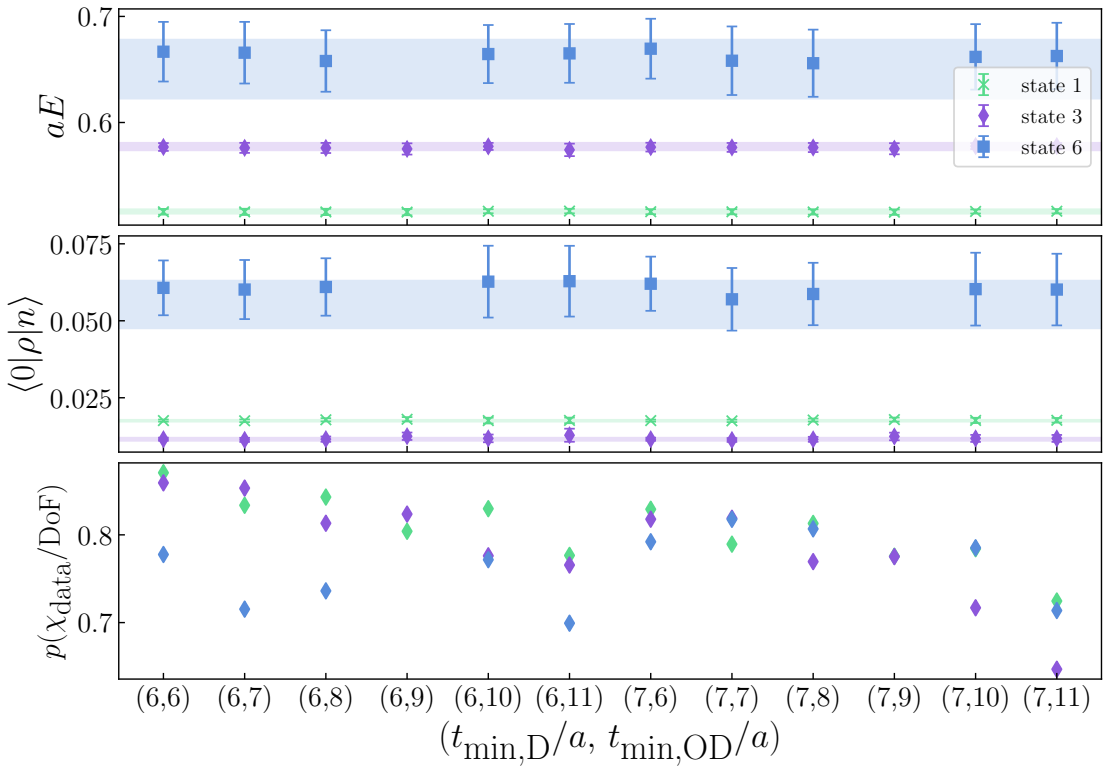

FIG. 8. Stability of fit results with respect to $t_{\text{min, D}}/a$ and $t_{\text{min, OD}}/a$ for the $n = [1, 3, 6]$ states. All fits contain $2 + 1$ exponentials and $t_{\text{max, D}}/a$ and $t_{\text{max, OD}}/a$ are fixed to 18 and 20 which corresponds to the maximum available time-slice for $t_{\text{max, D}}/a$. Bands represent the fits from the preferred values listed in Table V. Top: Ground state energy. Middle: Overlap amplitude Bottom: Quality of fit as measured by the p value, excluding the prior contribution.

For $n_{\max} = 4$, there is already good agreement between the raw data and the reconstruction at $t/a > 16$. Once the highest state is included, we have agreement as early as $t/a = 7$, but the reconstruction is actually noisier than the raw data here. In order to select a $t^\star$ at which to replace the vector-current correlator data with the reconstruction, we examine both the stability of a_μ^{ll}(conn.) with respect to $t^\star$ and also the relative error. In Fig. 10, we show the value a_μ^{ll}(conn.) as $t^\star$ is varied for a range of $n_{\max}$. We see for $n_{\max} = 6$ we have stability starting around $t^\star/a > 7$ in agreement with visual indication from Fig. 9. In the bottom panel, the relative error of these determinations is given. As mentioned, although the result stabilizes at $t^\star/a \approx 9$, precision is lost if the raw correlator data is replaced this early, as the reconstruction is noisier; hence, we select $t^\star/a = 13$.

Our results for the light-quark connected contribution to $a_\mu^{\text{HVP,LO}}$ are given in Fig. 11 for the analysis variations discussed in Sec. IV A 1. Our preferred final result is the value obtained at the reference time $t_0/a = 5$ using the full basis (blue band). We make this choice over $t_0/a = 4$ to avoid possible excited state contamination from the ρ^0 operator at early times. However, we find all variations give consistent determinations of a_μ^{ll}(conn.). The numerical value for our final result is given in Table VI, second column, for the case of using the 3473 configs of the two-pion data (first row) and also for the case of using the additional $\approx$ 6300 additional configurations for the vector current two-point function (second row). For comparison, shown in the third and fourth columns respectively and in

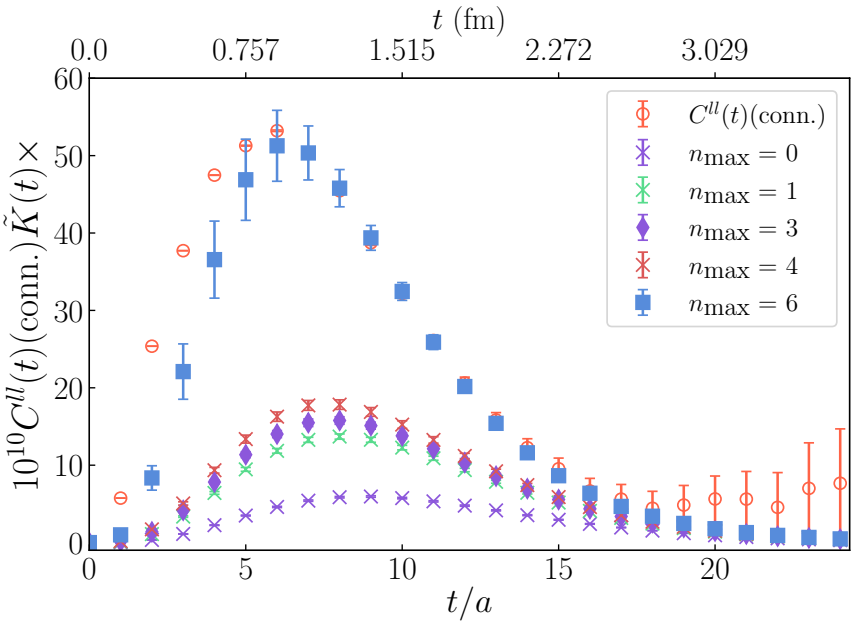

FIG. 9. Results for the taste-singlet vector-current two-point, correlation function (orange). Reconstruction of the correlation function from determined parameters for states up to $n_{\max} = [0, 6]$. In the region $t/a \in [7, 13]$, the raw correlation function results are obscured by the $n_{\max} = 6$ reconstruction.

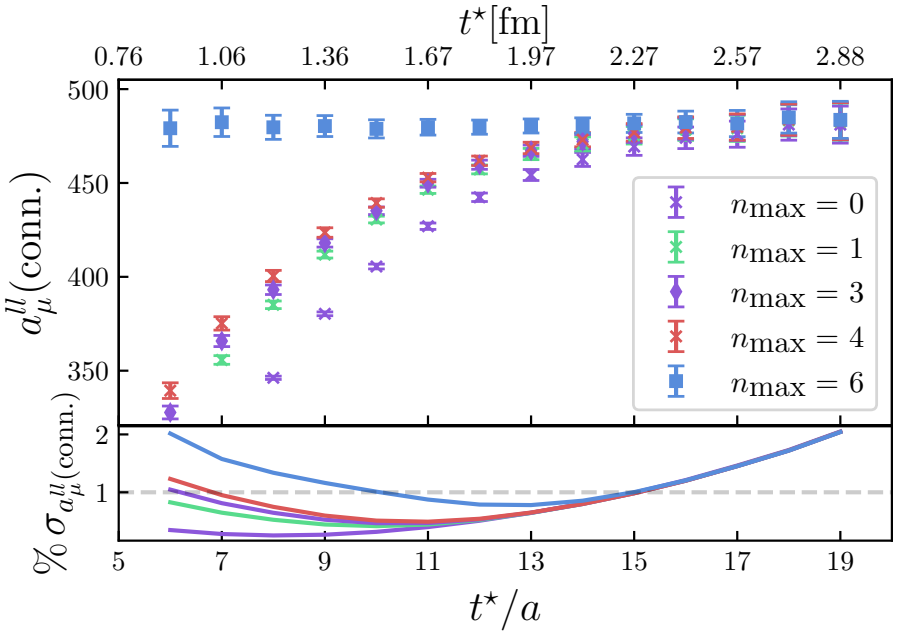

FIG. 10. Top: Results for $a_\mu^{ll}(\text{conn.})$ as $t^\star$, the point at which the correlator is replaced by the reconstruction, is varied. Bottom: relative error in the determinations of $a_\mu^{ll}(\text{conn.})$ from the top figure.

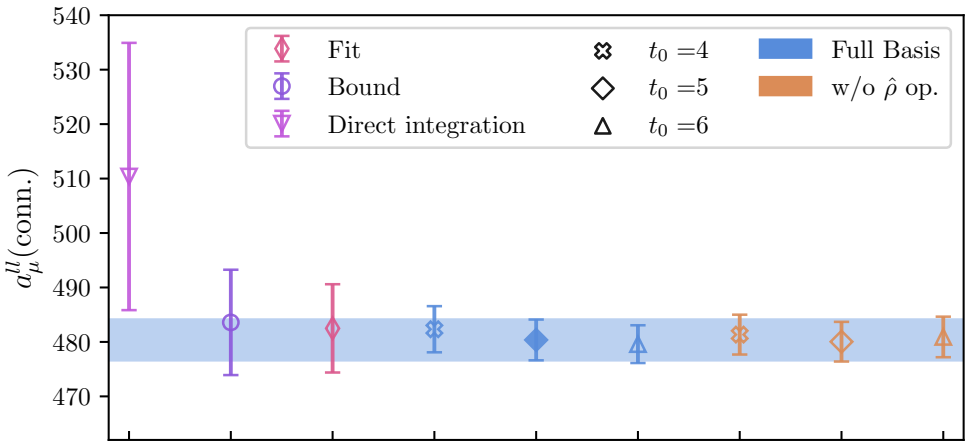

FIG. 11. Results for a_μ^{ll}(conn.) from the reconstruction strategy described in this work, using the 9600 configuration vector current dataset. We show results for the variations discussed in Sec. IV A 1, choosing different values of t_0 and also dropping the ρ^0 operator before performing the GEVP. Our final choice of a_μ^{ll}(conn.) is given by the full operator basis at $t_0/a = 5$, indicated by the blue band and filled symbol. Also included are comparisons to a_μ^{ll}(conn.) from the different noise-reduction strategies discussed in Sec. II, a_μ(fit) and a_μ(bound), as well as a_μ(direct), the result obtained by direct integration of the data with no noise-reduction applied.

TABLE VI. Numerical results for a_μ^{ll}(conn.) from the different noise-reduction strategies discussed in this work. The values for a_μ^{ll}(conn.) from the two-pion spectrum reconstruction are given in the column labelled by $a_\mu(\pi\pi$ recon.). The results from the fit and bounding methods discussed in Sec. II are given in the columns a_μ(fit) and a_μ(bound), respectively. Also included is a_μ(direct), the results obtained by direct integration of the data with no noise-reduction applied.

N_{conf}: $\left\langle J_i^l(x) J_i^l(0)\right\rangle_{\text{conn.}}$	$a_\mu(\pi\pi$ recon.)	a_μ(fit)	a_μ(bound)	a_μ(direct)
3473	477.1(5.1)	479(11)	470(17)	550(41)
9800	480.0(3.6)	482.7(9.0)	485(10)	510(25)

Fig. 11 are results from the bounding and fit methods, discussed at the end of Sec. II. Also given is the result from direct integration of the raw data, which is in mild tension with the other results, albeit with a much larger uncertainty, due to the badly behaved tail of the correlation function, visible in Fig. 9. We find all noise-reduction strategies address this issue and indeed are all consistent; however, we obtain an improvement, from the two-pion reconstruction, in statistical precision over the bounding approach of roughly a factor of 2.5.

V. SUMMARY AND OUTLOOK

The last few years have seen great progress in lattice QCD calculations of HVP observables in short- and intermediate-distance Euclidean time ranges [25, 26, 70–77]. However, the well-known signal-to-noise problem is still a limiting factor in calculations of the full HVP and the long-distance observable. In this paper, we address this issue by explicitly computing the contributions from exclusive channel two-pion states to the vector-current two-point function

at large Euclidean times. Ours is the first study of a staggered multi-hadron system which includes the full set of staggered operators. To construct the two-pion operators, we follow Refs. [47–49] to obtain the irreducible representations of the staggered group and compute the Clebsch-Gordan coefficients. The detailed information needed to construct two-pion operators, transforming under any staggered vector-current irrep, is given in the Appendices. The $I = 1$ three- and four-point correlation functions for $\rho \to \pi\pi$, $\pi\pi \to \rho$, and $\pi\pi \to \pi\pi$ are generated on the MILC collaboration's physical mass ensemble at $a \approx 0.15$ fm [46]. A GEVP analysis is used to extract the finite-volume amplitudes and energies of the interacting two-pion system. As shown in Fig. 10, the resulting spectral reconstructions of the vector-current correlation functions are obtained with greatly reduced statistical errors at large Euclidean times, while correctly reproducing the original vector-current correlation function over a range of Euclidean times down to $t \gtrsim 0.8$ fm. We find that results, for $a_\mu^{ll}(\text{conn.})$, obtained with the reconstructed correlation function are consistent with estimates using the bounding and fit methods, while improving the statistical precision by roughly a factor of 2.5 (see Table VI and Fig. 11). In summary, we show that the two-pion reconstruction offers a viable path towards lattice HVP calculations at the few permille level, also for simulations based on staggered fermions.

The next step is to extend this study to finer lattice spacings so that the statistical gains survive the continuum limit. This poses new challenges, because the smaller taste splittings at finer lattice spacings result in an increasing number of two-pion operators (see Fig. 1). In particular, for the MILC collaboration's physical mass ensemble at the next-finest lattice spacing, $a \approx 0.12$ fm, a total of eighteen two-pion operators are needed to resolve the spectrum below the ρ-meson mass, including two-pion operators made of three-link (taste vector) and four-link (taste scalar) pions, which are expected to yield noisier correlation functions. These challenges will be investigated in a follow-up study on this ensemble that is already underway.

Finally, the finite-volume amplitudes and energies of an interacting two-pion system can be related, in the Lüscher formalism [78], to the corresponding $\pi\pi$ scattering parameters in infinite-volume. Utilizing this connection for the case at hand, is, however, not straightforward, because the staggered formulation employed in this work violates unitarity, a result of the taking the fourth root of the staggered-fermion determinant to represent one quark flavor in the generation of the gauge-field ensembles. Since the unitarity violations enter as $\mathcal{O}(a^2)$ discretization errors [79], it may be possible to extend the Lüscher formalism to incorporate them. This question was investigated in Ref. [80] using partially-quenched ChPT for a non-unitary set-up involving twisted-mass fermions, while in Ref. [81] an extension of the Lüscher formalism to incorporate discretization effects was recently presented. Further investigations into this possibility are worthwhile; if successful, they could enable ab-initio studies of scattering processes and resonance physics on the large library of HISQ ensembles generated by the MILC collaboration.

ACKNOWLEDGMENTS

We thank Christine Davies, Peter Lepage, and all our collaborators in the Fermilab Lattice and MILC collaborations for useful discussions throughout the development of this project. Computations for this work were primarily carried out using resources provided by the Blue Waters sustained-petascale computing project, which is supported by NSF awards OCI-0725070 and ACI-1238993, the State of Illinois, and as of December 2019, the National Geospatial-Intelligence Agency. Blue Waters is a joint effort of the University of Illinois, Urbana-Champaign and its National Center for Supercomputing Applications. Some additional computations were also performed using Delta advanced computing and data resource which is supported by the National Science Foundation (award OAC 2005572) and the State of Illinois through allocation MCA93S002: Lattice Gauge Theory on Parallel Computers from the Advanced Cyberinfrastructure Coordination Ecosystem: Services & Support (ACCESS) program, which is supported by National Science Foundation grants #2138259, #2138286, #2138307, #2137603, and #2138296. This work was supported in part by the U.S. Department of Energy under Award No. DE-SC0015655 (A.X.K. and S.L.) and No. DE-SC0010120 (S.G.); by the Universities Research Association Visiting Scholarship awards 20-S-12 and 21-S-05 (S.L.); by the National Science Foundation under Grants PHY20-13064 and PHY23-10571. (C.D and S.L); by the Simons Foundation under their Simons Fellows in Theoretical Physics program (A.X.K.). A. El-Khadra is grateful to the Pauli Center for Theoretical Studies and the ETH Zürich for support and hospitality. This document was prepared using the resources of the Fermi National Accelerator Laboratory (Fermilab), a U.S. Department of Energy, Office of Science, HEP User Facility. Fermilab is managed by Fermi Research Alliance, LLC (FRA), acting under Contract No. DE-AC02-07CH11359.

Appendix A: Staggered quark theory primer

As this work involves multiparticle states constructed from staggered mesons, a topic not often studied in detail, this Appendix serves as a primer on the group theoretical details and notation used here. We rely primarily on the methodology introduced in Ref. [47], as it includes a natural extension for studying states at non-zero momentum. The construction of the irreducible representations of the staggered group in that work is repeated here, including the aforementioned decomposition to states at non-zero momentum. Construction of the associated operators and the connection to continuum states is also repeated, correcting some examples discussed in that work and expanding on some pertinent results relevant here.

1. Staggered lattice QCD

The staggered action has one fermion component (per color) at each site [43–45]. It can be obtained from the four-component naive action,

$$S_F[q_f, \bar{q}_f, U] = a^4 \sum_f \sum_{n\in\Lambda} \bar{q}_f(n) \left(\sum_{\mu=0}^{3} \gamma_\mu \frac{U_\mu(n) q_f(n+\hat{\mu}) - U_{-\mu}(n) q_f(n-\hat{\mu})}{2a} + m q_f(n) \right). \tag{A1}$$

through the Kawamoto-Smit transformation [45],

$$q(n) = \Omega(n) q'(n), \quad \bar{q}(n) = \bar{q}'(n)\Omega^\dagger(n), \tag{A2}$$

$$\Omega(n) \equiv (\gamma_0)^{n_0} (\gamma_1)^{n_1} (\gamma_2)^{n_2} (\gamma_3)^{n_3} . \tag{A3}$$

which diagonalizes the action as

$$S_F \left[q'_f, \bar{q}'_f, U\right] = a^4 \sum_f \sum_{n\in\Lambda} \bar{q}'_f(n) \left(\sum_{\mu=0}^{3} \eta_\mu(n) \frac{U_\mu(n) q'_f(n+\hat{\mu}) - U^\dagger_\mu(n-\hat{\mu}) q'_f(n-\hat{\mu})}{2a} + m q'_f(n) \right), \tag{A4}$$

with

$$\eta_\mu(n) \equiv \Omega^\dagger(n)\gamma_\mu\Omega(n \pm \hat{\mu}) = (-1)^{\sum_{\rho<\mu} n_\rho}. \tag{A5}$$

The spacetime directions are ordered (t, x, y, x) as in the MILC code, instead of the (x, y, z, t) order in Ref. [47]. Three of the four identical spin degrees of freedom are dropped to obtain the staggered quark action [44, 45]

$$S_F \left[\chi_f, \bar{\chi}_f, U\right] = a^4 \sum_f \sum_{n\in\Lambda} \bar{\chi}_f(n) \left(\sum_{\mu=0}^{3} \eta_\mu(n) \frac{U_\mu(n) \chi_f(n+\hat{\mu}) - U^\dagger_\mu(n-\hat{\mu}) \chi_f(n-\hat{\mu})}{2a} + m \chi_f(n) \right), \tag{A6}$$

where the χ field has one fermion degree of freedom per site. The reason for the reduction is that the naive action leads to 16 Dirac fermions in the continuum limit. Now only four 'tastes' survive.

2. Staggered symmetries and group structure

This work employs a lattice with $N_t = 48$ sites in the temporal direction and $N_s = 32$ sites in the spatial directions, and $N_t > N_s$ holds on the other 2+1+1-flavor HISQ ensembles [*ref*] that will be used in the future. Thus, symmetry between (Euclidean) time and space is absent [7], which is fine, as the objective here is the transformation properties of eigenstates of the transfer matrix and the operators that create them. Here, we show how the symmetries of staggered fermions combine to form the symmetry group of the transfer matrix.

a. Symmetries

The Kawamoto-Smit transformation in Eq. (A2) depends on n_μ, and hence modifies spin structure, differently at different spacetime points. Because of this, the original symmetries from the naive action, now have mixed spacetime-spin dependence when applied to $q'(n)$. Translations acting on the fields in the diagonalized action, for example, become

$$q'(n) \to \zeta_\mu(n)\gamma_\mu q'(n - \hat{\mu}), \tag{A7}$$

[7] The effect of this symmetry breaking is not detectable in the analysis described here. We find, for example, that the 3-fold and 1-fold multiplet of spatial and temporal 'one-link' pions are degenerate.

where

$$\zeta_\mu(n) \equiv \Omega^{-1}(n)\Omega(n \pm \hat{\mu})\gamma_\mu = (-1)^{\Sigma_{\sigma>\mu} n_\sigma}. \tag{A8}$$

It is preferable to have symmetry transformations which are also diagonal in the spinor index, as these can be associated with the one-component staggered action in Eq. (A6) and hence, can be used to classify the irreps (states) of the theory. The spin-diagonal set of transformations are obtained by combining the original symmetry transformations of the QCD action, after discretization, with the doubling transformations of the naive action,

$$q(n) \to e^{\omega^A B^A(x)} q(n), \bar{q}(n) \to \bar{q}(n) e^{-\omega^A B^A(x)}. \tag{A9}$$

The generating set $B^A(x)$ are anti-Hermitian and given by

$$B_\mu(n) = \gamma_\mu \gamma_5 (-1)^{n_\mu}, B_5(n) = i\gamma_5 \varepsilon(n), B_\mu(n) B_5(n), B_\mu(n) B_\nu(n) (\mu < \nu), \tag{A10}$$

where

$$\varepsilon(n) = (-1)^{n_0+n_1+n_2+n_3}. \tag{A11}$$

The resultant spin-diagonal symmetry operations are then

1. Translations $x \to x - a\hat{\mu}$ or $n \to n - \hat{\mu}$:
   Choosing $B_\mu(n) B_5(n)$ results in a spin-diagonal operator, leading to the staggered *shift*

$$S_\mu : \begin{cases} \chi(n) \to \zeta_\mu(n) \chi(n - \hat{\mu}), \\ \overline{\chi}(n) \to \zeta_\mu(n) \overline{\chi}\,(n - \hat{\mu}). \end{cases} \tag{A12}$$

2. Rotations by $\pi/2$ in the $\mu\nu$ plane, $R_{\mu\nu}$:
   Choosing $B_\mu(n) B_\nu(n)$ leads to the transformation rule for the staggered field

$$R_{\mu\nu} : \begin{cases} \chi(n) \to S_{R_{\mu\nu}}\left(R^{-1}n\right) \chi\left(R^{-1}n\right) \\ \overline{\chi}(n) \to S_{R_{\mu\nu}}\left(R^{-1}n\right) \overline{\chi}\left(R^{-1}n\right) \end{cases}, \tag{A13}$$

   where

$$\begin{aligned} S_{R_{\mu\nu}}\left(R^{-1}n\right) = \frac{1}{2} \big[& 1 + \eta_\mu(R_{\mu\nu}^{-1}n)\eta_\nu(R_{\mu\nu}^{-1}n)\zeta_\mu(R_{\mu\nu}^{-1}n)\zeta_\nu(R_{\mu\nu}^{-1}n) \\ & - \zeta_\mu(R_{\mu\nu}^{-1}n)\zeta_\nu(R_{\mu\nu}^{-1}n) + \eta_\mu(R_{\mu\nu}^{-1}n)\eta_\nu(R_{\mu\nu}^{-1}n) \big], \end{aligned} \tag{A14}$$

   where

$$\eta_\mu(n) \equiv (-1)^{\Sigma_{\sigma<\mu} n_\sigma}. \tag{A15}$$

   Upon applying $R_{\mu\nu}$ four times, the product of the $S_{R_{\mu\nu}}$ factors yields -1, as it should for a fermion.

3. Spatial inversion $I_S : n_0 \to n_0, n_i \to -n_i$:
Choosing $B_0 B_5$ leads to,

$$I_S : \begin{cases} \chi(n) \to (-1)^{n_1+n_2+n_3} \chi\left(I_S n\right) \\ \overline{\chi}(n) \to (-1)^{n_1+n_2+n_3} \overline{\chi}\left(I_S n\right) \end{cases} , \tag{A16}$$

so staggered fermions at odd and even spatial sites have opposite intrinsic parity. For inversion of a single axis, $I_\mu : \chi(n) \to (-1)^{n_\mu} \chi(I_\mu n)$ and similarly for $\overline{\chi}$. As discussed below, $I_S = I_1 I_2 I_3$ is not quite the parity operator of the continuum limit.

4. Charge conjugation:
Choosing $B_2(n) B_5(n) = i\gamma_2 (-1)^{n_2} \varepsilon(n)$ gives the transformation rule for staggered charged conjugation

$$C_0 : \begin{cases} \chi(n) \to \varepsilon(n) \overline{\chi}(n) \\ \overline{\chi}(n) \to -\varepsilon(n) \chi(n) \end{cases} . \tag{A17}$$

As discussed below, C_0 is not quite continuum-limit charge conjugation, hence the subscript.

5. Chiral symmetry:
The global chiral flavor symmetries also have spinor structure. In going to the reduced action, a remnant of this symmetry still exists as

$$\chi' = \mathrm{e}^{\mathrm{i}\alpha\varepsilon(n) T_i} \chi, \qquad \bar{\chi}' = \bar{\chi} \mathrm{e}^{\mathrm{i}\alpha\varepsilon(n) T_i}, \tag{A18}$$

$$\chi' = \mathrm{e}^{\mathrm{i}\alpha\varepsilon(n)} \chi, \qquad \bar{\chi}' = \bar{\chi} \mathrm{e}^{\mathrm{i}\alpha\varepsilon(n)}, \tag{A19}$$

where T_i is a flavor-symmetry generator, and Eq. (A19) show the flavor singlet case, which is *not*, however, a taste singlet.

b. Group structure

The symmetry group of the transfer matrix is generated by $\{R_{ij}, S_\mu, I_S, C_0\}$.[8] It is necessary to know their commutation relations. As always, the rotations $R_{\mu\nu}$, Eq. (A13), and axis inversions, I_μ, satisfy

$$R_{\mu\nu} I_\mu R_{\mu\nu}^{-1} = I_\nu = R_{\nu\mu} I_\mu R_{\nu\mu}^{-1}, \tag{A20}$$

$$R_{\mu\nu} I_\rho R_{\mu\nu}^{-1} = I_\rho, \rho \neq \mu, \nu. \tag{A21}$$

The shifts anti-commute,

$$S_\mu S_\nu S_\mu^{-1} = -S_\nu, \nu \neq \mu. \tag{A22}$$

With N_s sites (N_s must be even) in the spatial directions, repeating a spatial shift N_s times yields $S_i^{N_s} = \pm 1$, with the upper (lower) sign for (anti)periodic boundary conditions. Similarly, $S_0^{N_t} = \pm 1$. The shifts and rotation-reflections satisfy

$$R_{\mu\nu}^{-1} S_\mu R_{\mu\nu} = S_\nu, \tag{A23}$$

[8] The temporal-spatial rotations R_{0j} are not symmetries.

$$R_{\mu\nu}^{-1} S_\nu R_{\mu\nu} = -S_\mu^{-1}, \tag{A24}$$
$$R_{\mu\nu}^{-1} S_\rho R_{\mu\nu} = S_\rho, \rho \neq \mu, \nu \tag{A25}$$
$$I_S S_i I_S^{-1} = -S_i^{-1}, i = 1, 2, 3, \tag{A26}$$
$$I_S S_0 I_S^{-1} = S_0. \tag{A27}$$

Charge conjugation commutes with all reflections and rotations and anti-commutes with the shifts,

$$C_0 S_\mu = -S_\mu C_0. \tag{A28}$$

The flavor and color symmetries commute with all geometric symmetries and charge conjugation.

The transfer matrix for staggered fermions, Eq. (A6), is a Hilbert-space operator acting on physical states, evolving them two temporal spacings forward [44]. It is thus the Hilbert-space operator corresponding to

$$T_0 = S_0^2. \tag{A29}$$

T_0, of course, commutes with S_0. It is convenient to take the formal square root

$$\Xi_0 = T_0^{-1/2} S_0, \tag{A30}$$

i.e., if the eigenvalue of $\hat{T}_0$ is e^{-2E}, then $T^{-1/2} = \mathrm{e}^E$. In the same vein, it is convenient to introduce the same construction for the spatial directions, $T_i = S_i^2$ and

$$\Xi_i = T_i^{-1/2} S_i, \tag{A31}$$

where $T_i^{-1/2}$ is again defined via the eigenvalue of T_i. It is customary to call the Ξ_μ taste operators, to distinguish them from the shifts. They satisfy the same commutation rules as the S_μ, Eqs. (A23)–(A27). In particular, the Ξ_μ generate the Clifford group Γ_4, or incorporating charge conjugation, Eq. (A28), $\Gamma_{4,1}$ [47].

Thus, ignoring flavor and color, the symmetry group of the staggered transfer matrix is

$$\begin{aligned} G_{T_0} &= \{T_i\} \rtimes [\{\Xi_\mu, C_0\} \rtimes \{R_{ij}, I_S\}] \\ &= Z_{N_s/2}^3 \rtimes (\Gamma_{4,1} \rtimes O_\mathrm{h}), \end{aligned} \tag{A32}$$

with the octahedral group O_h consisting of the rotation-reflection symmetries of the cube.

3. Irreducible representations of the staggered group

Classifying the irreps of Eq. (A32) involves applying Wigner's method [82] for semi-direct products, $G = N \rtimes H$. Wigner's method needs to applied twice, first with the normal subgroup given by $N = Z_{N_s/2}^3$ and $H = \Gamma_{4,1} \rtimes O_\mathrm{h}$, and then with $N = \Gamma_{4,1}$ and $H = O_\mathrm{h}$. Only the bosonic representations are relevant for this work, as meson states appear exclusively. Considering just the bosonic representations of $\Gamma_{4,1}$ simplifies the construction, as the group homomorphism $\Gamma_{4,1} \to Z_2^5$ can be exploited in this case.

When N is Abelian, Wigner's method proceeds as follows [55]:

1. Determine all (one-dimensional) irreps 'σ' of the normal Abelian subgroup N.

2. For each irrep σ, determine the subgroup $H(\sigma) \subseteq H$ of elements h satisfying the character equation

$$\chi_N^{(\sigma)}(hnh^{-1}) = \chi_N^{(\sigma)}(n), \forall n \in N, \tag{A33}$$

where $\chi_N^{(\sigma)}$ denotes the character of σ in the normal subgroup N. The $H(\sigma)$ are the so-called little groups.

3. Classify the irreps, σ, into orbits(also called 'stars' [49]), which is achieved by breaking H into right cosets under the little group $H(\sigma)$,

$$H = H(\sigma)h_1 + H(\sigma)h_2 + \ldots + H(\sigma)h_{|H|/|H(\sigma)|}, \tag{A34}$$

where $h_1 = E$ (identity element) and $h_i \notin H(\sigma)h_j$ for all $i \neq j$. From Eq. (A34) we can then choose a set of coset representatives,

$$\{h_1, h_2, \ldots, h_{|H|/|H(\sigma)|}\}. \tag{A35}$$

The orbit is then the list of irreps, each with the same little group,

$$\{h_1(\sigma) = \sigma, h_2(\sigma), \ldots, h_{|H|/|H(\sigma)|}(\sigma)\}, \tag{A36}$$

determined from

$$\chi_N^{(h_i(\sigma))}(n) = \chi_N^{(\sigma)}(h_i n h_i^{-1}), \forall n \in N. \tag{A37}$$

4. Determine the irreps ρ of the little groups $H(\sigma)$.

5. Form irreps of the semi-direct groups $G(\sigma) = N \rtimes H(\sigma)$ for a single representative σ in each orbit as

$$D_{G(\sigma)}^{(\sigma,\rho)}(nh) = \chi_N^{(\sigma)}(n) D_{H(\sigma)}^{(\rho)}(h). \tag{A38}$$

6. Induce an irrep for the full group G through the formula

$$D_G^{(\gamma)}(g)_{it,jr} = \begin{cases} \chi_N^{(h_i(\sigma))}(n) D_{H(\sigma)}^{(\rho)}(h_i h h_j^{-1})_{tr}, & \text{if } h_i h h_j^{-1} \in H(\sigma) \\ 0, & \text{if } h_i h h_j^{-1} \notin H(\sigma) \end{cases}. \tag{A39}$$

A complete set of irreps is obtained by preforming the above step for each orbit.

As mentioned, the approach described above needs to applied twice for the nested semi-direct products appearing in Eq. (A32). In the first case, where the normal subgroup is given by $N = Z_{N_s/2}^3$, and $H = \Gamma_{4,1} \rtimes O_{\rm h}$, the one dimensional irreps of $Z_{N_s/2}^3$ are given by

$$T_i|\vec{p}\rangle = \exp\left(i2p_i\right)|\vec{p}\rangle, \quad p_i = \frac{2\pi}{aN_s}\ell_i, \tag{A40}$$

with ℓ_i as specified in Eq. (3.6). In the bosonic case, as mentioned above, the irreps of $\Gamma_{4,1}$ can be obtained by the homomorphism to the Abelian group Z_2^5 and are

$$D(\Xi_\mu) = e^{i(\pi_\xi)_\mu}, \quad \pi_\xi \equiv (\xi_0, \xi_1, \xi_2, \xi_3), \quad \xi_\mu = 0, \pi, \tag{A41}$$

TABLE VII. Momentum orbits under the staggered rotation group. First column: The list of the momentum orbits (with $2\pi/aN_s$ factored out) under the staggered rotation group, given by a representative element and the dimension. Second column: The corresponding little group given by its group generators and the corresponding group structure and order.

Orbit representative	Size	Little group generators and structure	Order
$(0,0,0)$	1	$\{\Xi_\mu, R_{ij}, I_S\} \cong \Gamma_{4,1} \rtimes O_\mathrm{h}$	48
$(0,0,\ell)$	6	$\{\Xi_\mu, R_{12}, R_{13}^2 I_S\} \cong \Gamma_{4,1} \rtimes \mathrm{D}_4$	8
$(\ell,\ell,0)$	12	$\{\Xi_\mu, R_{13}^2 R_{21}, R_{12}^2 I_S\} \cong \Gamma_{4,1} \rtimes \mathrm{C}_{2\mathrm{v}}$	4
(ℓ,ℓ,ℓ)	8	$\{\Xi_\mu, R_{13}^2 R_{12} I_S, R_{12}^2 R_{13} I_S\} \cong \Gamma_{4,1} \rtimes \mathrm{D}_3$	6
(ℓ,ℓ,m)	24	$\{\Xi_\mu, R_{12}^2 I_S\} \cong \Gamma_{4,1} \rtimes Z_2$	2
$(0,\ell,m)$	24	$\{\Xi_\mu, R_{23}^2 I_S\} \cong \Gamma_{4,1} \rtimes Z_2$	2
(ℓ,m,n)	48	$\{\Xi_\mu\} \cong \Gamma_{4,1} \rtimes \{E\}$	1

$$D(C_0) = e^{i\xi_C}, \quad \xi_C = 0, \pi. \tag{A42}$$

The elements of $\Gamma_{4,1}$ leave the momentum invariant, hence orbits consist of the list of momenta obtained through application of elements of O_h to the vector p_i. The corresponding little groups are the subgroups of $\Gamma_{4,1} \rtimes O_\mathrm{h}$ which leave the orbit representatives invariant. The complete set of orbits and little groups are listed in Table VII.

To classify irreps of these little groups, Wigner's method must be employed again where the normal subgroup is now $N = \Gamma_{4,1}$ and H are the rotation subgroups O_h, D_4, $\mathrm{C}_{2\mathrm{v}}$, D_3, Z_2. From Eqs. (A41) and (A42) there are $2^5 = 32$ one-dimensional bosonic irreps of $\Gamma_{4,1}$. By comparison of Eq. (A40) to Eq. (A41), the spatial part of the taste irrep vector will behave similarly to the momentum orbits under the momentum little groups in Table VII. More specifically, labelling the irreps of $\Gamma_{4,1}$ by

$$[\pi_\xi, \xi_C] = [(\xi_0, \xi_1, \xi_2, \xi_3), \xi_C], \tag{A43}$$

the little group $H([\pi_\xi, \xi_C])$ is the group of all elements h of H such that $h : [(\xi_0, \xi_1, \xi_2, \xi_3), \xi_C] \to [(\xi_0, \xi_1, \xi_2, \xi_3), \xi_C]$. And the orbits are then the unique set $\{[\pi_\xi, \xi_C]\}$ obtained from $h : [(\xi_0, \xi_1, \xi_2, \xi_3), \xi_C]$ $\forall\ h \in H$. As ξ_0 commutes with everything (there are no R_{0i}), $\xi_0 = 0$ and $\xi_0 = \pi$ always correspond to different orbits. Similarly, for $\xi_C = 0$ and $\xi_C = \pi$. Because of the mod2π associated with π_ξ any element hI_S in H will be in the little group $H([\pi_\xi, \xi_C])$ if h is. The complete list of bosonic taste orbits and taste little groups are given in the Table VIII. The character tables defining these bosonic irreps[9] are given in Appendix B 1.

Staggered irreps are uniquely labelled by a momentum orbit representative, a taste-charge conjugation orbit representative and a rotation little group irrep. As an example, a zero momentum, taste-singlet, rotation-vector irrep, with negative staggered charge conjugation and negative staggered parity is denoted by

$$(0,0,0) \rtimes [(0,0,0,0), \pi] \rtimes T_0^-. \tag{A44}$$

[9] These (non-projective) irreps are labelled bosonic as they result in staggered bosonic irreps once combined with the Abelian irreps of $\Gamma_{4,1}$. Similarly, the non-Abelian irreps of $\Gamma_{4,1}$ combine with the projective irreps of the rotation little groups to give fermionic irreps.

TABLE VIII. Taste orbits, little groups and irreps for each momentum orbit under the staggered group. The first column is the taste orbit, indicated by a representative element. The second column lists the orbit size. The third and fourth columns show the taste little groups (giving their generating elements and conventional name) and order. The final column shows the irreps of these groups. Irreps labelled A are 1D, E are 2D and T are 3D. Zero momentum irreps are also labelled by the sign under spatial inversion $\pm$. The character tables defining the irreps of the little groups are given in Appendix B 1. Also given is the total number of staggered group irreps resulting from these orbits and little group irreps and their dimensions.

Orbit representative (momentum) [(taste), C_0]	Orbit size	Little group	Order	Little-group irreps
		total # irreps (dimensions)		
$(0,0,0)$		160 irreps (32 1D, 16 2D, 96 3D and 16 6D)		
$[(\xi_0,0,0,0),\xi_C]$ $[(\xi_0,\pi,\pi,\pi),\xi_C]$	1	$\{R_{ij}, I_S\} \cong O_\mathrm{h}$	48	$A_0^\pm$, $A_1^\pm$, $E_0^\pm$, $T_0^\pm$, $T_1^\pm$
$[(\xi_0,\pi,0,0),\xi_C]$ $[(\xi_0,0,\pi,\pi),\xi_C]$	3	$\{R_{12}, R_{13}^2, I_S\} \cong \mathrm{D}_{4\mathrm{h}}$	16	$A_0^\pm$, $A_1^\pm$, $A_2^\pm$, $A_3^\pm$, $E_0^\pm$
$(0,0,\ell)$		112 irreps (64 1D and 48 2D)		
$[(\xi_0,0,0,\xi_3),\xi_C]$ $[(\xi_0,\pi,\pi,\xi_3),\xi_C]$	1	$\{R_{12}, R_{13}^2 I_S\} \cong \mathrm{D}_4$	8	A_0, A_1, A_2, A_3, E_0
$[(\xi_0,0,\pi,\xi_3),\xi_C]$	2	$\{R_{12}^2, R_{13}^2 I_S\} \cong \mathrm{C}_{2\mathrm{v}}$	4	A_0, A_1, A_2, A_3
$(\ell,\ell,0)$		80 irreps (64 1D and 16 2D)		
$[(\xi_0,0,0,\xi_3),\xi_C]$ $[(\xi_0,\pi,\pi,\xi_3),\xi_C]$	1	$\{R_{13}^2 R_{21}, R_{12}^2 I_S\} \cong \mathrm{C}_{2\mathrm{v}}$	4	A_0, A_1, A_2, A_3
$[(\xi_0,0,\pi,\xi_3),\xi_C]$	2	$\{R_{12} I_S\} \cong Z_2$	2	A_0, A_1
(ℓ,ℓ,ℓ)		40 irreps (16 1D, 8 2D and 16 3D)		
$[(\xi_0,0,0,0),\xi_C]$ $[(\xi_0,\pi,\pi,\pi),\xi_C]$	1	$\{R_{13}^2 R_{12} I_S, R_{12}^2 R_{13} I_S\} \cong \mathrm{D}_3$	6	A_0, A_1, E_0
$[(\xi_0,\pi,0,0),\xi_C]$ $[(\xi_0,0,\pi,\pi),\xi_C]$	3	$\{R_{13}^2 R_{12} I_S\} \cong Z_2$	2	A_0, A_1
(ℓ,ℓ,m)		40 irreps (32 1D and 8 2D)		
$[(\xi_0,0,0,\xi_3),\xi_C]$ $[(\xi_0,\pi,\pi,\xi_3),\xi_C]$	1	$\{R_{12}^2 I_S\} \cong Z_2$	2	A_0, A_1
$[(\xi_0,0,\pi,\xi_3),\xi_C]$	2	$\{E\}$	1	A_0
$(0,\ell,m)$		64 irreps (64 1D)		
$[(\xi_0,\xi_1,\xi_2,\xi_3),\xi_C]$	1	$\{R_{23}^2 I_S\} \cong Z_2$	2	A_0, A_1
(ℓ,m,n)		32 irreps (32 1D)		
$[(\xi_0,\xi_1,\xi_2,\xi_3),\xi_C]$	1	$\{E\}$	1	A_0

In Appendix A 4, one sees this is excited by a one-link staggered spatial vector current operator. This is three-dimensional, which can be seen from the product of the dimensions of the two orbits and the rotation irrep dimension.

$$\begin{aligned}&\text{Momentum orbit: } \{(0,0,0)\} - 1\text{D},\\ &\text{Taste orbit: } \{(0,0,0,0)\} - 1\text{D},\\ &O_\text{h} \text{ irrep: } T_0^- \ - 3\text{D},\end{aligned}$$

giving a total irrep dimension of $1 \times 1 \times 3$. As another example, a second irrep which also has the quantum numbers of the vector current operator is the zero momentum, taste-vector rotation-singlet irrep with positive charge conjugation and parity

$$(0,0,0) \rtimes [(\pi,0,\pi,\pi),0] \rtimes A_0^+, \tag{A45}$$

with the dimension breakdown

$$\begin{aligned}&\text{Momentum orbit: } \{(0,0,0)\} - 1\text{D},\\ &\text{Taste orbit: } \{(\pi,0,\pi,\pi),(\pi,\pi,0,\pi),(\pi,\pi,\pi,0)\} - 3\text{D},\\ &\text{D}_\text{4h} \text{ irrep: } A_0^+ - 1\text{D}.\end{aligned}$$

This also has the total dimension of 3, but it is now coming from the taste orbit rather than the rotation irrep. As a final example, a taste-vector, rotation-singlet irrep with one component of momentum, and negative charge conjugation,[10]

$$(0,0,\ell) \rtimes [(\pi,0,\pi,\pi),\pi] \rtimes A_2, \tag{A46}$$

with the following breakdown,

$$\begin{aligned}&\text{Momentum orbit: } \{(0,0,\ell) + 5 \text{ perms.}\} - 6\text{D},\\ &\text{Taste orbit: } \{(\pi,0,\pi,\pi),(\pi,\pi,0,\pi)\} - 2\text{D},\\ &\text{C}_\text{2v} \text{ irrep: } A_2 \ \ - 1\text{D},\end{aligned} \tag{A47}$$

giving a total dimension of 12. This irrep corresponds to a pseudo-scalar meson in flight in the continuum, i.e., a pion if one considers light-quark flavors.

In this work, we employ operators which excite the taste-singlet vector meson Eq. (A44), for the reasons discussed in Sec. III A. For each continuum bosonic state, there are $4 \times 4 = 16$ staggered states which have all the same quantum numbers except for the taste. The pseudoscalar irrep, Eq. (A46), is one of the multiple tastes of pion we study here, the full set is given in Appendix C 2. Depending on the taste and the momentum direction, these states can have degenerate or non-degenerate energies. In this work, the multi-particle states are built from single-particle states with momentum. Hence, understanding the relationship between staggered states at rest and states in flight is vital.

[10] Parity is not a good quantum number for states in flight.

a. Non-zero momentum decomposition

In order to decompose a staggered irrep at zero momentum to irrep(s) at non-zero momentum, one needs to

- Decompose the zero momentum taste orbit into the non-zero momentum taste orbit(s).
- Restrict the zero momentum little group irrep to the corresponding non-zero momentum taste little group(s) and determine what irrep(s) are contained in the (now) reducible representation.

To illustrate this, consider giving momentum in the z-direction to the following zero momentum state

$$(0,0,0) \rtimes [(\pi,\pi,0,0),\pi] \rtimes A_1^+ - 3\mathrm{D}; \quad O_\mathrm{h}\left(\vec{p},[\pi_\xi,\xi_C]\right) = \mathrm{D}_{4h}. \tag{A48}$$

The $\{(0,0,\ell)\}$ momentum little group only mixes ξ_1,ξ_2 in orbits, so ξ_3 becomes independent. Hence, the $(0,0,0)$ momentum taste-orbit $\{(\pi,0,0,\pi),(\pi,0,\pi,0),(\pi,\pi,0,0)\}$ splits into two parts. A two-dimensional orbit $\{(\pi,0,\pi,0),(\pi,\pi,0,0)\}$ with little group $O_\mathrm{h}\left(\vec{p},[\pi_\xi,\xi_C]\right) \cong \mathrm{C}_{2\mathrm{v}}$ and a one-dimensional orbit $\{(\pi,0,0,\pi)\}$ with little group $O_\mathrm{h}\left(\vec{p},[\pi_\xi,\xi_C]\right) \cong \mathrm{D}_4$. One then restricts the original little group, $\mathrm{D}_{4\mathrm{h}}$, to the two new little groups giving the following irrep decomposition

$$A_2^+\big|_{\mathrm{D}_{4\mathrm{h}}\to\mathrm{C}_{2\mathrm{v}}} = A_3, \tag{A49}$$

$$A_2^+\big|_{\mathrm{D}_{4\mathrm{h}}\to\mathrm{D}_4} = A_1. \tag{A50}$$

This restriction is performed by considering the characters of the conjugacy classes which remain after removing the elements not contained in the respective subgroups. The standard character decomposition [55] is employed to obtain the irreps of the subgroups. In both cases here, there is only one irrep contained, A_3 and A_1 respectively. Hence, there are now two $(0,0,\ell)$ momentum irreps from the original single zero-momentum irrep

$$(0,0,\ell) \rtimes [(\pi,\pi,0,0),\pi] \rtimes A_3 - 6\times 2\mathrm{D}, \tag{A51}$$

$$(0,0,\ell) \rtimes [(\pi,0,0,\pi),\pi] \rtimes A_1 - 6\times 1\mathrm{D}. \tag{A52}$$

This splitting of the taste-orbit into separate irreps is observed in the pion spectrum computed in Sec. III F.

4. Staggered operators

Following the form of the staggered action in the hypercubic representation [83, 84], one formally writes a staggered quark operator in the hypercubic representation (spin-taste basis) as

$$\mathcal{O}^{\Gamma_S\otimes\Gamma_T}(h) = \bar{q}(h)\Gamma_S\otimes\Gamma_T q(h). \tag{A53}$$

This operator has a spin quantum number from Γ_S and a taste quantum number from Γ_T.[11] Numerical simulations, however, are typically performed in the representation of Eq. (A6).

[11] The gauge links are left out for simplicity.

Recasting the operator in this form results in 'phase-shift' operators,

$$\mathcal{O}^{\varphi}_{(\delta)}(\vec{p},t) = \sum_{\vec{n}} e^{-ia\vec{p}\cdot\vec{n}}\bar{\chi}(n)\chi(n+\delta)\varphi(n). \tag{A54}$$

where the operator has now also been given a momentum p. The unbarred field is shifted by a spatial offset δ and there is an associated spacetime dependent staggered phase $\varphi(n)$. The relationship between these two representations is given by

$$\varphi(n) = \frac{1}{4}\mathrm{tr}\left(\Gamma_T^{\dagger}\Omega(n)^{\dagger}\Gamma_S\Omega(n+t+s)\right), \tag{A55}$$

$$\delta = t + s \bmod 2, \tag{A56}$$

where $\Omega(n)$ is defined in Eq. (A3) and s and t are four vectors which specify the spin and taste gamma structure. In this work, we use the $\Gamma_S \otimes \Gamma_T$ labelling to denote the operators, but the phase-shift form is used in the computation. Only symmetric-non-time-shift operators are considered,

$$\mathcal{O}^{\varphi}_{(\pm\delta)}(\vec{p},t) = \frac{1}{N_{\mathrm{sym}}}\sum_{\pm\delta_i}\mathcal{O}^{\varphi}_{(\delta)}(\vec{p},t). \tag{A57}$$

With an average over forward and backward directions for each component of δ performed. Symmetrizing in this way guarantees the operators have well-defined parity and, for flavor singlets, charge conjugation.

The phase-shift operators can be straight-forwardly related to the rows of the irreps from above by acting on them with the staggered symmetry transformations and reading off the quantum numbers:

$$\Xi_i : \mathcal{O}^{\varphi}_{(\pm\delta)}(\vec{p}) \to \zeta_i(\delta)\varphi(\hat{\imath})\mathcal{O}^{\varphi}_{(\pm\delta)}(\vec{p}), \tag{A58}$$

$$I_S : \mathcal{O}^{\varphi}_{(\pm\delta)}(\vec{p}) \to (-1)^{\sum_i \delta_i}\mathcal{O}^{\varphi}_{(\mp\delta)}(-\vec{p}), \tag{A59}$$

$$R_{ij} : \mathcal{O}^{\varphi}_{(\pm\delta)}(\vec{p}) \to \mathcal{O}^{\varphi'}_{(\pm\delta')}(\vec{p}'), \tag{A60}$$

$$C_0 : \mathcal{O}^{\varphi}_{(\pm\delta)}(\vec{p}) \to e^{i\vec{p}\cdot\vec{\delta}}(-1)^{\sum_i \delta_i}\varphi(\delta)\mathcal{O}^{\varphi}_{(\mp\delta)}(\vec{p}), \tag{A61}$$

where φ' $(\vec{p}')$ is obtained from φ $(\vec{p})$ via the given rotation. The momentum is specified through Eq. (A54). As the sum in Eq. (A54) does not include t, the operator is local in time and hence can excite irreps with any energy. Similarly, this results in ξ_0 not being fixed, hence the operators in Eq. (A54) excite states with $\xi_0 = 0$ and $\xi_0 = \pi$—without a full construction of the transfer matrix, operators of definite ξ_0 cannot be constructed. This is the source of the well known issue with local-time staggered operators, whereby states with both positive and negative continuum parity are excited, resulting in temporal oscillations in staggered correlation functions. Under the action of rotation group, Eq. (A60), the transformed operators $\{(\varphi_i', \delta_i')\}$ form a basis of the taste little group. Constructing the representation from this basis then allows one to determine the rotation irrep.

Operators corresponding to the examples considered in Eqs. (A44)–(A46) are given by

- taste singlet, spin vector, $(0,0,0) \rtimes [(0,0,0,0),\pi] \rtimes T_0^-$

$$\mathcal{O}^{\gamma_i\otimes 1}(\vec{p}=0) \ : \ \varphi(n) = \eta_i(n), \delta_j = \delta_{j,i}. \tag{A62}$$

- taste vector, spin vector, $(0,0,0) \rtimes [(\pi,0,\pi,\pi),0] \rtimes A_0^+$

$$\mathcal{O}^{\gamma_i \otimes \gamma_i}(\vec{p}=0) \ : \ \varphi(n) = (-1)^{\sum_{\rho \neq i} n_\rho}, \delta = (0,0,0,0). \tag{A63}$$

- taste vector, spin pseudo-scalar, $(0,0,\ell) \rtimes [(\pi,0,\pi,\pi),\pi] \rtimes A_2$

$$\mathcal{O}^{\gamma_5\gamma_0 \otimes \gamma_i}(\vec{p}=[0,0,l]) \ : \ \varphi(n), \ \delta = \begin{cases} (-1)^{n_0+n_3}, & (0,0,1,1) & \text{if } i=1 \\ (-1)^{n_0+n_2+n_3}, & (0,1,0,1) & \text{if } i=2 \end{cases}. \tag{A64}$$

As mentioned, the first operator corresponds to taste-singlet vector meson; it contains a one component shift. To preserve gauge invariance, these operators have gauge links connecting fields on different sites. Hence, this operator is referred to as a '1-link' operator for the single link connecting $\bar{\chi}$ and χ. The second operator is local and is named so. For the last irrep, the taste vector pseudo-scalar, the operator $\mathcal{O}^{\gamma_5 \otimes \gamma_i}$ also excites the same states but contains a shift in the time direction, so we do not use it.

For the non-zero momentum example irreps considered above, Eqs. (A48) and (A52), we have

- $(0,0,0) \rtimes [(\pi,\pi,0,0),\pi] \rtimes A_1^+$

$$\mathcal{O}^{\gamma_5 \otimes \gamma_i}(\vec{p}=0) \ : \ \varphi(n), \ \delta = \begin{cases} (-1)^{n_0+n_1+n_2}, & (0,0,1,1) & \text{if } i=1 \\ (-1)^{n_0+n_1}, & (0,1,0,1) & \text{if } i=2 \\ (-1)^{n_0+n_1+n_3}, & (0,1,1,0) & \text{if } i=3 \end{cases}. \tag{A65}$$

- $(0,0,\ell) \rtimes [(\pi,\pi,0,0),\pi] \rtimes A_3$

$$\mathcal{O}^{\gamma_5 \otimes \gamma_i}(\vec{p}=[0,0,l]) \ : \ \varphi(n), \ \delta = \begin{cases} (-1)^{n_0+n_1+n_2}, & (0,0,1,1) & \text{if } i=1 \\ (-1)^{n_0+n_1}, & (0,1,0,1) & \text{if } i=2 \end{cases}. \tag{A66}$$

- $(0,0,\ell) \rtimes [(\pi,0,0,\pi),\pi] \rtimes A_1$

$$\mathcal{O}^{\gamma_5 \otimes \gamma_3}(\vec{p}=[0,0,l]) \ : \ \varphi(n) = (-1)^{n_0+n_1+n_3}, \delta = (0,1,1,0). \tag{A67}$$

Here, the first operator excites the rows of an irrep which then splits into two non-zero momentum irreps which are excited by the second and third operators.

5. Connecting staggered observables to the continuum

There are two considerations when connecting an observable computed with staggered quarks to a continuum observable. The first is the subduction from the states in the continuum to the states of the staggered lattice group. As mentioned in Appendix A 2 b, for staggered quarks a $\mathrm{SU}(4)_T$ symmetry emerges in the continuum, meaning all states with the same quantum numbers, but different tastes, are degenerate and have the same properties as the same physical state. This degeneracy is lifted at finite lattice spacing, hence there is a non-trivial spectrum of states for each physical state. A central part of this work is understanding this taste-split spectrum as it pertains to two-pion states. The second consideration is the contribution of the four quark-tastes to the staggered fermion determinant. This is resolved by so-called (fourth-) rooting, the effect of this on the observables computed in this work is discussed in Appendix E.

a. Continuum decomposition

The decomposition from the continuum symmetry group irreps to the lattice irreps discussed above is laid out in Ref. [47]. However, there are some errors in that work, so we reproduce the full discussion here with corrections. Ignoring flavor, subduction from the continuum group to the lattice group is given by the following map:

$$\begin{array}{c} \text{Continuum Group} \\ \mathrm{SU}(4)_T \times \mathrm{SU}(2)_S \times P \times C \\ \downarrow \\ [\mathrm{SU}(2)_L \times \mathrm{SU}(2)_S] \times [\mathrm{SU}(2)_R \times P \times C] \\ \downarrow \\ \text{Staggered Rest Frame Group} \\ \frac{(SW_4 \times \Gamma_{2,2})}{(-E \times -E)} \\ \{R_{ij}, R_{jk}\Xi_{kj}\} \times \{C_0, \Xi_0, \Xi_{123}, C_0\Xi_0 I_S\} \end{array} \longrightarrow \begin{array}{c} \text{Staggered Group w/o Translations} \\ \Gamma_{4,1} \rtimes O_{\mathrm{h}} \\ \{\Xi_\mu, C_0\} \rtimes \{R_{ij}, I_S\} \\ \downarrow \\ \text{Full Staggered Group: } G_{T_0} \\ (Z^3_{N_s/2} \times \Gamma_{4,1}) \rtimes O_{\mathrm{h}} \end{array},$$

where the meaning and role of $\mathrm{SW}_4 \times \Gamma_{2,2}$ is explained below. The symmetry group in the continuum for a flavorless state is $\mathrm{SU}(4)_T \times \mathrm{SU}(2)_S \times P \times C$. [12] Here, P and C are continuum parity and charge conjugation, which are distinct but related to spatial inversion I_S and staggered charge conjugation C_0; $\mathrm{SU}(2)_S$ is the standard continuum spin group with integer and half-integer spin representations; $\mathrm{SU}(4)_T$ is the continuum symmetry group of four degenerate tastes.We have two bosonic representations of $\mathrm{SU}(4)_T$ labelled **0** and **15**. The SU(4) singlet **0** is one dimensional and decomposes to the taste-singlet, $\pi_\xi = (0,0,0,0)$, while the SU(4) fundamental irrep **15** is fifteen dimensional and decomposes to all other tastes.

The 15 taste transformations Ξ_μ, Ξ_5, $\Xi_\mu\Xi_5$, $\Xi_{\mu\nu}$ are generators of the continuum $\mathrm{SU}(4)_T$ but also exist as a subgroup inside it as is the case for the doubling symmetry, Eq. (A10), which has the equivalent group structure. By examining the action of these transformations in momentum space [48], one finds that Ξ_{ij} lie in a $\mathrm{SU}(2)_L$ subgroup while Ξ_0 and $\Xi_{123} \equiv \Xi_1\Xi_2\Xi_3$ lie in a commuting $\mathrm{SU}(2)_R$ subgroup, i.e. $\mathrm{SU}(2)_L \times \mathrm{SU}(2)_R \subset \mathrm{SU}(4)_T$. The bosonic irrep decomposition for this step is given by,

$$\mathrm{SU}(4) \to \mathrm{SU}(2) \times \mathrm{SU}(2), \tag{A68}$$

$$\mathbf{0} \to (0,0), \tag{A69}$$

$$\mathbf{15} \to (0,1) \oplus (1,0) \oplus (1,1), \tag{A70}$$

where 0 and 1 on the RHS are the familiar one-dimensional 'spin 0' and three-dimensional 'spin 1' irreps of SU(2).

[12] Apart from the inconsequential $U_V(1)$ that corresponds to baryon number conservation.

For the second step of the decomposition, parity and charge conjugation correspond to their continuum counterparts, with an additional taste transformation. The relationship between spatial inversion and parity is straightforward to read off from Eq. (A16)

$$I_S = P\Xi_0. \tag{A71}$$

Charge conjugation is more complicated, but the process of extracting it is described Ref. [47]. It amounts to the following procedure, first count the zeros, #0s, in the taste irrep orbit representative vector π_ξ. Then the relationship between the continuum charge conjugation C and lattice charge conjugation C_0 is

$$C_0 = \begin{cases} C, & \text{if } \#0\text{s} = 0, 3, 4 \\ -C, & \text{if } \#0\text{s} = 1, 2 \end{cases}. \tag{A72}$$

Lattice rotations correspond to simultaneous rotations of staggered taste and spin, Eq. (A60), and sit inside the diagonal subgroup of $\mathrm{SU}(2)_L \times \mathrm{SU}(2)_S$, which is subduced into the group generated by $\{\Xi_{kj}, R_{ij}\}$. Rewriting this generating set as

$$\{\tilde{R}_{4i}, R_{ij}\}, \tag{A73}$$

$$\tilde{R}_{4i} \equiv R_{jk}\Xi_{kj}, \tag{A74}$$

gives a group isomorphic to SW_4, the symmetry group of the hypercube, which appears in the map shown above. Below, SW_4 is a useful tool for decomposing continuum states into staggered irreps.

The group $\mathrm{SU}(2)_R \times P \times C$ is subduced into the group generated by the remaining staggered symmetries $\{\Xi_0, \Xi_{123}, I_S, C_0\}$. Using Eqs. (A71) and (A72), where again, rewriting generators

$$\{\Xi_0, \Xi_{123}, C_0\Xi_0 I_S, C_0\}, \tag{A75}$$

gives the defining set of mutually anti-commuting generators of $\Gamma_{2,2}$,

$$\Xi_0^2 = (C_0\Xi_0 I_S)^2 = -C_0^2 = -\Xi_{123}^2 = 1. \tag{A76}$$

The group,

$$(SW_4 \times \Gamma_{2,2})/(-E \times -E), \tag{A77}$$

is the staggered rest frame group and is isomorphic to the group $\Gamma_{4,1} \rtimes O_\mathrm{h}$ in Eq. (A32). The quotient factor, $(-E \times -E)$,[13] ensures only bosonic-type and fermionic-type irreps exist in the direct product, i.e., Abelian irreps of $\Gamma_{2,2}$ are combined with non-projective irreps of SW_4, while the faithful four dimensional irrep of $\Gamma_{2,2}$ is combined with the projective irreps of SW_4. The irreps and characters of SW_4 are given in Refs. [47, 85], however, there are some errors in Table 6 of Ref. [47]. In Ref. [85], Table 3 2a for SW_4 is correct, even though it is subduced from Table 3 3b, which interchanges the characters for $(1, 0)$ and $(0, 1)$. The bosonic irrep part of the character table is reproduced in Table XVI with the classes labelled by class representatives corresponding to Eq. (A73). In the case of bosonic (Abelian) irreps

[13] E denotes the identity element of the respective group.

of $\Gamma_{2,2}$, the homomorphism $\Gamma_{2,2} \to Z_2^4$ furnishes 16 one-dimensional irreps. These irreps are labeled by $\pi_\Gamma = (\xi_0, \xi_{123}, \xi_{I_S}, \xi_C)$, taking values 0 or π. The characters are straightforward and are given in Eq. (B1).

The subduction from $\mathrm{SU}(2)_L \times \mathrm{SU}(2)_S \cong O(4) \to SW_4$ is described in Ref. [85].[14] One restricts $\mathrm{SU}(2)_L \times \mathrm{SU}(2)_S$ to SW_4 using the natural mapping with $O(4)$. It is then straightforward to decompose the representations of the restricted group using the standard character vector algebra (the same process as in Appendix A 3 a). Explicit results for spin $0, 1, 2$ are given here,

$$(0,0) \to \square\square\square\square, \tag{A78}$$
$$(1,0) \to (1,0), \tag{A79}$$
$$(0,1) \to (0,1), \tag{A80}$$
$$(1,1) \to \begin{array}{|c|c|}\hline \multicolumn{1}{|c}{} & \multicolumn{1}{c|}{} \\ \hline \end{array} \oplus \mathbf{6}, \tag{A81}$$
$$(0,2) \to \begin{array}{|c|c|}\hline \multicolumn{1}{|c}{} & \multicolumn{1}{c|}{} \\ \hline \multicolumn{1}{|c}{} & \multicolumn{1}{c|}{} \\ \hline \end{array} \oplus \overline{(0,1)}, \tag{A82}$$
$$(1,2) \to \begin{array}{|c|c|}\hline \multicolumn{1}{|c}{} & \multicolumn{1}{c|}{} \\ \hline \multicolumn{1}{|c}{} & \multicolumn{1}{c|}{} \\ \hline \end{array} \oplus \mathbf{6} \oplus (1,0) \oplus \overline{(1,0)}. \tag{A83}$$

The irrep $\begin{array}{|c|}\hline \multicolumn{1}{|c}{} \\ \hline \multicolumn{1}{|c}{} \\ \hline \multicolumn{1}{|c}{} \\ \hline \end{array}$ in Table XVI appears first in the spin 3 subduction.

For $\mathrm{SU}(2)_R \times P \times C \to \Gamma_{2,2}$, one just needs to subduce $\mathrm{SU}(2)_R \to \{\Xi_0, \Xi_{123}\} \cong \mathrm{D}_4$, which is straightforward for the bosonic case via the homomorphism $\mathrm{D}_4 \to Z_2 \times Z_2$. C_0 and P follow from Eqs. (A71) and (A72). The mapping is given in Ref. [47],

$$\mathrm{SU}(2)_R \to Z_2 \times Z_2, \tag{A84}$$
$$0 \to (0,0), \tag{A85}$$
$$1 \to (\pi,0) \oplus (0,\pi) \oplus (\pi,\pi), \tag{A86}$$

where the irreps and characters for the group $Z_2 \times Z_2$ are given in Table XVII. This completes the second step of the continuum decomposition map. The isomorphism between the rest frame group and Eq. (A32) without translations is straightforward, as they contain the same generating elements, just rearranged. One makes the identification between the classes and matches the character vectors of the irreps. There are 17 irreps/classes in $\Gamma_{2,2}$ and 13 irreps/classes in SW_4 giving a total of 221[15] in the direct product, however 58 of them are removed through the $Z_2 \times Z_2$ quotient giving 163 classes corresponding to the 160 zero momentum bosonic irreps in Table VIII and the 3 fermionic irreps which are not considered here. The similarity between the irreps are given in Table IX.

With this similarity, the first three steps of the decomposition are completed. The final step just follows what is described in Appendix A 3 a. To illustrate the full procedure, the decomposition of the spin-zero meson with $P = -1$ and $C = 1$[16] and momentum in the z direction is performed. The decomposition for other momenta is given in Appendix C 2. Also given in Appendix C 1 is the decomposition of the ρ meson, including the example from

[14] The ordering of $\mathrm{SU}(2)_L \times \mathrm{SU}(2)_S$ is the correct one given the definitions of the $(0,1)$ and $(1,0)$ irreps in Refs. [47, 85], but Ref. [47] subsequently flips the order when carrying out its subduction analysis.

[15] It is a coincidence that the number of irreps/classes coincides with the recurrence of periodical cicadas.

[16] A pion if the correct isospin is chosen.

TABLE IX. Irreps for the isomorphic groups $(SW_4 \times \Gamma_{2,2})/(-E \times -E)$ and $\Gamma_{4,1} \rtimes O_{\rm h}$. The first five rows are the irreps corresponding to row one in Table VIII, the next five are the irreps in row two of that table.

$(SW_4 \times \Gamma_{2,2})/(-E \times -E)$	$\Gamma_{4,1} \rtimes O_{\rm h}$	Dimension
$\square\square\square\square \otimes (\xi_0, \xi_{123}, \xi_{I_S}, \xi_C)$	$[(\xi_0,\xi_1,\xi_2,\xi_3),\xi_C] \rtimes A_0^{e^{\xi_{I_S}}}$	1
$\begin{smallmatrix}\square\\\square\\\square\\\square\end{smallmatrix} \otimes (\xi_0, \xi_{123}, \xi_{I_S}, \xi_C)$	$[(\xi_0,\xi_1,\xi_2,\xi_3),\xi_C] \rtimes A_1^{e^{\xi_{I_S}}}$	1
$\begin{smallmatrix}\square\square\\\square\square\end{smallmatrix} \otimes (\xi_0, \xi_{123}, \xi_{I_S}, \xi_C)$	$[(\xi_0,\xi_1,\xi_2,\xi_3),\xi_C] \rtimes E_0^{e^{\xi_{I_S}}}$	2
$(0,1) \otimes (\xi_0, \xi_{123}, \xi_{I_S}, \xi_C)$	$[(\xi_0,\xi_1,\xi_2,\xi_3),\xi_C] \rtimes T_0^{e^{\xi_{I_S}}}$	3
$\overline{(0,1)} \otimes (\xi_0, \xi_{123}, \xi_{I_S}, \xi_C)$	$[(\xi_0,\xi_1,\xi_2,\xi_3),\xi_C] \rtimes T_1^{e^{\xi_{I_S}}}$	3
$\begin{smallmatrix}\square\square\square\\\square\end{smallmatrix} \otimes (\xi_0, \xi_{123}, \xi_{I_S}, \xi_C)$	$[(\xi_0,\xi_1,\xi_2,\xi_3),\xi_C] \rtimes A_0^{e^{\xi_{I_S}}}$	3
$\begin{smallmatrix}\square\square\\\square\\\square\end{smallmatrix} \otimes (\xi_0, \xi_{123}, \xi_{I_S}, \xi_C)$	$[(\xi_0,\xi_1,\xi_2,\xi_3),\xi_C] \rtimes A_1^{e^{\xi_{I_S}}}$	3
$(1,0) \otimes (\xi_0, \xi_{123}, \xi_{I_S}, \xi_C)$	$[(\xi_0,\xi_1,\xi_2,\xi_3),\xi_C] \rtimes A_2^{e^{\xi_{I_S}}}$	3
$\overline{(1,0)} \otimes (\xi_0, \xi_{123}, \xi_{I_S}, \xi_C)$	$[(\xi_0,\xi_1,\xi_2,\xi_3),\xi_C] \rtimes A_3^{e^{\xi_{I_S}}}$	3
$\mathbf{6} \otimes (\xi_0, \xi_{123}, \xi_{I_S}, \xi_C)$	$[(\xi_0,\xi_1,\xi_2,\xi_3),\xi_C] \rtimes E_0^{e^{\xi_{I_S}}}$	6

Ref. [47] which is repeated but with a corrected decomposition. The continuum spin-zero state can be in the taste-singlet irrep **0** or the taste-fifteen irrep **15**, hence we have

$$(\mathbf{0},0) \to (0,0) \otimes 0 \to \square\square\square\square \otimes (0,0), \tag{A87}$$

$$\begin{aligned}(\mathbf{15},0) \to\ & (1,0) \otimes 1 \oplus (1,0) \otimes 0 \ \oplus\ (0,0) \otimes 1 \to \\ & (1,0) \otimes (\pi,0) \oplus (1,0) \otimes (0,\pi) \oplus (1,0) \otimes (\pi,\pi) \oplus (1,0) \otimes (0,0) \oplus \\ & \square\square\square\square \otimes (\pi,0) \oplus \square\square\square\square \otimes (0,\pi) \oplus \square\square\square\square \otimes (\pi,\pi).\end{aligned} \tag{A88}$$

Proceeding with the mapping from Table IX, using Eqs. (A71) and (A72) with $P=-1$ and $C=1$ and the characters from Table XVII

$$\square\square\square\square \otimes (0,0) \sim (0,0,0) \rtimes [(0,0,0,0),0] \rtimes A_0^- \ :\ \mathcal{O}^{\gamma_5 \otimes 1}(0,0,0), \tag{A89}$$

$$\square\square\square\square \otimes (\pi,0) \sim (0,0,0) \rtimes [(\pi,0,0,0),0] \rtimes A_0^+ \ :\ \mathcal{O}^{\gamma_5 \otimes \gamma_5\gamma_0}(0,0,0), \tag{A90}$$

$$\square\square\square\square \otimes (0,\pi) \sim (0,0,0) \rtimes [(0,\pi,\pi,\pi),\pi] \rtimes A_0^- \ :\ \mathcal{O}^{\gamma_5 \otimes \gamma_0}(0,0,0), \tag{A91}$$

$$\square\square\square\square \otimes (\pi,\pi) \sim (0,0,0) \rtimes [(\pi,\pi,\pi,\pi),0] \rtimes A_0^+ \ :\ \mathcal{O}^{\gamma_5 \otimes \gamma_5}(0,0,0), \tag{A92}$$

$$(1,0) \otimes (\pi,0) \sim (0,0,0) \rtimes [(\pi,\pi,\pi,0),\pi] \rtimes A_2^+ \ :\ \mathcal{O}^{\gamma_5 \otimes \gamma_i}(0,0,0), \tag{A93}$$

$$(1,0) \otimes (0,\pi) \sim (0,0,0) \rtimes [(0,0,0,\pi),0] \rtimes A_2^- \ :\ \mathcal{O}^{\gamma_5 \otimes \gamma_5\gamma_i}(0,0,0), \tag{A94}$$

$$(1,0) \otimes (\pi,\pi) \sim (0,0,0) \rtimes [(\pi,0,0,\pi),\pi] \rtimes A_2^+ \ :\ \mathcal{O}^{\gamma_5 \otimes \gamma_i\gamma_0}(0,0,0), \tag{A95}$$

$$(1,0)\otimes(0,0)\sim(0,0,0)\rtimes[(0,\pi,\pi,0),\pi]\rtimes A_2^-\ :\ \mathcal{O}^{\gamma_5\otimes\gamma_i\gamma_j}(0,0,0), \tag{A96}$$

where corresponding operators, using Appendix A 4, are also given. The first four irreps are one-dimensional, the last four are three-dimensional, giving $4+12=16$ 'pion' states, as expected. For non-zero momentum in the continuum, one decomposes the zero momentum lattice irreps. For momentum $(0,0,p_z)$ one has,

$$(0,0,0)\rtimes[(0,0,0,0),0]\rtimes A_0^-\to\Big\{(0,0,1)\rtimes[(0,0,0,0),0]\rtimes A_1:\mathcal{O}^{\gamma_5\otimes 1}(0,0,1) \tag{A97}$$

$$(0,0,0)\rtimes[(\pi,0,0,0),0]\rtimes A_0^+\to\Big\{(0,0,1)\rtimes[(\pi,0,0,0),0]\rtimes A_0:\mathcal{O}^{\gamma_5\otimes\gamma_5\gamma_0}(0,0,1) \tag{A98}$$

$$(0,0,0)\rtimes[(0,\pi,\pi,\pi),\pi]\rtimes A_0^-\to\Big\{(0,0,1)\rtimes[(0,\pi,\pi,\pi),\pi]\rtimes A_1:\mathcal{O}^{\gamma_5\otimes\gamma_0}(0,0,1) \tag{A99}$$

$$(0,0,0)\rtimes[(\pi,\pi,\pi,\pi),0]\rtimes A_0^+\to\Big\{(0,0,1)\rtimes[(\pi,\pi,\pi,\pi),0]\rtimes A_0:\mathcal{O}^{\gamma_5\otimes\gamma_5}(0,0,1) \tag{A100}$$

$$(0,0,0)\rtimes[(\pi,\pi,\pi,0),\pi]\rtimes A_2^+\to\begin{cases}(0,0,1)\rtimes[(\pi,0,\pi,\pi),\pi]\rtimes A_2:\mathcal{O}^{\gamma_5\otimes\gamma_{i\neq 3}}(0,0,1)\\(0,0,1)\rtimes[(\pi,\pi,\pi,0),\pi]\rtimes A_1:\mathcal{O}^{\gamma_5\otimes\gamma_3}(0,0,1)\end{cases} \tag{A101}$$

$$(0,0,0)\rtimes[(0,0,0,\pi),0]\rtimes A_2^-\to\begin{cases}(0,0,1)\rtimes[(0,0,0,\pi),0]\rtimes A_0:\mathcal{O}^{\gamma_5\otimes\gamma_5\gamma_3}(0,0,1)\\(0,0,1)\rtimes[(0,0,\pi,0),0]\rtimes A_2:\mathcal{O}^{\gamma_5\otimes\gamma_5\gamma_{i\neq 3}}(0,0,1)\end{cases} \tag{A102}$$

$$(0,0,0)\rtimes[(\pi,0,0,\pi),\pi]\rtimes A_2^+\to\begin{cases}(0,0,1)\rtimes[(\pi,0,0,\pi),\pi]\rtimes A_1:\mathcal{O}^{\gamma_5\otimes\gamma_3\gamma_0}(0,0,1)\\(0,0,1)\rtimes[(\pi,0,\pi,0),\pi]\rtimes A_3,\ \mathcal{O}^{\gamma_5\otimes\gamma_{i\neq 3}\gamma_0}(0,0,1)\end{cases} \tag{A103}$$

$$(0,0,0)\rtimes[(0,\pi,\pi,0),\pi]\rtimes A_2^-\to\begin{cases}(0,0,1)\rtimes[(0,0,\pi,\pi),\pi]\rtimes A_3:\mathcal{O}^{\gamma_5\otimes\gamma_{i\neq 3}\gamma_3}(0,0,1)\\(0,0,1)\rtimes[(0,\pi,\pi,0),\pi]\rtimes A_0:\mathcal{O}^{\gamma_5\otimes\gamma_{i\neq 3}\gamma_{j\neq 3}}(0,0,1)\end{cases} \tag{A104}$$

Here, again the last four irreps undergo taste orbit splitting at non-zero momentum. It is also important to note that the operators given will excite states in irreps of both parities for ξ_0 and ξ_3.

Appendix B: Character tables

This appendix contains the character tables used to construct the irreducible representations in Appendix A. These are, again, contained in Ref. [47]. However, we repeat them here to address slight notational differences in irrep labelling and minor errors in some tables in that work.

1. Character tables for little groups

Here we given the character tables for the little groups of the taste-orbit under rotations defined in Table VIII. The two $(0,0,0)$ momentum taste little groups, O_h and $D_{4\mathrm{h}}$, are given

in Tables X and XI. For momentum $(0,0,n)$, the two little groups, D_4 and C_{2v}, are given in Tables XII and XIII. The remaining unique group character tables, D_3 and Z_2, are given in Tables XIV and XV. Where the little group structure is repeated for different momentum and taste orbits, we indicate in the caption and include the unique rotation group elements for each case in the table.

TABLE X. Character table for the $\vec{p} = 2\pi(0,0,0)/L$, $\pi_\xi = (\xi_0, \pi, \pi, \pi)$ little group O_h.

Rep. element	Class size	A_0^+	A_0^-	A_1^+	A_1^-	E_0^+	E_0^-	T_0^+	T_0^-	T_1^+	T_1^-
E	1	1	1	1	1	2	2	3	3	3	3
I_S	1	1	−1	1	−1	2	−2	3	−3	3	−3
$R_{12}R_{12}$	3	1	1	1	1	2	2	−1	−1	−1	−1
$R_{12}R_{12}I_S$	3	1	−1	1	−1	2	−2	−1	1	−1	1
R_{12}	6	1	1	−1	−1	0	0	1	1	−1	−1
$R_{12}I_S$	6	1	−1	−1	1	0	0	1	−1	−1	1
$R_{12}R_{12}R_{23}$	6	1	1	−1	−1	0	0	−1	−1	1	1
$R_{12}R_{12}R_{23}I_S$	6	1	−1	−1	1	0	0	−1	1	1	−1
$R_{12}R_{23}$	8	1	1	1	1	−1	−1	0	0	0	0
$R_{12}R_{23}I_S$	8	1	−1	1	−1	−1	1	0	0	0	0

TABLE XI. Character table for the $\vec{p} = 2\pi(0,0,0)/L$, $\pi_\xi = (\xi_0, 0, \pi, \pi)$ little group D_{4h}.

Rep. element	Class size	A_0^+	A_0^-	A_1^+	A_1^-	A_2^+	A_2^-	A_3^+	A_3^-	E_0^+	E_0^-
E	1	1	1	1	1	1	1	1	1	2	2
I_S	1	1	−1	1	−1	1	−1	1	−1	2	−2
$R_{23}R_{23}$	1	1	1	1	1	1	1	1	1	−2	−2
$R_{23}R_{23}I_S$	1	1	−1	1	−1	1	−1	1	−1	−2	2
$R_{12}R_{12}$	2	1	1	1	1	−1	−1	−1	−1	0	0
$R_{12}R_{12}I_S$	2	1	−1	1	−1	−1	1	−1	1	0	0
$R_{12}R_{12}R_{23}$	2	1	1	−1	−1	−1	−1	1	1	0	0
$R_{12}R_{12}R_{23}I_S$	2	1	−1	−1	1	−1	1	1	−1	0	0
R_{23}	2	1	1	−1	−1	1	1	−1	−1	0	0
$R_{23}I_S$	2	1	−1	−1	1	1	−1	−1	1	0	0

TABLE XII. Character table for the $\vec{p} = 2\pi(0,0,\ell)/L$, $\pi_\xi = (\xi_0, \pi, \pi, \xi_3)$ little group D_4.

Rep. element	Class size	A_0	A_1	A_2	A_3	E_0
E	1	1	1	1	1	2
$R_{12}R_{12}$	1	1	1	1	1	-2
R_{12}	2	1	1	-1	-1	0
$R_{12}R_{23}R_{23}I_S$	2	1	-1	-1	1	0
$R_{23}R_{23}I_S$	2	1	-1	1	-1	0

TABLE XIII. Character table for the $\vec{p} = 2\pi(0,0,\ell)/L$, $\pi_\xi = (\xi_0, 0, \pi, \xi_3)$ and the $\vec{p} = 2\pi/(\ell,\ell,0)/L$, $\pi_\xi = (\xi_0, \pi, \pi, \xi_3)$ little group C_{2v}.

Rep. element	Class size	A_0	A_1	A_2	A_3
E	1	1	1	1	1
$R_{12}R_{12}$ / $R_{12}R_{12}I_S$	1	1	1	-1	-1
$R_{23}R_{23}I_S$ / $R_{12}R_{23}R_{23}I_S$	1	1	-1	1	-1
$R_{31}R_{31}I_S$ / $R_{23}R_{23}R_{12}$	1	1	-1	-1	1

TABLE XIV. Character table for the $\vec{p} = 2\pi(\ell,\ell,\ell)/L$, $\pi_\xi = (\xi_0, \pi, \pi, \pi)$ little group D_3.

Rep. element	Class size	A_0	A_1	E_0
E	1	1	1	2
$R_{23}R_{12}$	2	1	1	-1
$R_{12}R_{12}R_{23}I_S$	3	1	-1	0

TABLE XV. Character table for the $\vec{p} = 2\pi/(\ell,\ell,0)/L$, $\pi_\xi = (\xi_0, 0, \pi, \xi_3)$, $\vec{p} = 2\pi(\ell,\ell,\ell)/L$, $\pi_\xi = (\xi_0, 0, \pi, \pi)$, $\vec{p} = 2\pi(\ell,\ell,m)/L$, $\pi_\xi = (\xi_0, \pi, \pi, \pi)$ and $\vec{p} = 2\pi(0,\ell,m)/L$, $\pi_\xi = (\xi_0, \pi, \pi, \pi)$ little group Z_2.

Rep. element	Class size	A_0	A_1
E	1	1	1
$R_{12}R_{12}I_S$ / $R_{12}R_{12}R_{23}I_S$ / $R_{12}R_{23}R_{23}I_S$ / $R_{23}R_{23}I_S$	1	1	-1

TABLE XVI. Character table for the bosonic irreps of SW_4, in agreement with Ref. [85] but correcting errors in  ,  , and  of Ref. [47].

Label	Rep. element	Class size						$(1,0)$	$(0,1)$	$\overline{(1,0)}$	$\overline{(0,1)}$	**6**
I	E	1	1	1	2	3	3	3	3	3	3	6
II	$R_{12}R_{12}$	6	1	1	2	3	3	−1	−1	−1	−1	−2
III	$R_{12}R_{12}\tilde{R}_{43}\tilde{R}_{43}$	1	1	1	2	3	3	3	3	3	3	6
IV	R_{12}	12	1	−1	0	1	−1	1	1	−1	−1	0
V	$R_{12}R_{12}R_{23}$	24	1	−1	0	1	−1	−1	−1	1	1	0
VI	$\tilde{R}_{43}R_{12}R_{12}$	12	1	−1	0	1	−1	1	1	−1	−1	0
VII	$R_{12}R_{23}$	32	1	1	−1	0	0	0	0	0	0	0
VIII	$\tilde{R}_{43}R_{12}R_{12}R_{23}$	32	1	1	−1	0	0	0	0	0	0	0
IX	$R_{12}R_{23}\tilde{R}_{43}$	24	1	−1	0	−1	1	1	−1	−1	1	0
X	$R_{12}R_{23}\tilde{R}_{42}$	24	1	−1	0	−1	1	−1	1	1	−1	0
XI	$R_{12}\tilde{R}_{43}R_{23}R_{23}$	12	1	1	2	−1	−1	−1	−1	−1	−1	2
XII	$\tilde{R}_{43}R_{12}R_{12}R_{12}$	6	1	1	2	−1	−1	−1	3	−1	3	−2
XIII	$R_{12}\tilde{R}_{43}$	6	1	1	2	−1	−1	3	−1	3	−1	−2

2. Character tables for staggered rest frame groups

The characters for the bosonic irreps of the group SW_4 are given in Table XVI. A mapping to the class labelling in Refs. [47, 85] is given in the first column. The first four irreps are induced from the symmetric group S_4. The irreps, $(1,0)$ and $(0,1)$, are subduced from the full four-dimensional rotation $O(4) \cong \mathrm{SU}(2) \times \mathrm{SU}(2)$ and remain irreducible. The penultimate two, $\overline{(1,0)}$ and $\overline{(0,1)}$ are the product of the previous two with  . In the last column, **6** is a six-dimensional irrep obtained from $O(4)$ [85].

For the bosonic case, any group element g of $\Gamma_{2,2}$ can be represented as a four vector Γ which takes values 0 or 1 depending on what generators g contains. The characters for the bosonic irreps, labelled by π_Γ, of $\Gamma_{2,2}$ are then given by

$$\chi^{\pi_\Gamma}(g) = e^{i\pi_\Gamma \cdot \Gamma} \tag{B1}$$

Leaving charge conjugation, C_0, and spatial inversion, I_S, out of this group gives the corresponding character table for the bosonic representations of $Z_2 \times Z_2$, Table XVII.

3. Rest frame groups isomorphism

The staggered lattice group has two useful representations at zero momentum, the first representation,

$$(SW_4 \times \Gamma_{2,2})/(-E \times -E), \tag{B2}$$

TABLE XVII. Character table for the $Z_2 \times Z_2$ group corresponding to the bosonic representations of $\{\Xi_0, \Xi_{123}\}$.

Rep. element	Class size	$(0,0)$	$(\pi,0)$	$(0,\pi)$	(π,π)
E	1	1	1	1	1
Ξ_0	1	1	-1	1	-1
Ξ_{123}	1	1	1	-1	-1
$\Xi_0\Xi_{123}$	1	1	-1	-1	1

is useful for subducing from the continuum. It has the generating elements,

$$\{R_{ij}, \tilde{R}_{4i} \equiv R_{jk}\Xi_{kj}\} \times \{\Xi_0, \Xi_{123}, C_0\Xi_0 I_S, C_0\} \tag{B3}$$
$$\{\Xi_0, \Xi_{123}, C_0\Xi_0 I_S, C_0\} \equiv \{\Gamma_1, \Gamma_2, \Gamma_3, \Gamma_4\}. \tag{B4}$$

The second representation of the group,

$$\Gamma_{4,1} \rtimes O_{\rm h}, \tag{B5}$$

is useful for considering states at non-zero momentum by the natural extension, $T_i \rtimes \Gamma_{4,1} \rtimes O_{\rm h}$. It has generating elements,

$$\{\Xi_0, \Xi_1, \Xi_2, \Xi_3, C_0\} \rtimes \{R_{ij}, I_s\} \tag{B6}$$

The similarity between the irreps is given in Table IX.

Appendix C: Staggered irreps

1. The staggered rho

Using the tools described in Appendix A 5 a, the full the decomposition of the vector meson with negative parity and negative charge conjugation is given here for zero momentum.

$$(0,1) \to (0,1) \otimes 0 \to (0,1) \otimes (0,0) \tag{C1}$$
$$\begin{aligned}(15,1) \to\ & (1,1) \otimes 1 \ \oplus\ (1,1) \otimes 0 \ \oplus\ (0,1) \otimes 1 \to \\ & \ydiagram{3,1} \otimes (\pi,0) \ \oplus\ \ydiagram{3,1} \otimes (0,\pi) \ \oplus\ \ydiagram{3,1} \otimes (\pi,\pi) \ \oplus\ \ydiagram{3,1} \otimes (0,0) \ \oplus \\ & \mathbf{6} \otimes (\pi,0) \ \oplus\ \mathbf{6} \otimes (0,\pi) \ \oplus\ \mathbf{6} \otimes (\pi,\pi) \ \oplus\ \mathbf{6} \otimes (0,0) \ \oplus \\ & (0,1) \otimes (\pi,0) \ \oplus\ (0,1) \otimes (0,\pi) \ \oplus\ (0,1) \otimes (\pi,\pi)\end{aligned} \tag{C2}$$

The term $(0,1) \otimes ((\pi,0) \oplus (0,\pi) \oplus (\pi,\pi))$ was mistakenly written with as $(1,0) \otimes \ldots$ in Ref. [47]. Proceeding with the mapping from Table IX, using Eqs. (A71) and (A72) with $P = -1$ and $C = -1$ and the characters from Table XVII

$$(0,1) \otimes (0,0) \sim (0,0,0) \rtimes [(0,0,0,0), \pi] \rtimes T_0^- \ :\ \mathcal{O}^{\gamma_i \otimes 1}(0,0,0) \tag{C3}$$
$$(0,1) \otimes (\pi,0) \sim (0,0,0) \rtimes [(\pi,0,0,0), \pi] \rtimes T_0^+ \ :\ \mathcal{O}^{\gamma_i \otimes \gamma_5\gamma_0}(0,0,0) \tag{C4}$$
$$(0,1) \otimes (0,\pi) \sim (0,0,0) \rtimes [(0,\pi,\pi,\pi), 0] \rtimes T_0^- \ :\ \mathcal{O}^{\gamma_i \otimes \gamma_0}(0,0,0) \tag{C5}$$
$$(0,1) \otimes (\pi,\pi) \sim (0,0,0) \rtimes [(\pi,\pi,\pi,\pi), \pi] \rtimes T_0^+ \ :\ \mathcal{O}^{\gamma_i \otimes \gamma_5}(0,0,0) \tag{C6}$$

$$\begin{array}{|c|c|c|}\hline \\ \hline\end{array} \otimes (0,0) \sim (0,0,0) \rtimes [(0,\pi,\pi,0),0] \rtimes A_0^- \;:\; \mathcal{O}^{\gamma_i \otimes \gamma_j \gamma_k}(0,0,0) \tag{C7}$$

$$\begin{array}{|c|c|c|}\hline \\ \hline\end{array} \otimes (\pi,0) \sim (0,0,0) \rtimes [(\pi,\pi,\pi,0),0] \rtimes A_0^+ \;:\; \mathcal{O}^{\gamma_i \otimes \gamma_i}(0,0,0) \tag{C8}$$

$$\begin{array}{|c|c|c|}\hline \\ \hline\end{array} \otimes (0,\pi) \sim (0,0,0) \rtimes [(0,0,0,\pi),\pi] \rtimes A_0^- \;:\; \mathcal{O}^{\gamma_i \otimes \gamma_5 \gamma_i}(0,0,0) \tag{C9}$$

$$\begin{array}{|c|c|c|}\hline \\ \hline\end{array} \otimes (\pi,\pi) \sim (0,0,0) \rtimes [(\pi,0,0,\pi),0] \rtimes A_0^+ \;:\; \mathcal{O}^{\gamma_i \otimes \gamma_i \gamma_0}(0,0,0) \tag{C10}$$

$$\mathbf{6} \otimes (\pi,0) \sim (0,0,0) \rtimes [(\pi,\pi,\pi,0),0] \rtimes E_0^+ \;:\; \mathcal{O}^{\gamma_i \otimes \gamma_j}(0,0,0) \tag{C11}$$

$$\mathbf{6} \otimes (0,\pi) \sim (0,0,0) \rtimes [(0,0,0,\pi),\pi] \rtimes E_0^- \;:\; \mathcal{O}^{\gamma_i \otimes \gamma_5 \gamma_j}(0,0,0) \tag{C12}$$

$$\mathbf{6} \otimes (\pi,\pi) \sim (0,0,0) \rtimes [(\pi,0,0,\pi),0] \rtimes E_0^+ \;:\; \mathcal{O}^{\gamma_i \otimes \gamma_j \gamma_0}(0,0,0) \tag{C13}$$

$$\mathbf{6} \otimes (0,0) \sim (0,0,0) \rtimes [(0,\pi,\pi,0),0] \rtimes E_0^- \;:\; \mathcal{O}^{\gamma_i \otimes \gamma_i \gamma_j}(0,0,0) \tag{C14}$$

In this work, we use the states and operators associated with Eq. (C3), called the 'one-link' or taste-singlet ρ. Continuing with the example from Ref. [47], giving the ρ momentum $(0,0,p_z)$ results in

$$(0,0,0) \rtimes [(\pi,0,0,0),\pi] \rtimes T_0^+ \to \begin{cases} (0,0,1) \rtimes [(\pi,0,0,0),\pi] \rtimes A_1 \;:\; \mathcal{O}^{\gamma_3 \otimes \gamma_5 \gamma_0}(0,0,1) \\ (0,0,1) \rtimes [(\pi,0,0,0),\pi] \rtimes E_0 \;:\; \mathcal{O}^{\gamma_{i\neq 3} \otimes \gamma_5 \gamma_0}(0,0,1) \end{cases} \tag{C15}$$

$$(0,0,0) \rtimes [(0,\pi,\pi,\pi),0] \rtimes T_0^- \to \begin{cases} (0,0,1) \rtimes [(0,\pi,\pi,\pi),0] \rtimes A_0 \;:\; \mathcal{O}^{\gamma_3 \otimes \gamma_0}(0,0,1) \\ (0,0,1) \rtimes [(0,\pi,\pi,\pi),0] \rtimes E_0 \;:\; \mathcal{O}^{\gamma_{i\neq 3} \otimes \gamma_0}(0,0,1) \end{cases} \tag{C16}$$

$$(0,0,0) \rtimes [(\pi,\pi,\pi,\pi),\pi] \rtimes T_0^+ \to \begin{cases} (0,0,1) \rtimes [(\pi,\pi,\pi,\pi),\pi] \rtimes A_1 \;:\; \mathcal{O}^{\gamma_3 \otimes \gamma_5}(0,0,1) \\ (0,0,1) \rtimes [(\pi,\pi,\pi,\pi),\pi] \rtimes E_0 \;:\; \mathcal{O}^{\gamma_{i\neq 3} \otimes \gamma_5}(0,0,1) \end{cases} \tag{C17}$$

$$(0,0,0) \rtimes [(0,\pi,\pi,0),0] \rtimes A_0^- \to \begin{cases} (0,0,1) \rtimes [(0,\pi,\pi,0),0] \rtimes A_1 \;:\; \mathcal{O}^{\gamma_3 \otimes \gamma_{j\neq i} \gamma_{k\neq i}}(0,0,1) \\ (0,0,1) \rtimes [(0,0,\pi,\pi),0] \rtimes A_1 \;:\; \mathcal{O}^{\gamma_{i\neq 3} \otimes \gamma_{j\neq i} \gamma_{k\neq i}}(0,0,1) \end{cases} \tag{C18}$$

$$(0,0,0) \rtimes [(\pi,\pi,\pi,0),0] \rtimes A_0^+ \to \begin{cases} (0,0,1) \rtimes [(\pi,\pi,\pi,0),0] \rtimes A_0 \;:\; \mathcal{O}^{\gamma_3 \otimes \gamma_3}(0,0,1) \\ (0,0,1) \rtimes [(\pi,0,\pi,\pi),0] \rtimes A_0 \;:\; \mathcal{O}^{\gamma_{i\neq 3} \otimes \gamma_i}(0,0,1) \end{cases} \tag{C19}$$

$$(0,0,0) \rtimes [(0,0,0,\pi),\pi] \rtimes A_0^- \to \begin{cases} (0,0,1) \rtimes [(0,0,0,\pi),\pi] \rtimes A_1 \;:\; \mathcal{O}^{\gamma_3 \otimes \gamma_5 \gamma_3}(0,0,1) \\ (0,0,1) \rtimes [(0,0,\pi,0),\pi] \rtimes A_1 \;:\; \mathcal{O}^{\gamma_{i\neq 3} \otimes \gamma_5 \gamma_i}(0,0,1) \end{cases} \tag{C20}$$

$$(0,0,0) \rtimes [(\pi,0,0,\pi),0] \rtimes A_0^+ \to \begin{cases} (0,0,1) \rtimes [(\pi,0,0,\pi),0] \rtimes A_0 \;:\; \mathcal{O}^{\gamma_3 \otimes \gamma_3 \gamma_0}(0,0,1) \\ (0,0,1) \rtimes [(\pi,0,\pi,0),0] \rtimes A_0 \;:\; \mathcal{O}^{\gamma_{i\neq 3} \otimes \gamma_i \gamma_0}(0,0,1) \end{cases} \tag{C21}$$

$$(0,0,0) \rtimes [(0,\pi,\pi,0),0] \rtimes E_0^- \to \begin{cases} (0,0,1) \rtimes [(0,\pi,\pi,0),0] \rtimes E_0 \;:\; \mathcal{O}^{\gamma_{i\neq 3} \otimes \gamma_i \gamma_{j\neq i,3}}(0,0,1) \\ (0,0,1) \rtimes [(0,0,\pi,\pi),0] \rtimes A_0 \;:\; \mathcal{O}^{\gamma_{i\neq 3} \otimes \gamma_i \gamma_3}(0,0,1) \\ (0,0,1) \rtimes [(0,0,\pi,\pi),0] \rtimes A_2 \;:\; \mathcal{O}^{\gamma_3 \otimes \gamma_{i\neq 3} \gamma_3}(0,0,1) \end{cases} \tag{C22}$$

$$(0,0,0)\rtimes[(\pi,\pi,\pi,0),0]\rtimes E_0^+\to\begin{cases}(0,0,1)\rtimes[(\pi,\pi,\pi,0),0]\rtimes E_0 & : \mathcal{O}^{\gamma_{i\neq 3}\otimes\gamma_3}(0,0,1)\\ (0,0,1)\rtimes[(\pi,0,\pi,\pi),0]\rtimes A_1 & : \mathcal{O}^{\gamma_{i\neq 3}\otimes\gamma_{j\neq 3}\gamma_3}(0,0,1)\\ (0,0,1)\rtimes[(\pi,0,\pi,\pi),0]\rtimes A_3 & : \mathcal{O}^{\gamma_3\otimes\gamma_{j\neq 3}}(0,0,1)\end{cases} \tag{C23}$$

$$(0,0,0)\rtimes[(0,0,0,\pi),\pi]\rtimes E_0^-\to\begin{cases}(0,0,1)\rtimes[(0,0,0,\pi),\pi]\rtimes E_0 & : \mathcal{O}^{\gamma_{i\neq 3}\otimes\gamma_5\gamma_3}(0,0,1)\\ (0,0,1)\rtimes[(0,0,\pi,0),\pi]\rtimes A_0 & : \mathcal{O}^{\gamma_{i\neq 3}\otimes\gamma_5\gamma_{j\neq 3}}(0,0,1)\\ (0,0,1)\rtimes[(0,0,\pi,0),\pi]\rtimes A_3 & : \mathcal{O}^{\gamma_3\otimes\gamma_5\gamma_{j\neq 3}}(0,0,1)\end{cases} \tag{C24}$$

$$(0,0,0)\rtimes[(\pi,0,0,\pi),0]\rtimes E_0^+\to\begin{cases}(0,0,1)\rtimes[(\pi,0,0,\pi),0]\rtimes E_0 & : \mathcal{O}^{\gamma_{i\neq 3}\otimes\gamma_3\gamma_0}(0,0,1)\\ (0,0,1)\rtimes[(\pi,0,\pi,0),0]\rtimes A_1 & : \mathcal{O}^{\gamma_{i\neq 3}\otimes\gamma_{j\neq 3}\gamma_0}(0,0,1)\\ (0,0,1)\rtimes[(\pi,0,\pi,0),0]\rtimes A_2 & : \mathcal{O}^{\gamma_3\otimes\gamma_{j\neq 3}\gamma_0}(0,0,1)\end{cases} \tag{C25}$$

Giving a different breakdown as to what is described in Ref. [47]. The breakdown in that work is likely incorrect due to the aforementioned issue in footnote 8 of this appendix. Alongside this, there is also a further error in the decomposition to non-zero momentum which the above breakdown corrects.

2. The staggered pion

The full the decomposition of the pseudo-scalar with $P=-1$, and $C=1$ is given here for the range of momentum considered in this work. Using the results from Appendix A 5 a, the zero-momentum irreps and operators are

$$\begin{aligned}(0,0)&\to(0,0)\otimes 0\to \square\square\square\square\otimes(0,0),\\ (15,0)&\to(1,0)\otimes 1\ \oplus\ (1,0)\otimes 0\ \oplus\ (0,0)\otimes 1\to\\ &\quad(1,0)\otimes(\pi,0)\ \oplus\ (1,0)\otimes(0,\pi)\ \oplus\ (1,0)\otimes(\pi,\pi)\ \oplus\ (1,0)\otimes(0,0)\ \oplus\\ &\quad\square\square\square\square\otimes(\pi,0)\ \oplus\ \square\square\square\square\otimes(0,\pi)\ \oplus\ \square\square\square\square\otimes(\pi,\pi).\end{aligned} \tag{C26}$$

Relating these irreps to the irreps of Eq. (A32),

$$\square\square\square\square\otimes(0,0)\sim(0,0,0)\rtimes[(0,0,0,0),0]\rtimes A_0^-\ :\ \mathcal{O}^{\gamma_5\otimes 1}(0,0,0), \tag{C27}$$
$$\square\square\square\square\otimes(\pi,0)\sim(0,0,0)\rtimes[(\pi,0,0,0),0]\rtimes A_0^+\ :\ \mathcal{O}^{\gamma_5\otimes\gamma_5\gamma_0}(0,0,0), \tag{C28}$$
$$\square\square\square\square\otimes(0,\pi)\sim(0,0,0)\rtimes[(0,\pi,\pi,\pi),\pi]\rtimes A_0^-\ :\ \mathcal{O}^{\gamma_5\otimes\gamma_0}(0,0,0), \tag{C29}$$
$$\square\square\square\square\otimes(\pi,\pi)\sim(0,0,0)\rtimes[(\pi,\pi,\pi,\pi),0]\rtimes A_0^+\ :\ \mathcal{O}^{\gamma_5\otimes\gamma_5}(0,0,0), \tag{C30}$$
$$(1,0)\otimes(\pi,0)\sim(0,0,0)\rtimes[(\pi,\pi,\pi,0),\pi]\rtimes A_2^+\ :\ \mathcal{O}^{\gamma_5\otimes\gamma_i}(0,0,0), \tag{C31}$$
$$(1,0)\otimes(0,\pi)\sim(0,0,0)\rtimes[(0,0,0,\pi),0]\rtimes A_2^-\ :\ \mathcal{O}^{\gamma_5\otimes\gamma_5\gamma_i}(0,0,0), \tag{C32}$$
$$(1,0)\otimes(\pi,\pi)\sim(0,0,0)\rtimes[(\pi,0,0,\pi),\pi]\rtimes A_2^+\ :\ \mathcal{O}^{\gamma_5\otimes\gamma_i\gamma_0}(0,0,0), \tag{C33}$$
$$(1,0)\otimes(0,0)\sim(0,0,0)\rtimes[(0,\pi,\pi,0),\pi]\rtimes A_2^-\ :\ \mathcal{O}^{\gamma_5\otimes\gamma_i\gamma_j}(0,0,0). \tag{C34}$$

The $(0,0,1)$ momentum subduction is given by

$$(0,0,0)\rtimes[(0,0,0,0),0]\rtimes A_0^-\to\Big\{(0,0,1)\rtimes[(0,0,0,0),0]\rtimes A_1:\mathcal{O}^{\gamma_5\otimes 1}(0,0,1) \tag{C35}$$

$$(0,0,0) \rtimes [(\pi,0,0,0),0] \rtimes A_0^+ \to \Big\{ (0,0,1) \rtimes [(\pi,0,0,0),0] \rtimes A_0 : \mathcal{O}^{\gamma_5 \otimes \gamma_5 \gamma_0}(0,0,1) \tag{C36}$$

$$(0,0,0) \rtimes [(0,\pi,\pi,\pi),\pi] \rtimes A_0^- \to \Big\{ (0,0,1) \rtimes [(0,\pi,\pi,\pi),\pi] \rtimes A_1 : \mathcal{O}^{\gamma_5 \otimes \gamma_0}(0,0,1) \tag{C37}$$

$$(0,0,0) \rtimes [(\pi,\pi,\pi,\pi),0] \rtimes A_0^+ \to \Big\{ (0,0,1) \rtimes [(\pi,\pi,\pi,\pi),0] \rtimes A_0 : \mathcal{O}^{\gamma_5 \otimes \gamma_5}(0,0,1) \tag{C38}$$

$$(0,0,0) \rtimes [(\pi,\pi,\pi,0),\pi] \rtimes A_2^+ \to \begin{cases} (0,0,1) \rtimes [(\pi,0,\pi,\pi),\pi] \rtimes A_2 : \mathcal{O}^{\gamma_5 \otimes \gamma_{i\neq 3}}(0,0,1) \\ (0,0,1) \rtimes [(\pi,\pi,\pi,0),\pi] \rtimes A_1 : \mathcal{O}^{\gamma_5 \otimes \gamma_3}(0,0,1) \end{cases} \tag{C39}$$

$$(0,0,0) \rtimes [(0,0,0,\pi),0] \rtimes A_2^- \to \begin{cases} (0,0,1) \rtimes [(0,0,0,\pi),0] \rtimes A_0 : \mathcal{O}^{\gamma_5 \otimes \gamma_5 \gamma_3}(0,0,1) \\ (0,0,1) \rtimes [(0,0,\pi,0),0] \rtimes A_2 : \mathcal{O}^{\gamma_5 \otimes \gamma_5 \gamma_{i\neq 3}}(0,0,1) \end{cases} \tag{C40}$$

$$(0,0,0) \rtimes [(\pi,0,0,\pi),\pi] \rtimes A_2^+ \to \begin{cases} (0,0,1) \rtimes [(\pi,0,0,\pi),\pi] \rtimes A_1 : \mathcal{O}^{\gamma_5 \otimes \gamma_3 \gamma_0}(0,0,1) \\ (0,0,1) \rtimes [(\pi,0,\pi,0),\pi] \rtimes A_3 : \mathcal{O}^{\gamma_5 \otimes \gamma_{i\neq 3} \gamma_0}(0,0,1) \end{cases} \tag{C41}$$

$$(0,0,0) \rtimes [(0,\pi,\pi,0),\pi] \rtimes A_2^- \to \begin{cases} (0,0,1) \rtimes [(0,0,\pi,\pi),\pi] \rtimes A_3 : \mathcal{O}^{\gamma_5 \otimes \gamma_{i\neq 3} \gamma_3}(0,0,1) \\ (0,0,1) \rtimes [(0,\pi,\pi,0),\pi] \rtimes A_0 : \mathcal{O}^{\gamma_5 \otimes \gamma_{i\neq 3} \gamma_{j\neq 3}}(0,0,1) \end{cases} \tag{C42}$$

The $(1,1,0)$ momentum momentum subduction is given by

$$(0,0,0) \rtimes [(0,0,0,0),0] \rtimes A_0^- \to \Big\{ (1,1,0) \rtimes [(0,0,0,0),0] \rtimes A_1 : \mathcal{O}^{\gamma_5 \otimes 1}(1,1,0) \tag{C43}$$

$$(0,0,0) \rtimes [(\pi,0,0,0),0] \rtimes A_0^+ \to \Big\{ (1,1,0) \rtimes [(\pi,0,0,0),0] \rtimes A_0 : \mathcal{O}^{\gamma_5 \otimes \gamma_5 \gamma_0}(1,1,0) \tag{C44}$$

$$(0,0,0) \rtimes [(0,\pi,\pi,\pi),\pi] \rtimes A_0^- \to \Big\{ (1,1,0) \rtimes [(0,\pi,\pi,\pi),\pi] \rtimes A_1 : \mathcal{O}^{\gamma_5 \otimes \gamma_0}(1,1,0) \tag{C45}$$

$$(0,0,0) \rtimes [(\pi,\pi,\pi,\pi),0] \rtimes A_0^+ \to \Big\{ (1,1,0) \rtimes [(\pi,\pi,\pi,\pi),0] \rtimes A_0 : \mathcal{O}^{\gamma_5 \otimes \gamma_5}(1,1,0) \tag{C46}$$

$$(0,0,0) \rtimes [(\pi,\pi,\pi,0),\pi] \rtimes A_2^+ \to \begin{cases} (1,1,0) \rtimes [(\pi,0,\pi,\pi),\pi] \rtimes A_1 : \mathcal{O}^{\gamma_5 \otimes \gamma_{i\neq 3}}(1,1,0) \\ (1,1,0) \rtimes [(\pi,\pi,\pi,0),\pi] \rtimes A_2 : \mathcal{O}^{\gamma_5 \otimes \gamma_3}(1,1,0) \end{cases} \tag{C47}$$

$$(0,0,0) \rtimes [(0,0,0,\pi),0] \rtimes A_2^- \to \begin{cases} (1,1,0) \rtimes [(0,0,0,\pi),0] \rtimes A_3 : \mathcal{O}^{\gamma_5 \otimes \gamma_5 \gamma_3}(1,1,0) \\ (1,1,0) \rtimes [(0,0,\pi,0),0] \rtimes A_0 : \mathcal{O}^{\gamma_5 \otimes \gamma_5 \gamma_{i\neq 3}}(1,1,0) \end{cases} \tag{C48}$$

$$(0,0,0) \rtimes [(\pi,0,0,\pi),\pi] \rtimes A_2^+ \to \begin{cases} (1,1,0) \rtimes [(\pi,0,0,\pi),\pi] \rtimes A_2 : \mathcal{O}^{\gamma_5 \otimes \gamma_3 \gamma_0}(1,1,0) \\ (1,1,0) \rtimes [(\pi,0,\pi,0),\pi] \rtimes A_1 : \mathcal{O}^{\gamma_5 \otimes \gamma_{i\neq 3} \gamma_0}(1,1,0) \end{cases} \tag{C49}$$

$$(0,0,0) \rtimes [(0,\pi,\pi,0),\pi] \rtimes A_2^- \to \begin{cases} (1,1,0) \rtimes [(0,0,\pi,\pi),\pi] \rtimes A_0 : \mathcal{O}^{\gamma_5 \otimes \gamma_{i\neq 3} \gamma_3}(1,1,0) \\ (1,1,0) \rtimes [(0,\pi,\pi,0),\pi] \rtimes A_3 : \mathcal{O}^{\gamma_5 \otimes \gamma_{i\neq 3} \gamma_{j\neq 3}}(1,1,0) \end{cases} \tag{C50}$$

The $(1,1,1)$ momentum subduction is given by

$$(0,0,0) \rtimes [(0,0,0,0),0] \rtimes A_0^- \to \Big\{ (1,1,1) \rtimes [(0,0,0,0),0] \rtimes A_1 : \mathcal{O}^{\gamma_5 \otimes 1}(1,1,1) \tag{C51}$$

$$(0,0,0) \rtimes [(\pi,0,0,0),0] \rtimes A_0^+ \to \Big\{ (1,1,1) \rtimes [(\pi,0,0,0),0] \rtimes A_0 : \mathcal{O}^{\gamma_5 \otimes \gamma_5 \gamma_0}(1,1,1) \tag{C52}$$

$$(0,0,0) \rtimes [(0,\pi,\pi,\pi),\pi] \rtimes A_0^- \to \Big\{ (1,1,1) \rtimes [(0,\pi,\pi,\pi),\pi] \rtimes A_1 : \mathcal{O}^{\gamma_5 \otimes \gamma_0}(1,1,1) \tag{C53}$$

$$(0,0,0) \rtimes [(\pi,\pi,\pi,\pi),0] \rtimes A_0^+ \to \Big\{ (1,1,1) \rtimes [(\pi,\pi,\pi,\pi),0] \rtimes A_0 : \mathcal{O}^{\gamma_5 \otimes \gamma_5}(1,1,1) \tag{C54}$$

$$(0,0,0) \rtimes [(\pi,\pi,\pi,0),\pi] \rtimes A_2^+ \to \Big\{ (1,1,1) \rtimes [(\pi,0,\pi,\pi),\pi] \rtimes A_1 : \mathcal{O}^{\gamma_5 \otimes \gamma_i}(1,1,1) \tag{C55}$$

$$(0,0,0) \rtimes [(0,0,0,\pi),0] \rtimes A_2^- \to \Big\{ (1,1,1) \rtimes [(0,0,0,\pi),0] \rtimes A_0 : \mathcal{O}^{\gamma_5 \otimes \gamma_5 \gamma_i}(1,1,1) \tag{C56}$$

$$(0,0,0) \rtimes [(\pi,0,0,\pi),\pi] \rtimes A_2^+ \to \Big\{ (1,1,1) \rtimes [(\pi,0,0,\pi),\pi] \rtimes A_1 : \mathcal{O}^{\gamma_5 \otimes \gamma_i \gamma_0}(1,1,1) \tag{C57}$$

$$(0,0,0) \rtimes [(0,\pi,\pi,0),\pi] \rtimes A_2^- \to \Big\{ (1,1,1) \rtimes [(0,0,\pi,\pi),\pi] \rtimes A_0 : \mathcal{O}^{\gamma_5 \otimes \gamma_i \gamma_j}(1,1,1) \tag{C58}$$

Appendix D: Staggered two-pion Clebsch-Gordan coefficients

In this Appendix, the Clebsch-Gordan coefficents (CGs) for the two cases of staggered two-pion states which couple to the taste-singlet vector current are given. These are two-pion states built out of single pion states, which are either one- or three-dimensional at zero momentum. We only consider the case for momentum $\vec{p}$, $p_i = 0, 1$ i.e the irreps and operators described in Appendix C 2 (see Sec. III C for en explanation of this).

1. One-dimensional pion irreps

These irreps correspond to Eqs. (C27)–(C30). All these cases are equivalent and have the same decomposition as appears with Wilson fermions. We use the pseudo-Goldstone boson pion, Eq. (C30), for illustration. The case for one unit of momentum, $(0,0,1)$, is given in Sec. III A but we give the results again here in Table XVIII, along with the higher momentum CGs, $(1,1,0)$ and $(1,1,1)$ in Tables XIX and XX, respectively.

TABLE XVIII. Clebsch-Gordan table for $(0,0,1) \rtimes [(\pi,\pi,\pi,\pi),0] \rtimes A_0 \otimes (0,0,1) \rtimes [(\pi,\pi,\pi,\pi),\pi] \rtimes A_0 = (0,0,0) \rtimes [(0,0,0,0),\pi] \rtimes T_0^- \oplus \cdots$. The irreps in the rows and columns are labeled by the corresponding operators.

Tensor product row	$\mathcal{O}^{\gamma_1 \otimes 1}(0,0,0)$	$\mathcal{O}^{\gamma_2 \otimes 1}(0,0,0)$	$\mathcal{O}^{\gamma_3 \otimes 1}(0,0,0)$
$\mathcal{O}^{\gamma_5 \otimes \gamma_5}(1,0,0) \otimes \mathcal{O}^{\gamma_5 \otimes \gamma_5}(-1,0,0)$	$\frac{1}{\sqrt{2}}$	0	0
$\mathcal{O}^{\gamma_5 \otimes \gamma_5}(-1,0,0) \otimes \mathcal{O}^{\gamma_5 \otimes \gamma_5}(1,0,0)$	$-\frac{1}{\sqrt{2}}$	0	0
$\mathcal{O}^{\gamma_5 \otimes \gamma_5}(0,1,0) \otimes \mathcal{O}^{\gamma_5 \otimes \gamma_5}(0,-1,0)$	0	$\frac{1}{\sqrt{2}}$	0
$\mathcal{O}^{\gamma_5 \otimes \gamma_5}(0,-1,0) \otimes \mathcal{O}^{\gamma_5 \otimes \gamma_5}(0,1,0)$	0	$-\frac{1}{\sqrt{2}}$	0
$\mathcal{O}^{\gamma_5 \otimes \gamma_5}(0,0,1) \otimes \mathcal{O}^{\gamma_5 \otimes \gamma_5}(0,0,-1)$	0	0	$\frac{1}{\sqrt{2}}$
$\mathcal{O}^{\gamma_5 \otimes \gamma_5}(0,0,-1) \otimes \mathcal{O}^{\gamma_5 \otimes \gamma_5}(0,0,1)$	0	0	$-\frac{1}{\sqrt{2}}$

TABLE XIX. Clebsch-Gordan table for $(1,1,0) \rtimes [(\pi,\pi,\pi,\pi),0] \rtimes A_0 \otimes (1,1,0) \rtimes [(\pi,\pi,\pi,\pi),\pi] \rtimes A_0 = (0,0,0) \rtimes [(0,0,0,0),\pi] \rtimes T_0^- \oplus \cdots$. The irreps in the rows and columns are labeled by the corresponding operators.

Tensor product row	$\mathcal{O}^{\gamma_1 \otimes 1}(0,0,0)$	$\mathcal{O}^{\gamma_2 \otimes 1}(0,0,0)$	$\mathcal{O}^{\gamma_3 \otimes 1}(0,0,0)$
$\mathcal{O}^{\gamma_5 \otimes \gamma_5}(1,1,0) \otimes \mathcal{O}^{\gamma_5 \otimes \gamma_5}(1,1,0)$	$\frac{1}{\sqrt{8}}$	$\frac{1}{\sqrt{8}}$	0
$\mathcal{O}^{\gamma_5 \otimes \gamma_5}(-1,-1,0) \otimes \mathcal{O}^{\gamma_5 \otimes \gamma_5}(-1,-1,0)$	$-\frac{1}{\sqrt{8}}$	$-\frac{1}{\sqrt{8}}$	0
$\mathcal{O}^{\gamma_5 \otimes \gamma_5}(-1,1,0) \otimes \mathcal{O}^{\gamma_5 \otimes \gamma_5}(-1,1,0)$	$-\frac{1}{\sqrt{8}}$	$\frac{1}{\sqrt{8}}$	0
$\mathcal{O}^{\gamma_5 \otimes \gamma_5}(1,-1,0) \otimes \mathcal{O}^{\gamma_5 \otimes \gamma_5}(1,-1,0)$	$\frac{1}{\sqrt{8}}$	$-\frac{1}{\sqrt{8}}$	0
$\mathcal{O}^{\gamma_5 \otimes \gamma_5}(1,0,1) \otimes \mathcal{O}^{\gamma_5 \otimes \gamma_5}(1,0,1)$	$\frac{1}{\sqrt{8}}$	0	$\frac{1}{\sqrt{8}}$
$\mathcal{O}^{\gamma_5 \otimes \gamma_5}(-1,0,-1) \otimes \mathcal{O}^{\gamma_5 \otimes \gamma_5}(-1,0,-1)$	$-\frac{1}{\sqrt{8}}$	0	$-\frac{1}{\sqrt{8}}$
$\mathcal{O}^{\gamma_5 \otimes \gamma_5}(-1,0,1) \otimes \mathcal{O}^{\gamma_5 \otimes \gamma_5}(-1,0,1)$	$-\frac{1}{\sqrt{8}}$	0	$\frac{1}{\sqrt{8}}$
$\mathcal{O}^{\gamma_5 \otimes \gamma_5}(1,0,-1) \otimes \mathcal{O}^{\gamma_5 \otimes \gamma_5}(1,0,-1)$	$\frac{1}{\sqrt{8}}$	0	$-\frac{1}{\sqrt{8}}$
$\mathcal{O}^{\gamma_5 \otimes \gamma_5}(0,1,-1) \otimes \mathcal{O}^{\gamma_5 \otimes \gamma_5}(0,1,-1)$	0	$\frac{1}{\sqrt{8}}$	$-\frac{1}{\sqrt{8}}$
$\mathcal{O}^{\gamma_5 \otimes \gamma_5}(0,-1,1) \otimes \mathcal{O}^{\gamma_5 \otimes \gamma_5}(0,-1,1)$	0	$-\frac{1}{\sqrt{8}}$	$\frac{1}{\sqrt{8}}$
$\mathcal{O}^{\gamma_5 \otimes \gamma_5}(0,1,1) \otimes \mathcal{O}^{\gamma_5 \otimes \gamma_5}(0,1,1)$	0	$\frac{1}{\sqrt{8}}$	$\frac{1}{\sqrt{8}}$
$\mathcal{O}^{\gamma_5 \otimes \gamma_5}(0,-1,-1) \otimes \mathcal{O}^{\gamma_5 \otimes \gamma_5}(0,-1,-1)$	0	$-\frac{1}{\sqrt{8}}$	$-\frac{1}{\sqrt{8}}$

TABLE XX. Clebsch-Gordan table for $(1,1,1) \rtimes [(\pi,\pi,\pi,\pi),0] \rtimes A_0 \otimes (1,1,1) \rtimes [(\pi,\pi,\pi,\pi),\pi] \rtimes A_0 = (0,0,0) \rtimes [(0,0,0,0),\pi] \rtimes T_0^- \oplus \cdots$. The irreps in the rows and columns are labeled by the corresponding operators.

Tensor product row	$\mathcal{O}^{\gamma_1 \otimes 1}(0,0,0)$	$\mathcal{O}^{\gamma_2 \otimes 1}(0,0,0)$	$\mathcal{O}^{\gamma_3 \otimes 1}(0,0,0)$
$\mathcal{O}^{\gamma_5 \otimes \gamma_5}(1,1,1) \otimes \mathcal{O}^{\gamma_5 \otimes \gamma_5}(1,1,1)$	$\frac{1}{\sqrt{8}}$	$\frac{1}{\sqrt{8}}$	$\frac{1}{\sqrt{8}}$
$\mathcal{O}^{\gamma_5 \otimes \gamma_5}(-1,-1,-1) \otimes \mathcal{O}^{\gamma_5 \otimes \gamma_5}(-1,-1,-1)$	$-\frac{1}{\sqrt{8}}$	$-\frac{1}{\sqrt{8}}$	$-\frac{1}{\sqrt{8}}$
$\mathcal{O}^{\gamma_5 \otimes \gamma_5}(-1,1,1) \otimes \mathcal{O}^{\gamma_5 \otimes \gamma_5}(-1,1,1)$	$-\frac{1}{\sqrt{8}}$	$\frac{1}{\sqrt{8}}$	$\frac{1}{\sqrt{8}}$
$\mathcal{O}^{\gamma_5 \otimes \gamma_5}(1,-1,-1) \otimes \mathcal{O}^{\gamma_5 \otimes \gamma_5}(1,-1,-1)$	$\frac{1}{\sqrt{8}}$	$-\frac{1}{\sqrt{8}}$	$-\frac{1}{\sqrt{8}}$
$\mathcal{O}^{\gamma_5 \otimes \gamma_5}(1,-1,1) \otimes \mathcal{O}^{\gamma_5 \otimes \gamma_5}(1,-1,1)$	$\frac{1}{\sqrt{8}}$	$-\frac{1}{\sqrt{8}}$	$\frac{1}{\sqrt{8}}$
$\mathcal{O}^{\gamma_5 \otimes \gamma_5}(-1,1,-1) \otimes \mathcal{O}^{\gamma_5 \otimes \gamma_5}(-1,1,-1)$	$-\frac{1}{\sqrt{8}}$	$\frac{1}{\sqrt{8}}$	$-\frac{1}{\sqrt{8}}$
$\mathcal{O}^{\gamma_5 \otimes \gamma_5}(1,1,-1) \otimes \mathcal{O}^{\gamma_5 \otimes \gamma_5}(1,1,-1)$	$\frac{1}{\sqrt{8}}$	$\frac{1}{\sqrt{8}}$	$-\frac{1}{\sqrt{8}}$
$\mathcal{O}^{\gamma_5 \otimes \gamma_5}(-1,-1,1) \otimes \mathcal{O}^{\gamma_5 \otimes \gamma_5}(-1,-1,1)$	$-\frac{1}{\sqrt{8}}$	$-\frac{1}{\sqrt{8}}$	$\frac{1}{\sqrt{8}}$

2. Three-dimensional pion irreps

For the case of the irreps which are three-dimensional at zero momentum, Eqs. (C31)–(C34), we use the taste-pseudo vector 'one-link' pion as the representative example. Again we start with repeating the results from Sec. III A while including the one-dimensional split irrep here before the higher momentum cases. The $(0,0,1)$ momentum irreps and operators are given in Table XXI for the one-dimensional case and Table XXII for the two-dimensional case. For $(1,1,0)$ momentum, the one- and two-dimensional irrep CGs are given in Tables XXIII and XXIV respectively. Finally at $(1,1,1)$, we have a restoration of the three-dimensional symmetry and hence only set of CGs given in Table XXV. The $(1,1,0)$

TABLE XXI. Clebsch-Gordan table for $(0,0,1) \rtimes [(0,0,0,\pi),0] \rtimes A_0 \otimes (0,0,1) \rtimes [(0,0,0,\pi),\pi] \rtimes A_0 = (0,0,0) \rtimes [(0,0,0,0),\pi] \rtimes T_0^- \oplus \cdots$. The irreps in the rows and columns are labeled by the corresponding operators.

	$\mathcal{O}^{\gamma_1\otimes 1}(0,0,0)$	$\mathcal{O}^{\gamma_2\otimes 1}(0,0,0)$	$\mathcal{O}^{\gamma_3\otimes 1}(0,0,0)$
$\mathcal{O}^{\gamma_5\otimes\gamma_5\gamma_1}(1,0,0) \otimes \mathcal{O}^{\gamma_5\otimes\gamma_5\gamma_1}(-1,0,0)$	$\frac{1}{\sqrt{4}}$	0	0
$\mathcal{O}^{\gamma_5\otimes\gamma_5\gamma_1}(-1,0,0) \otimes \mathcal{O}^{\gamma_5\otimes\gamma_5\gamma_1}(1,0,0)$	$-\frac{1}{\sqrt{4}}$	0	0
$\mathcal{O}^{\gamma_5\otimes\gamma_5\gamma_2}(0,-1,0) \otimes \mathcal{O}^{\gamma_5\otimes\gamma_5\gamma_2}(0,1,0)$	0	$-\frac{1}{\sqrt{4}}$	0
$\mathcal{O}^{\gamma_5\otimes\gamma_5\gamma_2}(0,1,0) \otimes \mathcal{O}^{\gamma_5\otimes\gamma_5\gamma_2}(0,-1,0)$	0	$\frac{1}{\sqrt{4}}$	0
$\mathcal{O}^{\gamma_5\otimes\gamma_5\gamma_3}(0,0,1) \otimes \mathcal{O}^{\gamma_5\otimes\gamma_5\gamma_3}(0,0,-1)$	0	0	$\frac{1}{\sqrt{4}}$
$\mathcal{O}^{\gamma_5\otimes\gamma_5\gamma_3}(0,0,-1) \otimes \mathcal{O}^{\gamma_5\otimes\gamma_5\gamma_3}(0,0,1)$	0	0	$-\frac{1}{\sqrt{4}}$

TABLE XXII. Clebsch-Gordan table for $(0,0,1) \rtimes [(0,0,\pi,0),0] \rtimes A_2 \otimes (0,0,1) \rtimes [(0,0,\pi,0),\pi] \rtimes A_2 = (0,0,0) \rtimes [(0,0,0,0),\pi] \rtimes T_0^- \oplus \cdots$. The irreps in the rows and columns are labeled by the corresponding operators.

Tensor product row	$\mathcal{O}^{\gamma_1\otimes 1}(0,0,0)$	$\mathcal{O}^{\gamma_2\otimes 1}(0,0,0)$	$\mathcal{O}^{\gamma_3\otimes 1}(0,0,0)$
$\mathcal{O}^{\gamma_5\otimes\gamma_5\gamma_2}(1,0,0) \otimes \mathcal{O}^{\gamma_5\otimes\gamma_5\gamma_2}(-1,0,0)$	$\frac{1}{\sqrt{4}}$	0	0
$\mathcal{O}^{\gamma_5\otimes\gamma_5\gamma_3}(1,0,0) \otimes \mathcal{O}^{\gamma_5\otimes\gamma_5\gamma_3}(-1,0,0)$	$\frac{1}{\sqrt{4}}$	0	0
$\mathcal{O}^{\gamma_5\otimes\gamma_5\gamma_2}(-1,0,0) \otimes \mathcal{O}^{\gamma_5\otimes\gamma_5\gamma_2}(1,0,0)$	$-\frac{1}{\sqrt{4}}$	0	0
$\mathcal{O}^{\gamma_5\otimes\gamma_5\gamma_3}(-1,0,0) \otimes \mathcal{O}^{\gamma_5\otimes\gamma_5\gamma_3}(1,0,0)$	$-\frac{1}{\sqrt{4}}$	0	0
$\mathcal{O}^{\gamma_5\otimes\gamma_5\gamma_3}(0,1,0) \otimes \mathcal{O}^{\gamma_5\otimes\gamma_5\gamma_3}(0,-1,0)$	0	$\frac{1}{\sqrt{4}}$	0
$\mathcal{O}^{\gamma_5\otimes\gamma_5\gamma_1}(0,1,0) \otimes \mathcal{O}^{\gamma_5\otimes\gamma_5\gamma_1}(0,-1,0)$	0	$\frac{1}{\sqrt{4}}$	0
$\mathcal{O}^{\gamma_5\otimes\gamma_5\gamma_3}(0,-1,0) \otimes \mathcal{O}^{\gamma_5\otimes\gamma_5\gamma_3}(0,1,0)$	0	$-\frac{1}{\sqrt{4}}$	0
$\mathcal{O}^{\gamma_5\otimes\gamma_5\gamma_1}(0,-1,0) \otimes \mathcal{O}^{\gamma_5\otimes\gamma_5\gamma_1}(0,1,0)$	0	$-\frac{1}{\sqrt{4}}$	0
$\mathcal{O}^{\gamma_5\otimes\gamma_5\gamma_1}(0,0,1) \otimes \mathcal{O}^{\gamma_5\otimes\gamma_5\gamma_1}(0,0,-1)$	0	0	$\frac{1}{\sqrt{4}}$
$\mathcal{O}^{\gamma_5\otimes\gamma_5\gamma_2}(0,0,1) \otimes \mathcal{O}^{\gamma_5\otimes\gamma_5\gamma_2}(0,0,-1)$	0	0	$\frac{1}{\sqrt{4}}$
$\mathcal{O}^{\gamma_5\otimes\gamma_5\gamma_1}(0,0,-1) \otimes \mathcal{O}^{\gamma_5\otimes\gamma_5\gamma_1}(0,0,1)$	0	0	$-\frac{1}{\sqrt{4}}$
$\mathcal{O}^{\gamma_5\otimes\gamma_5\gamma_2}(0,0,-1) \otimes \mathcal{O}^{\gamma_5\otimes\gamma_5\gamma_2}(0,0,1)$	0	0	$-\frac{1}{\sqrt{4}}$

momentum irreps and operators are given in Table XXIII for the one-dimensional case and

Table XXIV for the two-dimensional case . The $(1,1,1)$ momentum irreps and operators

TABLE XXIII. Clebsch-Gordan table for $(1,1,0) \rtimes [(0,0,0,\pi),0] \rtimes A_3 \otimes (1,1,0) \rtimes [(0,0,0,\pi),\pi] \rtimes A_3 = (0,0,0) \rtimes [(0,0,0,0),\pi] \rtimes T_0^- \oplus \cdots$. The irreps in the rows and columns are labeled by the corresponding operators.

Tensor product row	$\mathcal{O}^{\gamma_1 \otimes 1}(0,0,0)$	$\mathcal{O}^{\gamma_2 \otimes 1}(0,0,0)$	$\mathcal{O}^{\gamma_3 \otimes 1}(0,0,0)$
$\mathcal{O}^{\gamma_5 \otimes \gamma_5\gamma_3}(1,1,0) \otimes \mathcal{O}^{\gamma_5 \otimes \gamma_5\gamma_3}(1,1,0)$	$\frac{1}{\sqrt{8}}$	$\frac{1}{\sqrt{8}}$	0
$\mathcal{O}^{\gamma_5 \otimes \gamma_5\gamma_3}(-1,-1,0) \otimes \mathcal{O}^{\gamma_5 \otimes \gamma_5\gamma_3}(-1,-1,0)$	$-\frac{1}{\sqrt{8}}$	$-\frac{1}{\sqrt{8}}$	0
$\mathcal{O}^{\gamma_5 \otimes \gamma_5\gamma_3}(-1,1,0) \otimes \mathcal{O}^{\gamma_5 \otimes \gamma_5\gamma_3}(-1,1,0)$	$-\frac{1}{\sqrt{8}}$	$\frac{1}{\sqrt{8}}$	0
$\mathcal{O}^{\gamma_5 \otimes \gamma_5\gamma_3}(1,-1,0) \otimes \mathcal{O}^{\gamma_5 \otimes \gamma_5\gamma_3}(1,-1,0)$	$\frac{1}{\sqrt{8}}$	$-\frac{1}{\sqrt{8}}$	0
$\mathcal{O}^{\gamma_5 \otimes \gamma_5\gamma_2}(1,0,1) \otimes \mathcal{O}^{\gamma_5 \otimes \gamma_5\gamma_2}(1,0,1)$	$\frac{1}{\sqrt{8}}$	0	$\frac{1}{\sqrt{8}}$
$\mathcal{O}^{\gamma_5 \otimes \gamma_5\gamma_2}(-1,0,-1) \otimes \mathcal{O}^{\gamma_5 \otimes \gamma_5\gamma_2}(-1,0,-1)$	$-\frac{1}{\sqrt{8}}$	0	$-\frac{1}{\sqrt{8}}$
$\mathcal{O}^{\gamma_5 \otimes \gamma_5\gamma_2}(-1,0,1) \otimes \mathcal{O}^{\gamma_5 \otimes \gamma_5\gamma_2}(-1,0,1)$	$-\frac{1}{\sqrt{8}}$	0	$\frac{1}{\sqrt{8}}$
$\mathcal{O}^{\gamma_5 \otimes \gamma_5\gamma_2}(1,0,-1) \otimes \mathcal{O}^{\gamma_5 \otimes \gamma_5\gamma_2}(1,0,-1)$	$\frac{1}{\sqrt{8}}$	0	$-\frac{1}{\sqrt{8}}$
$\mathcal{O}^{\gamma_5 \otimes \gamma_5\gamma_1}(0,1,-1) \otimes \mathcal{O}^{\gamma_5 \otimes \gamma_5\gamma_1}(0,1,-1)$	0	$\frac{1}{\sqrt{8}}$	$-\frac{1}{\sqrt{8}}$
$\mathcal{O}^{\gamma_5 \otimes \gamma_5\gamma_1}(0,-1,1) \otimes \mathcal{O}^{\gamma_5 \otimes \gamma_5\gamma_1}(0,-1,1)$	0	$-\frac{1}{\sqrt{8}}$	$\frac{1}{\sqrt{8}}$
$\mathcal{O}^{\gamma_5 \otimes \gamma_5\gamma_1}(0,1,1) \otimes \mathcal{O}^{\gamma_5 \otimes \gamma_5\gamma_1}(0,1,1)$	0	$\frac{1}{\sqrt{8}}$	$\frac{1}{\sqrt{8}}$
$\mathcal{O}^{\gamma_5 \otimes \gamma_5\gamma_1}(0,-1,-1) \otimes \mathcal{O}^{\gamma_5 \otimes \gamma_5\gamma_1}(0,-1,-1)$	0	$-\frac{1}{\sqrt{8}}$	$-\frac{1}{\sqrt{8}}$

are given in Table XXV for the three-dimensional case.

TABLE XXIV. Clebsch-Gordan table for $(1,1,0) \rtimes [(0,0,\pi,0),0] \rtimes A_0 \otimes (1,1,0) \rtimes [(0,0,\pi,0),\pi] \rtimes A_0 = (0,0,0) \rtimes [(0,0,0,0),\pi] \rtimes T_0^- \oplus \cdots$. The irreps in the rows and columns are labeled by the corresponding operators.

Tensor product row	$\mathcal{O}^{\gamma_1 \otimes 1}(0,0,0)$	$\mathcal{O}^{\gamma_2 \otimes 1}(0,0,0)$	$\mathcal{O}^{\gamma_3 \otimes 1}(0,0,0)$
$\mathcal{O}^{\gamma_5 \otimes \gamma_5 \gamma_1}(1,1,0) \otimes \mathcal{O}^{\gamma_5 \otimes \gamma_5 \gamma_1}(-1,-1,0)$	$\frac{1}{4}$	$\frac{1}{4}$	0
$\mathcal{O}^{\gamma_5 \otimes \gamma_5 \gamma_2}(1,1,0) \otimes \mathcal{O}^{\gamma_5 \otimes \gamma_5 \gamma_2}(-1,-1,0)$	$\frac{1}{4}$	$\frac{1}{4}$	0
$\mathcal{O}^{\gamma_5 \otimes \gamma_5 \gamma_1}(-1,-1,0) \otimes \mathcal{O}^{\gamma_5 \otimes \gamma_5 \gamma_1}(1,1,0)$	$-\frac{1}{4}$	$-\frac{1}{4}$	0
$\mathcal{O}^{\gamma_5 \otimes \gamma_5 \gamma_2}(-1,-1,0) \otimes \mathcal{O}^{\gamma_5 \otimes \gamma_5 \gamma_2}(1,1,0)$	$-\frac{1}{4}$	$-\frac{1}{4}$	0
$\mathcal{O}^{\gamma_5 \otimes \gamma_5 \gamma_1}(-1,1,0) \otimes \mathcal{O}^{\gamma_5 \otimes \gamma_5 \gamma_1}(1,-1,0)$	$-\frac{1}{4}$	$\frac{1}{4}$	0
$\mathcal{O}^{\gamma_5 \otimes \gamma_5 \gamma_2}(-1,1,0) \otimes \mathcal{O}^{\gamma_5 \otimes \gamma_5 \gamma_2}(1,-1,0)$	$-\frac{1}{4}$	$\frac{1}{4}$	0
$\mathcal{O}^{\gamma_5 \otimes \gamma_5 \gamma_1}(1,-1,0) \otimes \mathcal{O}^{\gamma_5 \otimes \gamma_5 \gamma_1}(-1,1,0)$	$\frac{1}{4}$	$-\frac{1}{4}$	0
$\mathcal{O}^{\gamma_5 \otimes \gamma_5 \gamma_2}(1,-1,0) \otimes \mathcal{O}^{\gamma_5 \otimes \gamma_5 \gamma_2}(-1,1,0)$	$\frac{1}{4}$	$-\frac{1}{4}$	0
$\mathcal{O}^{\gamma_5 \otimes \gamma_5 \gamma_2}(1,0,1) \otimes \mathcal{O}^{\gamma_5 \otimes \gamma_5 \gamma_2}(-1,0,-1)$	$\frac{1}{4}$	0	$\frac{1}{4}$
$\mathcal{O}^{\gamma_5 \otimes \gamma_5 \gamma_3}(1,0,1) \otimes \mathcal{O}^{\gamma_5 \otimes \gamma_5 \gamma_3}(-1,0,-1)$	$\frac{1}{4}$	0	$\frac{1}{4}$
$\mathcal{O}^{\gamma_5 \otimes \gamma_5 \gamma_2}(-1,0,-1) \otimes \mathcal{O}^{\gamma_5 \otimes \gamma_5 \gamma_2}(1,0,1)$	$-\frac{1}{4}$	0	$-\frac{1}{4}$
$\mathcal{O}^{\gamma_5 \otimes \gamma_5 \gamma_3}(-1,0,-1) \otimes \mathcal{O}^{\gamma_5 \otimes \gamma_5 \gamma_3}(1,0,1)$	$-\frac{1}{4}$	0	$-\frac{1}{4}$
$\mathcal{O}^{\gamma_5 \otimes \gamma_5 \gamma_2}(-1,0,1) \otimes \mathcal{O}^{\gamma_5 \otimes \gamma_5 \gamma_2}(1,0,-1)$	$-\frac{1}{4}$	0	$\frac{1}{4}$
$\mathcal{O}^{\gamma_5 \otimes \gamma_5 \gamma_3}(-1,0,1) \otimes \mathcal{O}^{\gamma_5 \otimes \gamma_5 \gamma_3}(1,0,-1)$	$-\frac{1}{4}$	0	$\frac{1}{4}$
$\mathcal{O}^{\gamma_5 \otimes \gamma_5 \gamma_2}(1,0,-1) \otimes \mathcal{O}^{\gamma_5 \otimes \gamma_5 \gamma_2}(-1,0,1)$	$\frac{1}{4}$	0	$-\frac{1}{4}$
$\mathcal{O}^{\gamma_5 \otimes \gamma_5 \gamma_3}(1,0,-1) \otimes \mathcal{O}^{\gamma_5 \otimes \gamma_5 \gamma_3}(-1,0,1)$	$\frac{1}{4}$	0	$-\frac{1}{4}$
$\mathcal{O}^{\gamma_5 \otimes \gamma_5 \gamma_3}(0,1,1) \otimes \mathcal{O}^{\gamma_5 \otimes \gamma_5 \gamma_3}(0,-1,-1)$	0	$\frac{1}{4}$	$\frac{1}{4}$
$\mathcal{O}^{\gamma_5 \otimes \gamma_5 \gamma_1}(0,1,1) \otimes \mathcal{O}^{\gamma_5 \otimes \gamma_5 \gamma_1}(0,-1,-1)$	0	$\frac{1}{4}$	$\frac{1}{4}$
$\mathcal{O}^{\gamma_5 \otimes \gamma_5 \gamma_3}(0,-1,-1) \otimes \mathcal{O}^{\gamma_5 \otimes \gamma_5 \gamma_3}(0,1,1)$	0	$-\frac{1}{4}$	$-\frac{1}{4}$
$\mathcal{O}^{\gamma_5 \otimes \gamma_5 \gamma_1}(0,-1,-1) \otimes \mathcal{O}^{\gamma_5 \otimes \gamma_5 \gamma_1}(0,1,1)$	0	$-\frac{1}{4}$	$-\frac{1}{4}$
$\mathcal{O}^{\gamma_5 \otimes \gamma_5 \gamma_3}(0,1,-1) \otimes \mathcal{O}^{\gamma_5 \otimes \gamma_5 \gamma_3}(0,-1,1)$	0	$\frac{1}{4}$	$-\frac{1}{4}$
$\mathcal{O}^{\gamma_5 \otimes \gamma_5 \gamma_1}(0,1,-1) \otimes \mathcal{O}^{\gamma_5 \otimes \gamma_5 \gamma_1}(0,-1,1)$	0	$\frac{1}{4}$	$-\frac{1}{4}$
$\mathcal{O}^{\gamma_5 \otimes \gamma_5 \gamma_3}(0,-1,1) \otimes \mathcal{O}^{\gamma_5 \otimes \gamma_5 \gamma_3}(0,1,-1)$	0	$-\frac{1}{4}$	$\frac{1}{4}$
$\mathcal{O}^{\gamma_5 \otimes \gamma_5 \gamma_1}(0,-1,1) \otimes \mathcal{O}^{\gamma_5 \otimes \gamma_5 \gamma_1}(0,1,-1)$	0	$-\frac{1}{4}$	$\frac{1}{4}$

TABLE XXV. Clebsch-Gordan table for $(1,1,1) \rtimes [(0,0,0,\pi),0] \rtimes A_0 \otimes (1,1,1) \rtimes [(0,0,0,\pi),\pi] \rtimes A_0 = (0,0,0) \rtimes [(0,0,0,0),\pi] \rtimes T_0^- \oplus \cdots$. The irreps in the rows and columns are labeled by the corresponding operators.

Tensor product row	$\mathcal{O}^{\gamma_1 \otimes 1}(0,0,0)$	$\mathcal{O}^{\gamma_2 \otimes 1}(0,0,0)$	$\mathcal{O}^{\gamma_3 \otimes 1}(0,0,0)$
$\mathcal{O}^{\gamma_5 \otimes \gamma_5 \gamma_1}(1,1,1) \otimes \mathcal{O}^{\gamma_5 \otimes \gamma_5 \gamma_1}(-1,-1,-1)$	$\frac{1}{4}$	$\frac{1}{4\sqrt{2}}$	$\frac{1}{4\sqrt{2}}$
$\mathcal{O}^{\gamma_5 \otimes \gamma_5 \gamma_2}(1,1,1) \otimes \mathcal{O}^{\gamma_5 \otimes \gamma_5 \gamma_2}(-1,-1,-1)$	$\frac{1}{4\sqrt{2}}$	$\frac{1}{4}$	$\frac{1}{4\sqrt{2}}$
$\mathcal{O}^{\gamma_5 \otimes \gamma_5 \gamma_3}(1,1,1) \otimes \mathcal{O}^{\gamma_5 \otimes \gamma_5 \gamma_3}(-1,-1,-1)$	$\frac{1}{4\sqrt{2}}$	$\frac{1}{4\sqrt{2}}$	$\frac{1}{4}$
$\mathcal{O}^{\gamma_5 \otimes \gamma_5 \gamma^1}(-1,-1,-1) \otimes \mathcal{O}^{\gamma_5 \otimes \gamma_5 \gamma_1}(1,1,1)$	$-\frac{1}{4}$	$-\frac{1}{4\sqrt{2}}$	$-\frac{1}{4\sqrt{2}}$
$\mathcal{O}^{\gamma_5 \otimes \gamma_5 \gamma_2}(-1,-1,-1) \otimes \mathcal{O}^{\gamma_5 \otimes \gamma_5 \gamma_2}(1,1,1)$	$-\frac{1}{4\sqrt{2}}$	$-\frac{1}{4}$	$-\frac{1}{4\sqrt{2}}$
$\mathcal{O}^{\gamma_5 \otimes \gamma_5 \gamma_3}(-1,-1,-1) \otimes \mathcal{O}^{\gamma_5 \otimes \gamma_5 \gamma_3}(1,1,1)$	$-\frac{1}{4\sqrt{2}}$	$-\frac{1}{4\sqrt{2}}$	$-\frac{1}{4}$
$\mathcal{O}^{\gamma_5 \otimes \gamma_5 \gamma_1}(-1,1,1) \otimes \mathcal{O}^{\gamma_5 \otimes \gamma_5 \gamma_1}(1,-1,-1)$	$-\frac{1}{4}$	$\frac{1}{4\sqrt{2}}$	$\frac{1}{4\sqrt{2}}$
$\mathcal{O}^{\gamma_5 \otimes \gamma_5 \gamma_2}(-1,1,1) \otimes \mathcal{O}^{\gamma_5 \otimes \gamma_5 \gamma_2}(1,-1,-1)$	$-\frac{1}{4\sqrt{2}}$	$\frac{1}{4}$	$\frac{1}{4\sqrt{2}}$
$\mathcal{O}^{\gamma_5 \otimes \gamma_5 \gamma_3}(-1,1,1) \otimes \mathcal{O}^{\gamma_5 \otimes \gamma_5 \gamma_3}(1,-1,-1)$	$-\frac{1}{4\sqrt{2}}$	$\frac{1}{4\sqrt{2}}$	$\frac{1}{4}$
$\mathcal{O}^{\gamma_5 \otimes \gamma_5 \gamma_1}(1,-1,-1) \otimes \mathcal{O}^{\gamma_5 \otimes \gamma_5 \gamma_1}(-1,1,1)$	$\frac{1}{4}$	$-\frac{1}{4\sqrt{2}}$	$-\frac{1}{4\sqrt{2}}$
$\mathcal{O}^{\gamma_5 \otimes \gamma_5 \gamma_2}(1,-1,-1) \otimes \mathcal{O}^{\gamma_5 \otimes \gamma_5 \gamma_2}(-1,1,1)$	$\frac{1}{4\sqrt{2}}$	$-\frac{1}{4}$	$-\frac{1}{4\sqrt{2}}$
$\mathcal{O}^{\gamma_5 \otimes \gamma_5 \gamma_3}(1,-1,-1) \otimes \mathcal{O}^{\gamma_5 \otimes \gamma_5 \gamma_3}(-1,1,1)$	$\frac{1}{4\sqrt{2}}$	$-\frac{1}{4\sqrt{2}}$	$-\frac{1}{4}$
$\mathcal{O}^{\gamma_5 \otimes \gamma_5 \gamma_1}(1,-1,1) \otimes \mathcal{O}^{\gamma_5 \otimes \gamma_5 \gamma_1}(-1,1,-1)$	$\frac{1}{4}$	$-\frac{1}{4\sqrt{2}}$	$\frac{1}{4\sqrt{2}}$
$\mathcal{O}^{\gamma_5 \otimes \gamma_5 \gamma_2}(1,-1,1) \otimes \mathcal{O}^{\gamma_5 \otimes \gamma_5 \gamma_2}(-1,1,-1)$	$\frac{1}{4\sqrt{2}}$	$-\frac{1}{4}$	$\frac{1}{4\sqrt{2}}$
$\mathcal{O}^{\gamma_5 \otimes \gamma_5 \gamma_3}(1,-1,1) \otimes \mathcal{O}^{\gamma_5 \otimes \gamma_5 \gamma_3}(-1,1,-1)$	$\frac{1}{4\sqrt{2}}$	$-\frac{1}{4\sqrt{2}}$	$\frac{1}{4}$
$\mathcal{O}^{\gamma_5 \otimes \gamma_5 \gamma_1}(-1,1,-1) \otimes \mathcal{O}^{\gamma_5 \otimes \gamma_5 \gamma_1}(1,-1,1)$	$-\frac{1}{4}$	$\frac{1}{4\sqrt{2}}$	$-\frac{1}{4\sqrt{2}}$
$\mathcal{O}^{\gamma_5 \otimes \gamma_5 \gamma_2}(-1,1,-1) \otimes \mathcal{O}^{\gamma_5 \otimes \gamma_5 \gamma_2}(1,-1,1)$	$-\frac{1}{4\sqrt{2}}$	$\frac{1}{4}$	$-\frac{1}{4\sqrt{2}}$
$\mathcal{O}^{\gamma_5 \otimes \gamma_5 \gamma_3}(-1,1,-1) \otimes \mathcal{O}^{\gamma_5 \otimes \gamma_5 \gamma_3}(1,-1,1)$	$-\frac{1}{4\sqrt{2}}$	$\frac{1}{4\sqrt{2}}$	$-\frac{1}{4}$
$\mathcal{O}^{\gamma_5 \otimes \gamma_5 \gamma_1}(1,1,-1) \otimes \mathcal{O}^{\gamma_5 \otimes \gamma_5 \gamma_1}(-1,-1,1)$	$\frac{1}{4}$	$\frac{1}{4\sqrt{2}}$	$-\frac{1}{4\sqrt{2}}$
$\mathcal{O}^{\gamma_5 \otimes \gamma_5 \gamma_2}(1,1,-1) \otimes \mathcal{O}^{\gamma_5 \otimes \gamma_5 \gamma_2}(-1,-1,1)$	$\frac{1}{4\sqrt{2}}$	$\frac{1}{4}$	$-\frac{1}{4\sqrt{2}}$
$\mathcal{O}^{\gamma_5 \otimes \gamma_5 \gamma_3}(1,1,-1) \otimes \mathcal{O}^{\gamma_5 \otimes \gamma_5 \gamma_3}(-1,-1,1)$	$\frac{1}{4\sqrt{2}}$	$\frac{1}{4\sqrt{2}}$	$-\frac{1}{4}$
$\mathcal{O}^{\gamma_5 \otimes \gamma_5 \gamma_1}(-1,-1,1) \otimes \mathcal{O}^{\gamma_5 \otimes \gamma_5 \gamma_1}(1,1,-1)$	$-\frac{1}{4}$	$-\frac{1}{4\sqrt{2}}$	$\frac{1}{4\sqrt{2}}$
$\mathcal{O}^{\gamma_5 \otimes \gamma_5 \gamma_2}(-1,-1,1) \otimes \mathcal{O}^{\gamma_5 \otimes \gamma_5 \gamma_2}(1,1,-1)$	$-\frac{1}{4\sqrt{2}}$	$-\frac{1}{4}$	$\frac{1}{4\sqrt{2}}$
$\mathcal{O}^{\gamma_5 \otimes \gamma_5 \gamma_3}(-1,-1,1) \otimes \mathcal{O}^{\gamma_5 \otimes \gamma_5 \gamma_3}(1,1,-1)$	$-\frac{1}{4\sqrt{2}}$	$-\frac{1}{4\sqrt{2}}$	$\frac{1}{4}$

Appendix E: Rooting and staggered observables

In quantum field theory, observables can be obtained through taking functional derivatives of a generating functional. For the case of staggered fermions, the fermion determinant, $\det D_f[U]$, describes four tastes of staggered fermions for each flavor. This is addressed by taking the fourth root of the fermion determinant. The rooted-staggered path integral is then

$$Z = \int \mathcal{D}[U] \prod_f [\det D_f[U]]^{\frac{1}{4}} \, \mathrm{e}^{-S_G}. \tag{E1}$$

Rooting results in additional factors of $\frac{1}{4}$ that need to be included when computing physical observables. As illustration, we obtain the vector current two-point correlation function using the staggered action, Eq. (A6). Coupling to a background photon field $C^\mu(n)$, we have,

$$S_F\left[\chi_f, \bar{\chi}_f, U, C\right] = a^4 \sum_f \sum_{n,m\in\Lambda} \bar{\chi}_f(n) D_f[U,C](n|m) \chi_f(m), \tag{E2}$$

$$D_f[U,C](n|m) = \sum_\mu \eta_\mu(n) \left[\frac{U_\mu(n) e^{iaQ_f C_\mu(n)} \delta_{m,n+\hat{\mu}}}{2a} - \text{H.c.} \right] + m\, \delta_{n,m}, \tag{E3}$$

where H.c.is the Hermitian conjugate. The generating functional is

$$Z[C] = \int \mathcal{D}[U] \prod_f \det D_f[U,C] \, \mathrm{e}^{-S_G}. \tag{E4}$$

The vector current two-point function is obtained by taking the second derivative with respect to the source field, giving

$$\left.\frac{\delta^2 \log Z[C]}{\delta C_\mu(x) \delta C_\mu(x')}\right|_{C=0} = \left.\frac{1}{Z[C(x')]} \frac{\delta^2 Z[C]}{\delta C_\mu(x) \delta C_\mu(x')}\right|_{C=0} - \left.\frac{1}{Z^2[C(x')]} \frac{\delta Z[C]}{\delta C_\mu(x)}\right|_{C=0} \tag{E5}$$

The second term on the right-hand side is zero by the lattice rotation-reflection symmetries. Then using

$$\det M = \exp \operatorname{tr} \log M, \tag{E6}$$

first without rooting, gives

$$\begin{aligned} \frac{1}{Z[C(x')]} \frac{\delta^2 Z[C]}{\delta C_\mu(x) \delta C_\mu(x')} = \frac{1}{Z[C(x')]} \frac{\delta}{\delta C_\mu(x)} \int \mathcal{D}[U] \mathrm{e}^{-S_G} \prod_f \det D_f[U,C] \\ \times \operatorname{tr} \left[\sum_f D_f^{-1}[U,C](x')\, iQ_f \eta_\mu(x') \left[\frac{U_\mu(x') e^{iaQ_f C_\mu(x')} \delta_{m,x'+\hat{\mu}}}{2} - \text{h.c.} \right] \right] \end{aligned} \tag{E7}$$

Taking the second derivative and setting $C = 0$ gives

$$= \int \mathcal{D}[U] \mathrm{e}^{-S_G} \prod_f \det D_f[U,C] \left\{ \operatorname{tr}\Big[\sum_f D_f^{-1}[U,C](x)\, Q_f j^\mu(x) D_f^{-1}[U,C](x')\, Q_f j^\mu(x') \Big] \right.$$

$$- \operatorname{tr}\Big[\sum_{f'} D_{f'}^{-1}[U,C](x)\, Q'_f j^\mu(x)\Big] \times \operatorname{tr}\Big[\sum_{f} D_{f}^{-1}[U,C](x')\, Q_f j^\mu(x')\Big]\Bigg\} \tag{E8}$$

where the lattice current operator, $j^\mu(x)$, was introduced

$$J^\mu(x) \equiv \frac{1}{2}\left[\eta_\mu(x) U_\mu(x) \delta_{m,x+\hat{\mu}} - \text{h.c.}\right] \tag{E9}$$

The trace on the first line Eq. (E8) is the 'connected' Wick contraction while the product of the two traces on the second line is the 'disconnected' contraction, corresponding to the following two diagrams,

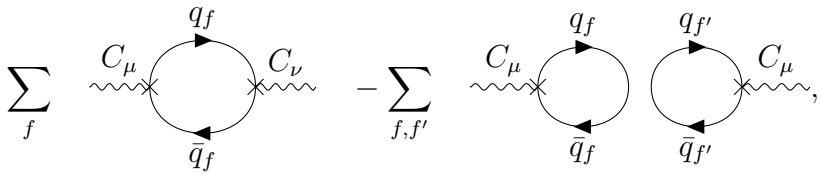

(E10)

where the $\times$ implies the background fields are set to zero as above. The effect of the 4 tastes is to add three additional quark loops for each flavor.

Re-computing Eq. (E8) for the case of a rooted determinant results in

$$= \int \mathcal{D}[U] \mathrm{e}^{-S_G} \prod_f \left[\det D_f[U,C]\right]^{\frac{1}{4}} \Bigg\{ \frac{1}{4} \operatorname{tr}\Big[\sum_f D_f^{-1}[U,C](x)\, Q_f J^\mu(x) D_f^{-1}[U,C](x')\, Q_f J^\mu(x')\Big]$$
$$- \frac{1}{16} \operatorname{tr}\Big[\sum_{f'} D_{f'}^{-1}[U,C](x)\, Q'_f J^\mu(x)\Big] \times \operatorname{tr}\Big[\sum_f D_f^{-1}[U,C](x')\, Q_f J^\mu(x')\Big]\Bigg\}. \tag{E11}$$

There is now a factor of $\frac{1}{4}$ in the connected component and a factor of $\frac{1}{16}$ in the disconnected component. From this and Eq. (E10), one can infer the diagrammatic rule that for every fermion loop in a staggered Wick contraction, a factor of $\frac{1}{4}$ is added to obtain the corresponding physical observable.

Appendix F: Time-split two-pion operators

1. Operator definitions

As mentioned in Sec. III B, the correlation functions used in this work are generated with time-split two-pion operators. This modification, introduced in Ref. [54] to address possible Fierz rearrangement of pions on the same time slice, is not actually necessary with the random-wall sources used here.[17] Here, for completeness, we describe the additional considerations these operators require.

[17] This was not realized at the time of data generation.

The time-split operators, which are non-Hermitian to start with, are defined as

$$\mathcal{O}^{\mathrm{TS}}_{\pi\pi}(\vec{0},t) \equiv \pi^{+}_{\otimes\gamma_\xi}(p,t)\pi^{-}_{\otimes\gamma_\xi}(-p,t+1) - \pi^{+}_{\otimes\gamma_\xi}(-p,t)\pi^{-}_{\otimes\gamma_\xi}(p,t+1), \tag{F1}$$

$$\mathcal{O}^{\mathrm{TS}\,\dagger}_{\pi\pi}(\vec{0},t) \equiv \pi^{+}_{\otimes\gamma_\xi}(p,t+1)\pi^{-}_{\otimes\gamma_\xi}(-p,t) - \pi^{+}_{\otimes\gamma_\xi}(-p,t+1)\pi^{-}(p,t), \tag{F2}$$

using the notation of Secs. III A and III B on the right-hand side. To make apparent the effects of these operators on the correlation functions described in Sec. III B, it is useful to pull out the time dependence,

$$\mathcal{O}^{\mathrm{TS}}_{\pi\pi}(\vec{0},t) \equiv e^{Ht}\mathcal{O}_{\pi\pi}(\vec{0})e^{-H(t+1)}, \tag{F3}$$

$$\mathcal{O}^{\mathrm{TS}\,\dagger}_{\pi\pi}(\vec{0},t) \equiv e^{H(t+1)}\mathcal{O}_{\pi\pi}(\vec{0})e^{-Ht}, \tag{F4}$$

with

$$\mathcal{O}_{\pi\pi}(\vec{0}_{\vec{p}}) = \pi^{+}(\vec{p})\pi^{-}(-\vec{p}) - \pi^{+}(-\vec{p})\pi^{-}(\vec{p}), \tag{F5}$$

now Hermitian.

2. Correlation functions

The two-point function, Eq. (2.10), is unchanged. The $C(t)_{\pi\pi\to\rho}$ three-point function, Eq. (3.27), is modified as

$$C(t)_{\pi\pi\to\rho} = \frac{1}{3}\sum_i \left\langle \rho^0_i(\vec{0},t)\mathcal{O}^{\mathrm{TS}\,\dagger}_{\pi\pi}(\vec{0}_{\vec{p}},0)\right\rangle = \sum_n \langle 0|\rho^0|n\rangle\langle n|\mathcal{O}^{\otimes\gamma_\xi}_{\pi\pi}|0\rangle e^{-E_n(t-1)}$$

$$= 4\cdot\frac{1}{2}\cdot\frac{1}{4}\cdot\frac{1}{N_S^{9/2}}\cdot\frac{1}{3}\times\sum_i$$

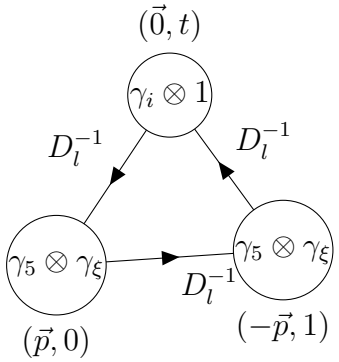

, (F6)

$$= \frac{1}{6N_S^{9/2}}\sum_{i,\vec{n}_0,\vec{n}_1,\vec{n}_2,\{\pm\delta_j\}} \varphi^{\gamma_5\otimes\gamma_\xi}(n_0)\varphi^{\gamma_5\otimes\gamma_\xi}(n_1)\varphi^{\gamma_i\otimes 1}(n_2)e^{i\vec{p}\cdot(\vec{n}_0-\vec{n}_1)}$$

$$\times\,\mathrm{tr}\left[D_l^{-1}(\vec{n}_0+\delta^{\gamma_5\otimes\gamma_\xi},0|\vec{n}_1,1)D_l^{-1}(\vec{n}_1+\delta^{\gamma_5\otimes\gamma_\xi},1|\vec{n}_2,t)D_l^{-1}(\vec{n}_2+\delta^{\gamma_i\otimes 1},t|\vec{n}_0,0)\right]. \tag{F7}$$

with the same normalizations defined in Sec. III B 2. The $\pi\pi\to\pi\pi$ four point function becomes

$$C(t)_{\pi\pi\to\pi\pi} = \left\langle \mathcal{O}^{\mathrm{TS}}_{\pi\pi}(\vec{0}_{\vec{p}},t)\mathcal{O}^{\mathrm{TS}\,\dagger}_{\pi\pi}(\vec{0}_{\vec{p}},0)\right\rangle = \sum_n \langle 0|\mathcal{O}^{\mathrm{TS},\otimes\gamma_{\xi_1}}_{\pi\pi}|n\rangle\langle n|\mathcal{O}^{\mathrm{TS},\otimes\gamma_{\xi_2}}_{\pi\pi}|0\rangle e^{-E_n t}$$

$$= -4 \cdot \frac{1}{4} \cdot \frac{1}{N_S^6} \times$$

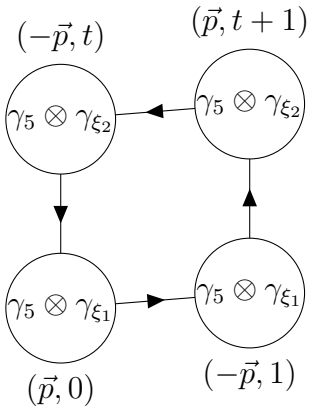

$$+ 4 \cdot \frac{1}{4} \cdot \frac{1}{N_S^6} \times$$

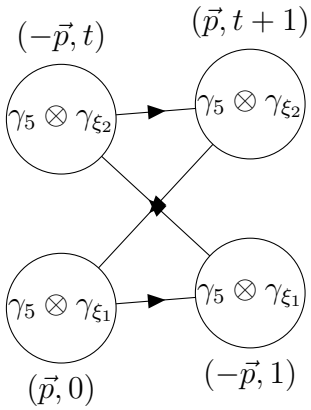

$$+ 2 \cdot \frac{1}{16} \cdot \frac{1}{N_S^6} \times$$

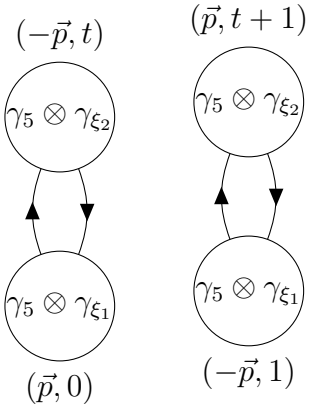

$$- 2 \cdot \frac{1}{16} \cdot \frac{1}{N_S^6} \times$$

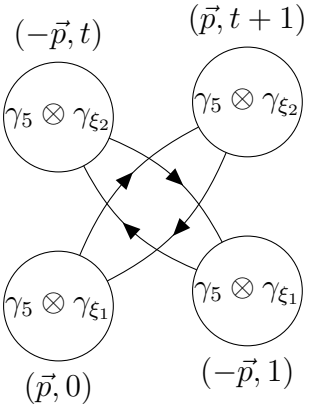

, (F8)

$$= \frac{1}{N_S^6} \sum_{\vec{n}_0, \vec{n}_1, \vec{n}_2, \vec{n}_3, \{\pm\delta_j\}} \varphi^{\gamma_5 \otimes \gamma_{\xi_1}}(n_0) \varphi^{\gamma_5 \otimes \gamma_{\xi_1}}(n_1) \varphi^{\gamma_5 \otimes \gamma_{\xi_2}}(n_2) \varphi^{\gamma_5 \otimes \gamma_{\xi_2}}(n_3) e^{i\vec{p} \cdot (\vec{n}_0 - \vec{n}_1 + \vec{n}_2 - \vec{n}_3)} \Big[$$

$$\begin{aligned}
&- \mathrm{tr}\left[D_l^{-1}(\vec{n}_0 + \delta^{\gamma_5 \otimes \gamma_{\xi_1}}, 0 | \vec{n}_1, 1) D_l^{-1}(\vec{n}_1 + \delta^{\gamma_5 \otimes \gamma_{\xi_1}}, 1 | \vec{n}_2, t) \right. \\
&\qquad \left. \times D_l^{-1}(\vec{n}_2 + \delta^{\gamma_5 \otimes \gamma_{\xi_2}}, t | \vec{n}_3, t+1) D_l^{-1}(\vec{n}_3 + \delta^{\gamma_5 \otimes \gamma_{\xi_2}}, t+1 | \vec{n}_0, 0) \right] \\
&+ \mathrm{tr}\left[D_l^{-1}(\vec{n}_0 + \delta^{\gamma_5 \otimes \gamma_{\xi_1}}, 0 | \vec{n}_1, 1) D_l^{-1}(\vec{n}_1 + \delta^{\gamma_5 \otimes \gamma_{\xi_1}}, 1 | \vec{n}_3, t+1) \right. \\
&\qquad \left. \times D_l^{-1}(\vec{n}_3 + \delta^{\gamma_5 \otimes \gamma_{\xi_2}}, t+1 | \vec{n}_2, t) D_l^{-1}(\vec{n}_2 + \delta^{\gamma_5 \otimes \gamma_{\xi_2}}, t | \vec{n}_0, 0) \right] \\
&+ \frac{1}{8} \mathrm{tr}\left[D_l^{-1}(\vec{n}_0 + \delta^{\gamma_5 \otimes \gamma_{\xi_1}}, 0 | \vec{n}_2, t) D_l^{-1}(\vec{n}_2 + \delta^{\gamma_5 \otimes \gamma_{\xi_2}}, t | \vec{n}_0, 0) \right] \\
&\qquad \times \mathrm{tr}\left[D_l^{-1}(\vec{n}_1 + \delta^{\gamma_5 \otimes \gamma_{\xi_1}}, 1 | \vec{n}_3, t+1) D_l^{-1}(\vec{n}_3 + \delta^{\gamma_5 \otimes \gamma_{\xi_2}}, t+1 | \vec{n}_1, 1) \right] \\
&- \frac{1}{8} \mathrm{tr}\left[D_l^{-1}(\vec{n}_0 + \delta^{\gamma_5 \otimes \gamma_{\xi_1}}, 0 | \vec{n}_3, t+1) D_l^{-1}(\vec{n}_3 + \delta^{\gamma_5 \otimes \gamma_{\xi_2}}, t+1 | \vec{n}_0, 0) \right] \\
&\qquad \times \mathrm{tr}\left[D_l^{-1}(\vec{n}_1 + \delta^{\gamma_5 \otimes \gamma_{\xi_1}}, 1 | \vec{n}_2, t) D_l^{-1}(\vec{n}_2 + \delta^{\gamma_5 \otimes \gamma_{\xi_2}}, t | \vec{n}_1, 1) \right] \Big]. \qquad \text{(F9)}
\end{aligned}$$

[1] D. P. Aguillard *et al.* (Muon g-2), Phys. Rev. Lett. **131**, 161802 (2023), arXiv:2308.06230 [hep-ex].

[2] B. Abi *et al.* (Muon $g-2$), Phys. Rev. Lett. **126**, 141801 (2021).

[3] G. W. Bennett *et al.* (Muon g-2), Phys. Rev. D **73**, 072003 (2006), arXiv:hep-ex/0602035.

[4] T. Aoyama *et al.*, Phys. Rept. **887**, 1 (2020), arXiv:2006.04822 [hep-ph].

[5] T. Aoyama, M. Hayakawa, T. Kinoshita, and M. Nio, Phys. Rev. Lett. **109**, 111808 (2012).
[6] T. Aoyama, T. Kinoshita, and M. Nio, Atoms **7**, 28 (2019).
[7] A. Czarnecki, W. J. Marciano, and A. Vainshtein, Phys. Rev. **D67**, 073006 (2003), [Erratum: Phys. Rev. **D73**, 119901 (2006)].
[8] C. Gnendiger, D. Stöckinger, and H. Stöckinger-Kim, Phys. Rev. **D88**, 053005 (2013).
[9] M. Davier, A. Hoecker, B. Malaescu, and Z. Zhang, Eur. Phys. J. C **77**, 827 (2017), arXiv:1706.09436 [hep-ph].
[10] A. Keshavarzi, D. Nomura, and T. Teubner, Phys. Rev. D **97**, 114025 (2018).
[11] G. Colangelo, M. Hoferichter, and P. Stoffer, JHEP **02** (2019), 006.
[12] M. Hoferichter, B.-L. Hoid, and B. Kubis, JHEP **08** (2019), 137.
[13] M. Davier, A. Hoecker, B. Malaescu, and Z. Zhang, Eur. Phys. J. C **80**, 241 (2020), [Erratum: Eur. Phys. J. C **80**, 410 (2020)].
[14] A. Keshavarzi, D. Nomura, and T. Teubner, Phys. Rev. D **101**, 014029 (2020).
[15] A. Kurz, T. Liu, P. Marquard, and M. Steinhauser, Phys. Lett. B **734**, 144 (2014).
[16] K. Melnikov and A. Vainshtein, Phys. Rev. **D70**, 113006 (2004).
[17] P. Masjuan and P. Sánchez-Puertas, Phys. Rev. **D95**, 054026 (2017).
[18] G. Colangelo, M. Hoferichter, M. Procura, and P. Stoffer, JHEP **04** (2017), 161.
[19] M. Hoferichter, B.-L. Hoid, B. Kubis, S. Leupold, and S. P. Schneider, JHEP **10** (2018), 141.
[20] A. Gérardin, H. B. Meyer, and A. Nyffeler, Phys. Rev. **D100**, 034520 (2019).
[21] J. Bijnens, N. Hermansson-Truedsson, and A. Rodríguez-Sánchez, Phys. Lett. **B798**, 134994 (2019).
[22] G. Colangelo, F. Hagelstein, M. Hoferichter, L. Laub, and P. Stoffer, JHEP **03** (2020), 101.
[23] T. Blum, N. Christ, M. Hayakawa, T. Izubuchi, L. Jin, C. Jung, and C. Lehner (RBC), Phys. Rev. Lett. **124**, 132002 (2020).
[24] G. Colangelo, M. Hoferichter, A. Nyffeler, M. Passera, and P. Stoffer, Phys. Lett. **B735**, 90 (2014).
[25] S. Borsanyi *et al.* (BMW), Nature **593**, 51 (2021).
[26] A. Boccaletti *et al.*, arXiv:2407.10913 [hep-lat] (2024).
[27] C. Davies *et al.* (Fermilab Lattice, HPQCD, MILC), Phys. Rev. D **101**, 034512 (2020).
[28] A. Bazavov *et al.* (Fermilab Lattice, HPQCD,, MILC), Phys. Rev. D **107**, 114514 (2023), arXiv:2301.08274 [hep-lat].
[29] T. Blum, Phys. Rev. Lett. **91**, 052001 (2003).
[30] D. Bernecker and H. B. Meyer, Eur. Phys. J. A **47**, 148 (2011).
[31] J. Gasser, A. Rusetsky, and I. Scimemi, Eur. Phys. J. C **32**, 97–114 (2003).
[32] G. S. Bali, S. Collins, and A. Schäfer, Comput. Phys. Commun. **181**, 1570–1583 (2010).
[33] L. Giusti, P. Hernandez, M. Laine, P. Weisz, and H. Wittig, JHEP **04** (2004), 013, arXiv:hep-lat/0402002.
[34] T. A. DeGrand and S. Schaefer, Nucl. Phys. B Proc. Suppl. **140**, 296 (2005), arXiv:hep-lat/0409056.
[35] E. Shintani, R. Arthur, T. Blum, T. Izubuchi, C. Jung, and C. Lehner, Phys. Rev. D **91**, 114511 (2015), arXiv:1402.0244 [hep-lat].
[36] T. Blum *et al.* (RBC, UKQCD), Phys. Rev. Lett. **121**, 022003 (2018).
[37] F. Erben, J. R. Green, D. Mohler, and H. Wittig, Phys. Rev. D **101**, 054504 (2020), arXiv:1910.01083 [hep-lat].
[38] M. Bruno, T. Izubuchi, C. Lehner, and A. S. Meyer, PoS **LATTICE2019**, 239 (2019), arXiv:1910.11745 [hep-lat].

[39] S. Lahert *et al.* (Fermilab Lattice, HPQCD, MILC), PoS **LATTICE2021**, 526 (2022).
[40] S. Lahert, *The light-quark connected contribution to the muon's anomalous magnetic moment*, Ph.D. thesis, Illinois U., Urbana (main) (2023).
[41] F. J. Frech, F. M. Stokes, K. K. Szabo, and B. C. Toth (Budapest-Marseille-Wuppertal), PoS **LATTICE2023**, 251 (2024), arXiv:2401.00514 [hep-lat].
[42] T. Banks, L. Susskind, and J. B. Kogut, Phys. Rev. D **13**, 1043 (1976).
[43] L. Susskind, Phys. Rev. D **16**, 3031 (1977).
[44] H. S. Sharatchandra, H. J. Thun, and P. Weisz, Nucl. Phys. B **192**, 205 (1981).
[45] N. Kawamoto and J. Smit, Nucl. Phys. B **192**, 100 (1981).
[46] A. Bazavov *et al.* (MILC), Phys. Rev. D **87**, 054505 (2013).
[47] G. W. Kilcup and S. R. Sharpe, Nucl. Phys. **B283**, 493 (1987).
[48] M. F. L. Golterman and J. Smit, Nucl. Phys. **B245**, 61 (1984).
[49] M. F. L. Golterman, Nucl. Phys. **B278**, 417 (1986).
[50] T. Blum, Phys. Rev. Lett. **91**, 052001 (2003), arXiv:hep-lat/0212018.
[51] G. P. Lepage, in *Theoretical Advanced Study Institute in Elementary Particle Physics* (1989).
[52] S. Borsanyi *et al.* (Budapest-Marseille-Wuppertal), Phys. Rev. Lett. **121**, 022002 (2018), arXiv:1711.04980 [hep-lat].
[53] B. Chakraborty, C. T. H. Davies, P. G. de Oliviera, J. Koponen, G. P. Lepage, and R. S. Van de Water (HPQCD), Phys. Rev. D **96**, 034516 (2017).
[54] Z. Fu and L. Wang, Phys. Rev. D **94**, 034505 (2016), arXiv:1608.07478 [hep-lat].
[55] J. F. Cornwell, *Group theory in physics: An introduction* (Academic, San Diego, 1997).
[56] I. Sakata, J. Math. Phys. **15**, 1702 (1974).
[57] M. Fukugita, Y. Kuramashi, M. Okawa, H. Mino, and A. Ukawa, Phys. Rev. D **52**, 3003 (1995), arXiv:hep-lat/9501024.
[58] R. L. Workman *et al.* (Particle Data Group), PTEP **2022**, 083C01 (2022).
[59] S. Navas *et al.* (Particle Data Group), Phys. Rev. D **110**, 030001 (2024).
[60] S. Borsanyi *et al.* (BMW), JHEP **09** (2012), 010.
[61] R. J. Dowdall, C. T. H. Davies, G. P. Lepage, and C. McNeile (HPQCD), Phys. Rev. D **88**, 074504 (2013).
[62] A. Bazavov *et al.* (Fermilab Lattice, MILC), Phys. Rev. D **93**, 113016 (2016).
[63] D. Hatton, C. T. H. Davies, G. P. Lepage, and A. T. Lytle (HPQCD), Phys. Rev. D **100**, 114513 (2019), arXiv:1909.00756 [hep-lat].
[64] G. Lepage, C. Gohlke, and D. Hackett, `gplepage/gvar v11.10` (2022).
[65] J. J. Dudek, R. G. Edwards, and C. E. Thomas, Phys. Rev. D **86**, 034031 (2012), arXiv:1203.6041 [hep-ph].
[66] B. Blossier *et al.*, JHEP **04** (2009), 094.
[67] M. Bruno, T. Izubuchi, C. Lehner, and A. S. Meyer, PoS **LATTICE2019**, 239 (2019).
[68] E. T. Neil and J. W. Sitison, Phys. Rev. E **108**, 045308 (2023), arXiv:2305.19417 [stat.ME].
[69] C. Lehner and A. S. Meyer, Phys. Rev. D **101**, 074515 (2020).
[70] C. Aubin, T. Blum, C. Tu, M. Golterman, C. Jung, and S. Peris, Phys. Rev. D **101**, 014503 (2020), arXiv:1905.09307 [hep-lat].
[71] C. Aubin, T. Blum, M. Golterman, and S. Peris, Phys. Rev. D **106**, 054503 (2022).
[72] G. Wang, T. Draper, K.-F. Liu, and Y.-B. Yang (χQCD), arXiv:2204.01280 [hep-lat] (2022).
[73] M. Cè *et al.*, Phys. Rev. D **106**, 114502 (2022).
[74] C. Alexandrou *et al.* (Extended Twisted Mass), Phys. Rev. D **107**, 074506 (2023), arXiv:2206.15084 [hep-lat].

[75] A. Bazavov *et al.* (Fermilab Lattice, HPQCD,, MILC), Phys. Rev. D **107**, 114514 (2023), arXiv:2301.08274 [hep-lat].
[76] T. Blum *et al.* (RBC, UKQCD), Phys. Rev. D **108**, 054507 (2023), arXiv:2301.08696 [hep-lat].
[77] S. Kuberski, M. Cè, G. von Hippel, H. B. Meyer, K. Ottnad, A. Risch, and H. Wittig, JHEP **03** (172), 172, arXiv:2401.11895 [hep-lat].
[78] M. Luscher, Commun. Math. Phys. **104**, 177 (1986).
[79] C. Bernard, M. Golterman, and Y. Shamir, Phys. Rev. D **77**, 074505 (2008), arXiv:0712.2560 [hep-lat].
[80] Z. T. Draper and S. R. Sharpe, Phys. Rev. D **105**, 034508 (2022), arXiv:2111.13975 [hep-lat].
[81] M. T. Hansen and T. Peterken, arXiv:2408.07062 [hep-lat] (2024).
[82] E. P. Wigner, Annals Math. **40**, 149 (1939), [Reprint: Nucl. Phys. Proc. Suppl. 6, 9(1989)].
[83] F. Gliozzi, Nucl. Phys. B **204**, 419 (1982).
[84] H. Kluberg-Stern, A. Morel, O. Napoly, and B. Petersson, Nucl. Phys. B **220**, 447 (1983).
[85] J. E. Mandula, G. Zweig, and J. Govaerts, Nucl. Phys. B **228**, 91 (1983).